Habilitation à diriger des recherches

Critical systems and quantum multifractality

Soutenue le 7 avril 2015

par

Olivier GIRAUD

Laboratoire de Physique Théorique et Modèles Statistiques, UMR 8626
Université Paris-Sud, Centre scientifique d'Orsay
15 rue Georges Clemenceau 91405 Orsay cedex

JURY

Dominique DELANDE	Université Pierre et Marie Curie	Président
Vladimir KRAVTSOV	ICTP Trieste	Rapporteur
Cécile MONTHUS	CEA Saclay	Rapportrice
Nicolas PAVLOFF	Université Paris Sud	
Peter SCHLAGHECK	Université de Liège	Rapporteur
Imre VARGA	Budapest University of Technology and Economics	

Contents

Foreword

A large part of the research I have been carrying out in the last decade can be related to a common thread[1]. Even though the connection is sometimes tenuous, various topics are related to localization, criticality and multifractality of quantum wavefunctions, in the framework of quantum chaos. This manuscript reviews my works on this subject, which includes the investigation of spectral statistics of intermediate systems (chapter 3), multifractal properties of random quantum maps (chapters 4 to 8), and connections between localization and entanglement in quantum information (chapter 9).

In order to keep the manuscript as coherent as possible, and avoid multiple introductions to different subjects, I will not present results that were obtained on various other topics I have been interested in. The main one is concerned with quantum information. In this field, I have been interested in quantum algorithms for the detection of delocalization in smallworld networks [OG009], for the computing of semiclassical formulas [OG016] and for efficient Monte-Carlo sampling [OG026]. I have also investigated various properties of quantum circuits, such as the optimal number of controlled-NOT gates required to generate a three-qubit state [OG015] or the construction of quantum circuits able to generate three-qubit random states [OG020]. A related topic was the investigation of the decompositions of quantum qubit channels into elementary channels [OG038]. I also did a series of works on geometrical questions in quantum information and more specifically the so-called classicality of quantum states, which is the investigation of the representation of spin density matrices as convex sums of projectors over spin coherent states. I have defined classical spin states in [OG017] as a generalization of classical states common in quantum optics. I then have considered the question of finding the most quantum states, which are the states farthest away from any classical spin state [OG024, OG025], and given a parametrization of spin-1 classical states [OG033].

Another significant part of my activity that I will overlook in the present manuscript deals with properties of complex networks, in particular spectral properties of their adjacency matrices and localization transitions in their eigenvectors. These investigations were carried on network models [OG021] and on real data from the World Wide Web and other directed networks [OG024]. In [OG031] and [OG041] networks describing local statistical features of the game of go were proposed and investigated.

[1] In the whole manuscript, numbers [xxx] refer to the bibliography at the end of the manuscript while [OGxxx] refer to my publications in chronological order, listed at Chapter 1.

Other research topics stemming from quantum chaos include a calculation of topology probabilities of closed Brownian paths on the twice punctured plane [OG005], and various mathematical properties of isospectral billiards: characterization of their diffractive orbits [OG004], and the connection between isospectral billiards and projective geometries in vector spaces over finite fields [OG008] – which has led to the RMP review paper [OG028].

I have intended this manuscript as a review of the various points about multifractality that I wanted to have fixed somewhere for future reference. This explains why some basic and well-known results are presented, as well as some details on calculations that had not been written elsewhere.

I am grateful to all the collaborators with whom I had the opportunity to work in the past years on all these subjects, especially in Toulouse and Orsay, but also in Bristol, Ljubljana, Ghent, Liège, Mar del Plata, Tübingen, London. I am also thankful to all those with which I had enlightening discussions over the years. I am also very grateful to the jury members for having taken the time to read the manuscript and to give valuable feedback.

Chapter 1

Publications

[OG001] E. Bogomolny, O. Giraud and C. Schmit, *Periodic Orbit Contribution to the 2-Point Correlation Form Factor for Pseudo-Integrable Billiards*, Commun. Math. Phys. **222**, 327-369 (2001).

[OG002] E. Bogomolny and O. Giraud, *Semiclassical Calculations of the Two-Point Correlation Form Factor for Diffractive Systems*, Nonlinearity **15** Vol. 4, 993 (2002).

[OG003] E. Bogomolny, O. Giraud and C. Schmit, *Nearest-Neighbor Distribution for Singular Billiards*, Phys. Rev. E **65**, 056214 (2002).

[OG004] O. Giraud, *Diffractive orbits in isospectral billiards*, J. Phys. A: Math. Gen. **37** No 7, 2751 (2004).

[OG005] O. Giraud, A. Thain and J. H. Hannay, *Shrunk loop theorem for the topology probabilities of closed Brownian (or Feynman) paths on the twice punctured plane*, J. Phys. A: Math. Gen. **37** No 8, 2913 (2004).

[OG006] O. Giraud, J. Marklof and S. O'Keefe, *Intermediate statistics in quantum maps*, J. Phys. A: Math. Gen. **37** No 28, L303 (2004).

[OG007] O. Giraud, *Periodic orbits and semiclassical form factor in barrier billiards*, Commun. Math. Phys. **260** No 1, 183 (2005).

[OG008] O. Giraud, *Finite geometries and diffractive orbits in isospectral billiards*, J. Phys. A: Math. Gen. **38** No 27, L477 (2005).

[OG009] O. Giraud, B. Georgeot and D. Shepelyansky, *Quantum computing of delocalization in small-world networks*, Phys. Rev. E **72**, 036203 (2005).

[OG010] O. Giraud and B. Georgeot, *Intermediate quantum maps for quantum computation*, Phys. Rev. A **72**, 042312 (2005).

[OG011] O. Giraud, *Distribution of bipartite entanglement for random pure states*, J. Phys. A: Math. Theor. **40**, 2793 (2007).

[OG012] O. Giraud, J. Martin and B. Georgeot, *Entanglement of localized states*, Phys. Rev. A **76**, 042333 (2007).

[OG013] O. Giraud, *Purity distribution for bipartite random pure states*, J. Phys. A: Math. Theor. **40**, F1053 (2007).

[OG014] J. Martin, O. Giraud and B. Georgeot, *Multifractality and intermediate statistics in quantum maps*, Phys. Rev. E **77**, 035201(R) (2008).

[OG015] M. Znidaric, O. Giraud and B. Georgeot, *Optimal number of controlled-NOT gates to generate a three-qubit state*, Phys. Rev. A **77**, 032320 (2008).

[OG016] B. Georgeot and O. Giraud, *Quantum computing of semiclassical formulas*, Phys. Rev. E **77**, 046218 (2008).

[OG017] O. Giraud, P. Braun and D. Braun, *Classicality of spin states*, Phys. Rev. A **78**, 042112 (2008).

[OG018] O. Giraud, J. Martin and B. Georgeot, *Entropy of entanglement and multifractal exponents for random states*, Phys. Rev. A **79**, 032308 (2009).

[OG019] I. Garcia-Mata, O. Giraud and B. Georgeot, *Quantum computation of multifractal exponents through the quantum wavelet transform*, Phys. Rev. A **79**, 052321 (2009).

[OG020] O. Giraud, M. Znidaric and B. Georgeot, *Quantum circuit for three-qubit random states*, Phys. Rev. A **80**, 042309 (2009).

[OG021] O. Giraud, B. Georgeot and D. Shepelyansky, *Delocalization transition for the Google matrix*, Phys. Rev. E **80**, 026107(2009).

[OG022] E. Bogomolny, O. Giraud and C. Schmit, *Random matrix ensembles associated with Lax matrices*, Phys. Rev. Lett. **103**, 054103 (2009).

[OG023] O. Giraud, P. Braun, and D. Braun, *Quantifying Quantumness and the Quest for Queens of Quantum*, New J. Phys. **12**, 063005 (2010).

[OG024] B. Georgeot, O. Giraud, and D. L. Shepelyansky, *Spectral properties of the Google matrix of the World Wide Web and other directed networks*, Phys. Rev. E **81**, 056109 (2010).

[OG025] J. Martin, O. Giraud, P. A. Braun, D. Braun, and T. Bastin, *Multiqubit symmetric states with high geometric entanglement*, Phys. Rev. A **81**, 062347 (2010).

[OG026] N. Destainville, B. Georgeot, and O. Giraud, *Quantum algorithm for exact Monte Carlo sampling*, Phys. Rev. Lett. **104**, 250502 (2010).

[OG027] J. Martin, I. Garcia-Mata, O. Giraud, and B. Georgeot, *Multifractal wave functions of simple quantum maps*, Phys. Rev. E **82**, 046206 (2010).

[OG028] O. Giraud and K. Thas, *Hearing shapes of drums - mathematical and physical aspects of isospectrality*, Rev. Mod. Phys. **82**, 2213 (2010).

[OG029] E. Bogomolny and O. Giraud, *Eigenfunction entropy and spectral compressibility for critical random matrix ensembles*, Phys. Rev. Lett. **106**, 044101 (2011).

[OG030] E. Bogomolny, O. Giraud, and C. Schmit, *Integrable random matrix ensembles*, Nonlinearity **24**, 3179 (2011).

[OG031] B. Georgeot and O. Giraud, *The game of go as a complex network*, Europhys. Lett. **97**, 68002 (2012).

[OG032] E. Bogomolny and O. Giraud, *Perturbation approach to multifractal dimensions for certain critical random matrix ensembles*, Phys. Rev. E **84**, 036212 (2011).

[OG033] O. Giraud, P. Braun, and D. Braun, *Parametrization of spin-1 classical states*, Phys. Rev. A **85**, 032101 (2012).

[OG034] E. Bogomolny and O. Giraud, *Multifractal dimensions for all moments for certain critical random-matrix ensembles in the strong multifractality regime*, Phys. Rev. E **85**, 046208 (2012).

[OG035] I. Garcia-Mata, J. Martin, O. Giraud, and B. Georgeot, *Multifractality of quantum wave packets*, Phys. Rev. E **86**, 056215 (2012).

[OG036] Y. Y. Atas, E. Bogomolny, O. Giraud, and G. Roux, *Distribution of the ratio of consecutive level spacings in random matrix ensembles*, Phys. Rev. Lett. **110**, 084101 (2013).

[OG037] Y. Y. Atas, E. Bogomolny, O. Giraud, P. Vivo, and E. Vivo, *Joint probability densities of level spacing ratios in random matrices*, J. Phys. A : Math. Theor. **46**, 355204 (2013).

[OG038] D. Braun, O. Giraud, I. Nechita, C. Pellegrini, and M. Znidaric, *A universal set of qubit quantum channels*, J. Phys. A : Math. Theor. **47**, 135302 (2014).

[OG039] E. Bogomolny and O. Giraud, *Calculation of mean spectral density for statistically uniform tree-like random models*, Phys. Rev. E **88**, 062811 (2013).

[OG040] R. Dubertrand, I. García-Mata, B. Georgeot, O. Giraud, G. Lemarié, and J. Martin, *Two scenarios for quantum multifractality breakdown*, Phys. Rev. Lett. **112**, 234101 (2014).

[OG041] V. Kandiah, B. Georgeot, and O. Giraud, *Move ordering and communities in complex networks describing the game of go*, Euro. Phys. J. B **87**, 246 (2014).

[OG042] Y. V. Fyodorov and O. Giraud, *High values of disorder-generated multifractals and logarithmically correlated processes*,
http://arxiv.org/abs/1407.4035

[OG-PROC001] O. Giraud, J. Martin and B. Georgeot, *Entanglement and localization of wavefunctions*, Proceedings of the NATO Advanced Research Workshop 'Recent Advances in Nonlinear Dynamics and Complex System Physics', Tashkent, Uzbekistan (2009).

Chapter 2

Introduction

The Nobel prize in Physics 1977 was awarded to Philip Warren Anderson, Sir Nevill Francis Mott and John Hasbrouck van Vleck "for their fundamental theoretical investigations of the electronic structure of magnetic and disordered systems" [1]. In a seminal paper [2], Anderson predicted that a quantum particle (e.g. an electron) in a disordered potential can be localized by quantum interferences even though the classical system is diffusive. The theory predicts that the wavefunctions are localized for any strength of disorder in dimension one, while in two dimensions the localization length can be exponentially large for weak disorder. In contrast, in dimension three a transition appears at a certain strength of disorder, separating a localized phase from a delocalized phase where the system is not an insulator any more [3]. At the transition point, it was argued that the wavefunctions are neither localized nor ergodic, but are characterized by amplitude distributions which are multifractal [4, 5, 6, 7, 8]. Similar effects have been observed in various different contexts: the quantum Hall effect [9, 10], pseudo-integrable billiards [11], random matrix models [12, 13, 14], quantized chaotic maps [15], tight-binding models of quasi-crystals [16] or disordered quantum smallworld networks [17], and others [18, 19]. Nontrivial multifractal properties play a crucial role in understanding e.g. the scaling of the activation temperature at superconductor-insulator transition [20] or peculiar conductance properties [21].

The study of wavefunction multifractality and of its observable experimental consequences is an active subject of research in the world both at the theoretical and experimental level. Initially developed as a set of theoretical concepts, it has now become an experimental reality. On the one hand, progress in computer technologies and in analytical methods enabled to get a clearer and clearer picture of these systems (see e.g. [22, 23, 24, 25, 26, 27, 28]). In parallel, theorists have discovered new instances where such phenomena take place, opening new possibilities for study and understanding (see e.g. [14, 29, 30]). More recently, various experimental studies have been dedicated to the Anderson transition, and enabled to probe the Anderson localization effect or the Anderson transition in Bose-Einstein condensates [31, 32, 33], cold atoms in optical lattices [34, 35, 36] or in disordered potentials created by speckle laser field [37, 38], acoustic waves in random media [39], or light [40].

The concept of fractal geometry was introduced by Mandelbrot in the seventies [41], to describe a range of phenomena characterized by the fact that a certain

quantity has a similar distribution at all scales. While many physical phenomena have been described in terms of fractals, the application of these ideas to quantum mechanics is much more recent. This notion has proven very useful in many areas of science, including fluid mechanics (turbulence), biology (DNA structure), economy (fluctuations of the stock market), geophysics, to name but a few examples (see references in [42]). Geometric fractals are characterized by their fractal dimension, which roughly describes how much space they occupy. Multifractals have an even richer structure, as they are characterized by the existence of a whole range of fractal dimensions. We refer to Chapter 5 for precise definitions.

Very recently, there has been a renewed interest in localization in many-body systems. In a one-dimensional disordered system, non-interacting particles are localized by the strength of the potential. It is nevertheless possible that the system undergoes a delocalization transition in the presence of short-range interactions [43, 44]. The vanishing of conductivity below some critical finite temperature was dubbed "many-body localization". The understanding of this localization transition and the properties of the critical phase is still largely a subject of discussion. Although we will not discuss many-body localization in this manuscript, our contribution to this question is a tool allowing to characterize spectral statistics for many-body problems by means of the statistics of nearest-neighbour ratios. This will be developed of Chapter 3.

In parallel, the field of quantum chaos has been developing in the past few decades. One of the goals of this domain is to study how a quantum system is affected by the dynamical properties of the underlying classical system, and to uncover universal properties, that is, generic features independent of microscopic properties of the systems described. One of the most important results concerns the statistical properties of quantum spectra. It has been conjectured by Bohigas, Giannoni and Schmit [45] that for systems which have a chaotic classical limit the quantum spectra should have statistical properties given by Random Matrix Theory (RMT), a theory introduced by Wigner [49] and later developed by Dyson [50] (see [51] for a review of founding papers) in order to describe statistical properties of the spectra of complex nuclei. This conjecture, although not proven, has been checked on numerous examples. On the other hand, for integrable systems Berry and Tabor [46] have proposed an argument according to which spectra in this case are characterized by Poissonian statistics, i.e. they are similar to sets of uncorrelated random numbers.

More recently, the existence of a third universality class of spectral statistics was suggested in [47] for systems at the metal-insulator transition. It is characterized by level repulsion and linear number variance. These spectral statistics are intermediate between the chaotic and integrable cases [48]. Numerical studies have shown that wavefunctions corresponding to this situation in general display multifractal distributions. The main question is to identify the quantities which are universal in this intermediate critical case.

In order to find a simple description for this third universality class, in the spirit of RMT, which has allowed great success in the understanding of properties of quantum chaotic systems, various random matrix ensembles have been introduced. Some of them realize a crossover between RMT and Poisson statistics and display

intermediate statistics [52]. Other ensembles are defined by random banded matrices (see section 4.2.2). In 2004 we introduced a family of quantum maps with critical properties [OG006].

Quantum maps are defined as quantizations of classical maps represent quantum evolution with discrete time steps [53]. They are particularly convenient tools to investigate chaotic behaviour, as they have the advantage of displaying a great variety of classical and quantum behaviours, and yet are simpler to investigate than systems such as quantum billiards. Indeed, billiards were extensively studied in the past decades, in particular using trace formulas; however, in most cases it is difficult to describe the classical periodic orbits analytically, and quantum wavefunctions are difficult to compute numerically. On the other hand, analytical investigations for quantum maps turn out to be considerably easier than the geometric approach required for billiards, while numerical investigations only require diagonalization of matrices, rather than the implementation of finite-element methods to find eigenmodes of 2d surfaces.

After having shown the existence of quantum maps with critical properties in [OG006], we were led to introduce new ensembles of critical random matrices, based on Lax matrices of integrable models of interacting particles on a line. These definitions were based on a formal analogy between the quantum maps defined in [OG006] and certain Lax matrices describing interacting relativistic particles. The investigation of such maps and random matrix ensembles, and more specifically their spectral properties and multifractality of their eigenvectors, constitutes the central part of the present manuscript, and will be developed in chapters 4 to 8.

More recently, the fields of quantum information and computation have developed in the last years as a new means of treating information. One of its goal is to investigate how quantum states can be entangled, manipulated and measured in an optimal way in order to process information efficiently. The most common basic building block of quantum information processors is the qubit, which is any two-level quantum system satisfying a certain number of properties [54]. Ensembles of interacting qubits are manipulated by applying one-qubit or two-qubit operations. The sequence of operations applied, together with a final measurement scheme, is a quantum algorithm. The domain has been boosted by the discovery of quantum algorithms which could solve problems more efficiently than their classical counterpart, one of the most famous being Shor's prime number decomposition algorithm [55]. However, since then, surprisingly few efficient algorithms (that is, exponentially, or at least polynomially faster than classical algorithms) have been exhibited. Moreover the efficiency of quantum algorithms is conditioned to the ability to extract useful information from the computation.

Quantum chaos gives a framework in which it is interesting to study the possibilities of quantum computation. The interplay between quantum information and quantum chaos has various aspects. Early works have discussed the ways in which chaos might affect the efficiency of a quantum computer [56]. In parallel, changes in entanglement are indicators of a quantum phase transition. There is increasing evidence that phase transitions obtained in the framework of random matrix theory are mirrored by transitions in the entanglement properties of random states (see

e.g. [57, 58, 59, 60]). Evolution of entanglement across a metal-insulator transition was considered in integrable or chaotic one-dimensional tight-binding models [61] or in various models of one or two-dimensional spin chains [62, 63, 64]. In Chapter 9 I will discuss various aspects of quantum information in connection with localization problems.

Chapter 3

Quantum chaos – Level and eigenfunction statistics

One of the goals of quantum chaos is to classify quantum systems according to universal statistical properties. The investigation of properties of quantum spectra is based on various analytical tools. In the first section we briefly introduce the statistical functions that will be used in the presentation of our result, which will be the object of the subsequent sections.

Various conjectures describing statistical properties of energy levels of quantum systems have been proposed, depending on the nature of the dynamics of the underlying classical system. These conjectures are based on some analytical arguments and many numerical simulations pointing in the same direction. We will review these conjectures, as well as our contributions, in sections 3.2–3.4.

3.1 Statistical functions

In most of what will be considered here, the spectrum is a set of eigenvalues of some Hamiltonian, labeled $\{E_1, E_2, ..., E_N, ...\}$, and all statistical quantities are an average over disorder realizations of the system. One can also average in an energy window around some fixed energy E. For some quantities one can further average over all possible positions of the energy window. The density of eigenvalues is defined as

$$\rho(E) = \langle \sum_n \delta(E - E_n) \rangle, \tag{3.1}$$

where the sum runs over all eigenvalues. The level counting function is the integrated version of the density (3.1), namely

$$N(E) = \langle \sum_{n=1}^{\infty} \Theta(E - E_n) \rangle = \langle \sum_{E_i < E} 1 \rangle. \tag{3.2}$$

The n-point correlation functions are defined as

$$R_n(\epsilon_1, \epsilon_2, ..., \epsilon_n) = \langle \rho(E + \epsilon_1)\rho(E + \epsilon_2)...\rho(E + \epsilon_n) \rangle, \tag{3.3}$$

which represents the probability to have n energy levels at specified positions. If we define the connected two-point correlation function as

$$R_2^c(\epsilon) = \langle \rho(E - \epsilon/2)\rho(E + \epsilon/2)\rangle - \langle \rho(E)\rangle^2, \tag{3.4}$$

the form factor is then its Fourier transform

$$K(\tau) = \frac{1}{\langle \rho(E)\rangle} \int_{-\infty}^{\infty} d\epsilon R_2^c(\epsilon) e^{i\epsilon\tau t_H/\hbar}, \tag{3.5}$$

where the Heisenberg time is defined as

$$t_H = 2\pi\hbar\langle \rho(E)\rangle = \frac{2\pi\hbar}{\Delta} \tag{3.6}$$

and corresponds to the shortest energy scale, given by the mean level spacing $\Delta = 1/\langle \rho(E)\rangle$.

In order to characterize the statistics of energy levels, the most studied quantity is the distribution of nearest-neighbour spacings $E_{i+1} - E_i$. At places of the spectrum where the density of states is low, the mean local nearest-neighbour spacing will be smaller than at places where the density is high. In order to be able to compare different spectra, or different regions of a spectrum, and retain only the statistics of fluctuations around the mean position of eigenvalues, a common procedure is to "unfold" the spectrum in order to get a mean level spacing equal to 1 all over the spectrum. More specifically, one defines new eigenvalues as $e_n = N(E_n)$, where $N(E)$ is the counting function (3.2), i.e. the mean number of levels less than E [65]. The mean level spacing of these new eigenvalues is then 1. The distribution $P(s)$ of nearest-neighbour spacings $s_i = e_{i+1} - e_i$ then verifies the two normalization conditions

$$\int_0^{\infty} P(s)ds = 1 \quad \text{et} \quad \int_0^{\infty} sP(s)ds = 1. \tag{3.7}$$

Similarly one can define the probability $P(n, s)$ to find in the spectrum two eigenvalues separated by a distance s with $n-1$ other eigenvalues in-between. In particular $P(s) = P(1, s)$. The two-point correlation function can then be expressed as

$$R_2(s) = \sum_{n=1}^{\infty} P(n, s). \tag{3.8}$$

The quantity $P(0)$ is the probability that two eigenvalues be infinitely close to each other. If $P(0) = 0$ then nearest neighbours tend to never touch each other, a phenomenon which is called 'level repulsion'. The value of $P(s)$ at small arguments is governed by energy correlations at a scale of the order of the mean level spacing, that is, time scales of the order of the Heisenberg time (3.6).

The unfolding of the spectrum makes easier a comparison between different models, provided the counting function $N(E)$ is known analytically or easily estimated numerically. This is the case for instance for the usual Dyson random matrix ensembles, where the mean density of states can be shown to be given by a semi-circle (see Eq. (3.38) below). Another example is that of statistically uniform tree-like

random models, for which we derived in [OG039] several accurate approximations for the mean spectral density.

However, when $N(E)$ is not accessible analytically and is difficult to compute reliably numerically, as for instance in many-body problems, it may be useful to avoid the unfolding procedure. A new spectral measure was proposed in [66], as the statistics of the ratio between consecutive nearest-neighbour spacings

$$\tilde{r}_n = \min\left(r_n, \frac{1}{r_n}\right), \qquad r_n = \frac{E_{n+1} - E_n}{E_n - E_{n-1}}. \tag{3.9}$$

Since the ratio is expected to be independent of the local density of states, the unfolding procedure becomes unnecessary. Such a quantity has been investigated e.g. in finite size lattices [67, 68, 69] and in many-body localization problems [66, 67, 68, 69, 70, 71]. If there is a statistical symmetry between left and right intervals at a given energy, the distribution of r_n and that of $1/r_n$ are the same, which implies the following functional equation

$$P(r) = \frac{1}{r^2} P\left(\frac{1}{r}\right) . \tag{3.10}$$

Whenever (3.10) holds, it is equivalent to consider the whole distribution $P(r)$ or to restrict the study to the support $[0, 1]$ by considering the variable $\tilde{r}$ defined in (3.9), as was done in [66]. Other types of ratios can be studied; the simplest is the kth overlapping ratio $(E_{n+k+1} - E_n)/(E_{n+k} - E_{n-1})$, for which analytic expressions can be found in some simple cases (see [OG037] and next section).

The number variance $\Sigma^2(L)$ is defined as the variance of the number of eigenvalues lying in an interval of length L. It is given by

$$\Sigma^2(L) = \langle (n(L) - \langle n(L) \rangle)^2 \rangle, \tag{3.11}$$

where $n(L)$ is the number of eigenvalues in a given interval of length L. The average in (3.11) is then taken over all positions of that interval. The number variance can be expressed as a function of the two-point correlation function $R_2(s)$ given by (3.8) [72]. If the mean level spacing is supposed to be equal to 1, then $\langle n(L) \rangle = L$ and

$$\Sigma^2(L) = L - 2\int_0^L (L - u)(1 - R_2(u))du. \tag{3.12}$$

The "level compressibility" is defined as the quantity χ such that

$$\Sigma^2(L) \sim_{L\to\infty} \chi L. \tag{3.13}$$

In particular for $K(0) \neq 0$ Eq. (3.12) implies that $\Sigma^2(L) \sim_\infty K(0)L$: the limit of the form factor at small argument characterizes the asymptotic behaviour of the number variance. The Laplace transform of the two-point correlation function has a series expansion of the form

$$g_2(t) = \int_0^\infty ds\, R_2(s) \mathrm{e}^{-ts} = \frac{1}{t} + \frac{\chi - 1}{2} + O(t), \tag{3.14}$$

from which one can obtain χ [73]. While $P(s)$ at small s probes time scales of the order of the Heisenberg time (energy scales of the order of the mean level spacing), the level compressibility characterizes long-range correlations of energy, that is, very short time scales.

Alternatively, one may consider, rather than the Hamiltonian, the evolution operator $U = \exp(-iHt/\hbar)$, which is unitary. Let its eigenvalues be $E_n = e^{i\theta_n}, 1 \leq n \leq N$. Then the density of (pseudo-)eigenvalues is defined as

$$\rho(\theta) = \sum_{n=1}^{N} \sum_{k=-\infty}^{\infty} \delta\left(\theta - \theta_n + 2k\pi\right). \tag{3.15}$$

The nearest-neighbour spacing distribution is given by

$$P(s) = \frac{1}{N} \sum_{j=1}^{N} \delta\left(s - \frac{N}{2\pi}(\theta_j - \theta_{j-1})\right), \tag{3.16}$$

where the factor of $N/2\pi$ ensures that s measures spacings on the scale of the mean level spacing $2\pi/N$. The two-point correlation density in this case reads

$$R_2(s) = \frac{1}{N} \sum_{j,k=1}^{N} \sum_{m\in\mathbb{Z}} \delta\left(s - \frac{N}{2\pi}(\theta_j - \theta_k + 2\pi m)\right). \tag{3.17}$$

Using the Poisson summation formula, one can rewrite (3.17) as

$$R_2(s) = \frac{1}{N^2} \sum_{n\in\mathbb{Z}} \left|\mathrm{tr}U^n\right|^2 e^{2i\pi ns/N}. \tag{3.18}$$

The spectral form factor is defined as the Fourier transform of $R_2(s)$,

$$K(\tau) = \frac{1}{N}\left|\mathrm{tr}U^n\right|^2, \quad \tau = n/N. \tag{3.19}$$

One can show [74], [OG006], that the level compressibility, defined by

$$\chi = \lim_{\ell\to 0} \lim_{\substack{N_\nu\to\infty \\ L=\ell N_\nu}} \frac{\Sigma^2(L)}{L} \tag{3.20}$$

with $\Sigma^2(L)$ the number variance (3.11) calculated over macroscopic intervals of size $L = \ell N_\nu$ (with $\ell > 0$ fixed and the limit is taken along suitable subsequences $N_1, N_2, \ldots \to \infty$ of integers), is given by

$$\chi = \lim_{n\to\infty} \lim_{N_\nu\to\infty} \frac{1}{n} \sum_{n'=1}^{n} K(n'/N_\nu). \tag{3.21}$$

Numerically, the level compressibility is quite difficult to compute reliably. First one has to calculate the number variance on the unfolded spectrum (with mean level spacing $\Delta = 1$) by taking the average of $n(L)$ over windows of length $L = 2k\Delta$. One

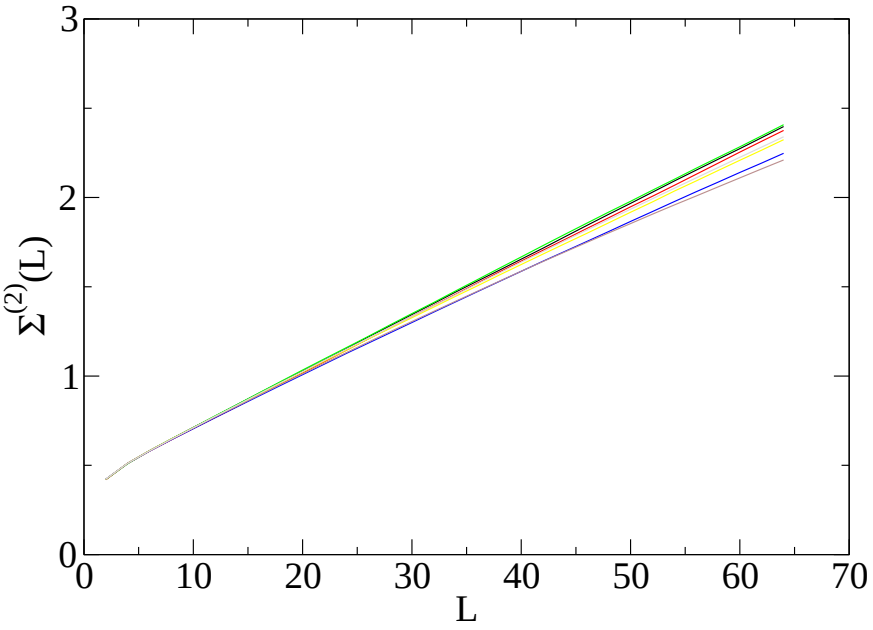

Figure 3.1: Number variance $\Sigma^2(L)$ for the PRBM model (4.11) with $1/b = 0.4$ for matrices of size $N = 256, 362, 512, 724, 1024, 1448, 2048$. Average is taken over windows of length $L = 2k\Delta$ with $1 \leq k \leq 32$, centered at integer positions of the energy around $E = 0$, namely (in units of Δ) $E = -32$ to $E = 32$, and over random realizations of the matrices (from $r = 32000$ for $N = 256$ to $r = 500$ for $n = 2048$).

should in principle take the thermodynamic limit $N \to \infty$ before taking the limit of large window size $L \to \infty$. Numerically, the linear behaviour (3.13) holds only at large L, but due to finite-size effects the value of L is restricted. Thus the level compressibility $\chi(N)$ is extracted from a quadratic fit $\Sigma^{(2)}(L) = a + \chi(N)L + cL^2$ performed in an intermediate range of values of L. The large–N asymptotics for χ is finally obtained by a linear fit of $\chi(N)$ as a function of $1/N$. We give an illustration of this procedure in Figs. 3.1–3.2 for a random matrix ensemble defined in Section 4.2.2. Figure 3.1 shows the number variance (3.12) as a function of L, and Fig. 3.2 the extrapolation to large N. Results of this numerical investigation were published in [OG029].

3.2 Integrable systems and Poisson statistics

The Berry-Tabor conjecture [46] states that for classically chaotic systems the distribution of energy levels follows the Poisson distribution of independent random variables. A review of analytical elements supporting this conjecture is found at [75]. According to this conjecture, only "generic" classically integrable systems have a Poissonian statistics: many examples of integrable systems whose quantum counterpart does not verify Berry-Tabor conjecture are known, for instance, harmonic oscillators (Berry-Tabor [46], Pandey *et al* [76], Bleher [77, 78], Greenman [79]), Zoll

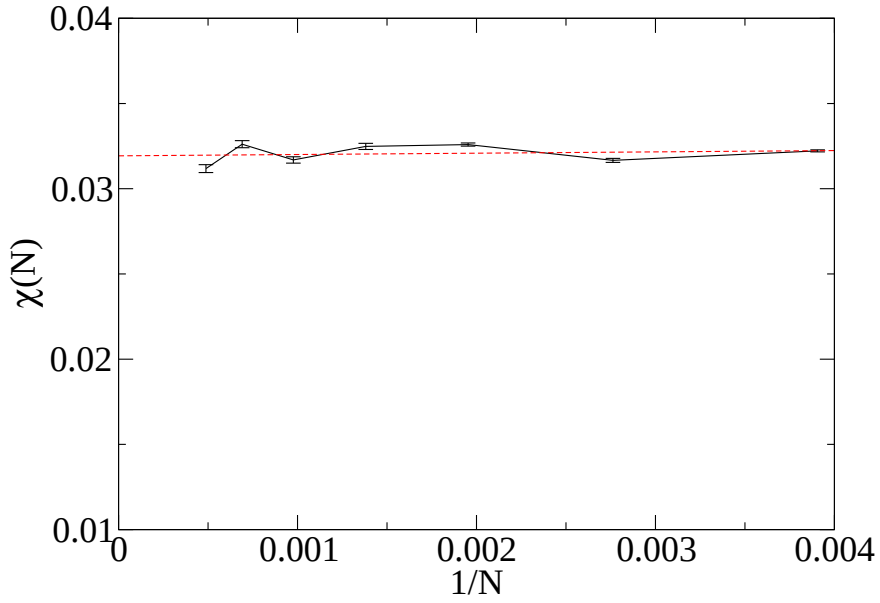

Figure 3.2: Level compressibility $\chi(N)$ as a function of $1/N$. Here $\chi(N)$ is extracted from a quadratic fit $\Sigma^{(2)}(L) = a + \chi(N)L + cL^2$ of the data of Fig. 3.1, performed in the range $L \in [10, 32]$. Dashed line is a linear fit; the extrapolated value of χ is $\chi = 0.032$ (see [OG029]).

surfaces (surfaces whose geodesics are closed and of the same length, like the sphere (see Duistermaat and Guillemin [80], Weinstein [81] or Colin de Verdière [82]). It is also possible to construct artificially one-dimensional integrable systems whose statistics is of random matrix type by constructing an ad-hoc potential [83].

Spectral correlation functions for Poisson variables can be easily derived. In particular the nearest-neighbour spacing distribution is given by

$$P(s) = e^{-s}, \tag{3.22}$$

the form factor is $K(\tau) = 1$ and the number variance $\Sigma^2(L) = L$.

In [OG036] we showed that the ratio of adjacent spacings of Poisson variables is distributed according to

$$P(r) = 1/(1+r)^2. \tag{3.23}$$

We derived in [OG037] the distribution $P_k(r)$ of the kth overlapping ratio, defined as $(E_{n+k+1} - E_n)/(E_{n+k} - E_{n-1})$. It reads

$$P_k(r) = \begin{cases} \dfrac{r^k(k+1+kr)}{(1+r)^2} & \text{if } r < 1, \\ \dfrac{k+r(k+1)}{r^{k+1}(1+r)^2} & \text{if } r > 1. \end{cases} \tag{3.24}$$

3.3 Chaotic systems and random matrix theory

3.3.1 Random matrix theory

Random matrices are matrices with random entries, whose probability distribution satisfies some symmetry rules. The basic idea behind their introduction in Physics is that Hamiltonians of quantum system are large Hermitian matrices whose entries may be too complicated to work out analytically. One then makes the guess that statistical properties of the real Hamiltonian may be similar to those of a matrix with entries given by random numbers. The probability distribution chosen for the matrix coefficients depends on the underlying structure, that is, on the symmetries of the system. A symmetry can be represented by an operator T such that for any pair of states $|\Psi\rangle$ and $|\Psi'\rangle$ one has $|\langle T\Psi|T\Psi'\rangle| = |\langle\Psi|\Psi'\rangle|$. According to Wigner's theorem, this implies that T is either a unitary operator U or an anti-unitary operator of the form UK, with K the (anti-unitary) complex conjugation operator (the fact that only these two possibilities exist can be traced back to the fact that there are only two field automorphisms on $\mathbb{C}$, namely the identity and the complex conjugation). One can show that for systems with integer spin, time-reversal can be represented by the anti-unitary operator K, while for systems with half-integer spins it can be taken as $K(-i\sigma_y)$ for each spin–1/2.

How can one model the Hamiltonian by a random Hermitian matrix distributed according to some measure $P(H)dH$? If one wants to keep only generic properties (for instance if nothing is known about the microscopic features of the system), one should require that the probability of a matrix H be the same as the probability of its transform under any arbitrary symmetry T. If the system has no time-reversal symmetry, then from the discussion above $P(H)$ should be invariant under all unitary transformations. For a system with integer spin and time-reversal invariance, one can show that there exists a basis in which the Hamiltonian can be expressed as a real symmetric matrix. In this case, the system should be better described by restricting the previous set to symmetric random matrices with a probability distribution invariant under orthogonal transformations. For a system with half-integer spin and time-reversal invariance, one can represent H by a symplectic matrix, and one can restrict the set to quaternionic random matrices (see the more precise definition below) [72]. These symmetry considerations lead to three invariant ensembles of random matrices, depending on the symmetries of the underlying system; these are the three "historical" Wigner-Dyson random matrix ensembles. Other ensembles involving discrete symmetries can be constructed, namely three chiral ensembles in the context of condensed matter physics, and four Bogoliubov-De Gennes ensembles describing superconducting systems [84]. This classification is complete, in the sense that it can be put in relation with the Cartan classification of compact symmetric Riemannian manifolds. Here we concentrate on the three Wigner-Dyson ensembles.

These three ensembles are defined as ensembles of matrices with Gaussian-distributed random entries which are respectively real, complex or quaternionic. The Gaussian Orthogonal Ensemble (GOE) is the ensemble of real symmetric matrices with a probability law $P(H)$ invariant under orthogonal conjugation $H' = O^t HO$

and such that matrix elements $H_{ij}, i \leq j$ are independent random variables. The Gaussian Unitary ensemble GUE is the set of complex Hermitian matrices with a probability law $P(H)$ invariant under unitary conjugation $H' = U^\dagger HU$, and such that the real and imaginary part of matrix elements are independent random variables. The Gaussian symplectic ensemble GSE is the set of $2N \times 2N$ real quaternionic matrices ($H = H^\mu \sigma_\mu$, where σ_μ are Pauli matrices, H^0 an $N \times N$ real symmetric matrix and $H^i, 1 \leq i \leq 3$ real antisymmetric matrices), with a probability law $P(H)$ invariant under symplectic transformation (i.e. under conjugation with a $2N \times 2N$ unitary matrix such that $Z = BZ^tB$ with $Z = H^2\sigma_2, H^2 = I_N$). Invariance under conjugation and independence of matrix coefficients imply that $P(H)$ takes the form

$$P(H) = \exp\left(-a \,\mathrm{tr} H^2\right), \tag{3.25}$$

with a a positive real number [72].

3.3.2 Conjecture for chaotic systems

The conjecture of Bohigas-Giannoni-Schmit [45] states that the statistics of a system whose classical counterpart is chaotic follows that of one of these three Gaussian ensembles, depending on the symmetries of the system. Systems invariant under time-reversal have a GOE statistics for integer spin, GSE for half-integer spin. Generic systems have a GUE statistics [45, 85]. In the same spirit, one defines the Dyson circular ensembles of random unitary matrices COE, CUE and CSE, which describe quantum evolution operators (for instance for a system whose dynamics can be described by a periodic Hamiltonian, $U = e^{-\frac{i}{\hbar}\int_0^T H(t)dt}$).

Many numerical simulations support this conjecture. There are many instances of quantum systems where random matrix level statistics have been observed. This was famously analyzed for a "nuclear data ensemble" made of 1407 nuclear resonance energies aggregated from 30 sequences from 27 various nuclei [86]. Other instances include energy levels of chaotic billiards [45], the rovibrational spectrum of the H_3^+ molecule close to the $H^+ + H_2$ dissociation [87], or zeros of the Riemann zeta function [65].

Note that it has been shown however that certain systems without time-reversal or spatial symmetry follow GOE statistics [88]. This is for instance the case for systems such as a billiard with Aharonov-Bohm flux line situated on a symmetry axis, for which a combination (time-reversal and spatial symmetry) gives rise to a real symmetric Hamiltonian and is responsible for a GOE behaviour. For some systems, such as for arithmetical chaos [89], spectral statistics is Poissonian although classical mechanics is entirely chaotic.

3.3.3 Random matrix theory: spectral correlation functions

Analytical predictions on the statistical functions describing energy levels of chaotic systems can then be made from calculations on the Gaussian ensembles defined by (3.25). The joint distribution of eigenvalues $\lambda_1, \ldots, \lambda_N$ is easily obtained from a change of variables (from matrix components to eigenvalue-eigenvector components)

as

$$P(\lambda_1, \lambda_2, ..., \lambda_N) = C \prod_{i<j} |\lambda_i - \lambda_j|^\beta \exp\left(-\frac{1}{4\sigma^2} \sum_i \lambda_i^2\right) \tag{3.26}$$

where $\beta = 1, 2, 4$ for (respectively) GOE, GUE and GSE, is the Dyson index, and σ^2 the variance of the Gaussian distribution of the matrix coefficients [72]. The constant C is imposed by normalisation.

A useful way of considering (3.26) is to rewrite it as

$$P(\lambda_1, \lambda_2, ..., \lambda_N) = \frac{1}{Z} e^{-\beta W(\lambda_1, \lambda_2, ..., \lambda_N)} \tag{3.27}$$

with

$$W(\lambda_1, \lambda_2, ..., \lambda_N) = -\frac{1}{4\sigma^2 \beta} \sum_i \lambda_i^2 + \beta \sum_{j<k} \ln |\lambda_j - \lambda_k|. \tag{3.28}$$

It is convenient to rescale the variables by setting $x_i = \lambda_i/(\sigma\sqrt{2})$, so that $P(x_1, x_2, ..., x_N) \sim \exp[-\beta W(x_1, \ldots, x_N)]$ with

$$W(x_1, x_2, ..., x_N) = -\frac{1}{2} \sum_i x_i^2 + \sum_{j<k} \ln |x_j - x_k|. \tag{3.29}$$

Variables $x_1, \ldots, x_N$ can then be seen as the position of N particles on a line with quadratic confining potential and logarithmic repulsion between pairs of particles, and β is interpreted as an inverse temperature.

An interesting consequence of (3.27)–(3.29) is that the most probable distribution of the x_i corresponds to the equilibrium configuration where all $\partial W/\partial x_i$ vanish, a condition equivalent to

$$x_k = \sum_{j \neq k} \frac{1}{x_k - x_j} \ , 1 \leq k \leq N. \tag{3.30}$$

These are the Stieltjes relations. They characterize the zeros of Hermite polynomials, which are a family of orthogonal polynomials defined by

$$H_n(x) = (-1)^n e^{x^2} \frac{d^n}{dx^n} e^{-x^2} = n! \sum_{k=0}^{\lfloor n/2 \rfloor} \frac{(-1)^k}{k!(n-2k)!} (2x)^{n-2k}. \tag{3.31}$$

Exact calculations of spectral quantities are conveniently performed by means of such orthogonal polynomials. For instance, the Vandermonde determinant appearing in (3.26) can be rewritten

$$\prod_{j<k} |x_j - x_k| = \begin{vmatrix} 1 & x_1 & \ldots & x_1^{N-1} \\ 1 & x_2 & \ldots & x_2^{N-1} \\ \vdots & \vdots & & \vdots \\ 1 & \vdots & & x_N^{N-1} \end{vmatrix} \propto \begin{vmatrix} H_0(1) & H_1(x_1) & \ldots & H_{N-1}(x_1) \\ H_0(x_2) & H_1(x_2) & \ldots & H_{N-1}(x_2) \\ \vdots & \vdots & & \vdots \\ H_0(x_N) & \vdots & & H_{N-1}(x_N) \end{vmatrix} \tag{3.32}$$

where $H_n(x)$ are the Hermite polynomials (3.31). Setting

$$\varphi_n(x) = \frac{e^{-x^2/2}}{\sqrt{2^n n! \sqrt{\pi}}} H_n(x), \tag{3.33}$$

the joint distribution of eigenvalues for the GUE ensemble can then be rewritten under the simple form

$$\prod_{1\le j<k\le N} |x_j - x_k|^2 \prod_{j=1}^{N} e^{-x_j^2} = \begin{vmatrix} \varphi_0(1) & \dots & \varphi_{N-1}(x_1) \\ \varphi_0(x_2) & \dots & \varphi_{N-1}(x_2) \\ \vdots & & \vdots \\ \varphi_0(x_N) & & \varphi_{N-1}(x_N) \end{vmatrix}^2 = \det[K(x_i, x_j)] \tag{3.34}$$

with

$$K(x,y) = \sum_k \varphi_k(x)\varphi_k(y). \tag{3.35}$$

Orthogonality of φ_n (the fact that $\int_{-\infty}^{\infty} dx \varphi_m(x)\varphi_n(x) = \delta_{mn}$) implies

$$\int_{-\infty}^{\infty} K(x,y)K(y,z)dy = K(x,z). \tag{3.36}$$

One can then obtain exact expressions for the correlation functions. For instance, the mean level density

$$\rho(x) \propto \int_{-\infty}^{\infty} dx_2 \dots dx_N \det[K(x_i, x_j)] = K(x,x) \tag{3.37}$$

can be shown, using Christoffel-Darboux formula for Hermite polynomials, to be asymptotically given by the semi-circle law [72]

$$\rho(x) = \begin{cases} \frac{1}{\pi}\sqrt{4N^2 - x^2} & |x| \le 2N \\ 0 & \text{otherwise.} \end{cases} \tag{3.38}$$

The connected two-point correlation functions can be derived similarly, and read

$$\begin{aligned} \text{GOE:} \quad R_2^c(x) &= \delta(x) - \left(\frac{\sin \pi x}{\pi x}\right)^2 \\ &+ \left(\int_0^{\pi x} \frac{\sin y}{y} dy - \frac{\pi}{2}\text{sgn}(x)\right)\left(\frac{\cos \pi x}{\pi x} - \frac{\sin \pi x}{(\pi x)^2}\right) \\ \text{GUE:} \quad R_2^c(x) &= \delta(x) - \left(\frac{\sin \pi x}{\pi x}\right)^2 \\ \text{GSE:} \quad R_2^c(x) &= \delta(x) - \left(\frac{\sin 2\pi x}{2\pi x}\right)^2 + \int_0^{2\pi x} \frac{\sin y}{y} dy \left(\frac{\cos 2\pi x}{2\pi x} - \frac{\sin 2\pi x}{(2\pi x)^2}\right). \end{aligned} \tag{3.39}$$

The form factor is then easily obtained from (3.5), yielding

$$\begin{aligned}
\text{GOE:}\quad K(\tau) &= \begin{cases} 2\tau - \tau\ln(1+2\tau) & 0<\tau<1 \\ 2-\tau\ln\left(\frac{2\tau+1}{2\tau-1}\right) & \tau>1 \end{cases} \\
\text{GUE:}\quad K(\tau) &= \begin{cases} \tau & 0<\tau<1 \\ 1 & \tau>1 \end{cases} \\
\text{GSE:}\quad K(\tau) &= \begin{cases} \frac{1}{2}\tau - \frac{1}{4}\tau\ln|1-\tau| & 0<\tau<2 \\ 1 & \tau>2. \end{cases}
\end{aligned} \tag{3.40}$$

The number variance for the Gaussian ensembles has the asymptotic behaviour [90]

$$\Sigma^2(L) \simeq \frac{2}{\beta\pi^2}\ln(L), \quad L \gg 1. \tag{3.41}$$

3.3.4 Eigenvector distribution functions

In a similar way, analytical expressions can be obtained for the distribution of eigenvector components. A consequence of the change of variables leading to (3.26) is that eigenvectors have a uniform distribution on the unit sphere. Setting $x_i = N|\psi_i|^2$, the distribution of a component is thus readily obtained (for instance for GOE) as

$$P(x) \propto \int \prod_i dx_i \delta(x - Nx_1^2)\delta\left(\sum_i x_i^2 - 1\right), \tag{3.42}$$

which can be easily integrated. After normalization this gives

$$P(x) = \frac{\Gamma\left(\frac{N}{2}\right)}{\sqrt{\pi N}\,\Gamma\left(\frac{N-1}{2}\right)} \frac{\left(1-\frac{x}{N}\right)^{\frac{N-3}{2}}}{\sqrt{x}}. \tag{3.43}$$

At the large–N limit this yields the Porter-Thomas distribution for GOE,

$$P(x) = \frac{e^{-x/2}}{\sqrt{2\pi x}}. \tag{3.44}$$

For the other Wigner-Dyson ensembles with index β, similar calculations yield [72]

$$P(x) = \frac{e^{-\beta x/2}}{x\Gamma(\beta/2)}\left(\frac{\beta x}{2}\right)^{\beta/2}. \tag{3.45}$$

3.3.5 Spacing distribution: the Wigner surmise

Expressions for the nearest-neighbour spacing distribution can be obtained in the large–N limit, but the formulas are quite heavy. Rather than cumbersome exact expressions, Wigner [91] proposed a simple approximate expression for $P(s)$, namely

$$P(s) = a_\beta s^\beta e^{-b_\beta s^2}\,, \tag{3.46}$$

with constants a_β et b_β obtained from normalisation conditions (3.7) [72] as

$$a_\beta = 2\frac{\Gamma^{\beta+1}\left((\beta+2)/2\right)}{\Gamma^{\beta+2}\left((\beta+1)/2\right)}, \qquad b_\beta = \frac{\Gamma^2\left((\beta+2)/2\right)}{\Gamma^2\left((\beta+1)/2\right)}. \tag{3.47}$$

This formula, called the Wigner surmise, corresponds to the exact result for 2×2 matrices, and is numerically in very good agreement with the exact large–N expressions [92] (see also the discussion in [OG037]). Explicitly, for $\beta = 1, 2, 4$, one gets the Wigner-Dyson distributions

$$\begin{aligned} &\text{GOE:} \quad P(s) = \frac{\pi}{2} s \exp\left(-\frac{\pi}{4}s^2\right) \\ &\text{GUE:} \quad P(s) = \frac{32}{\pi^2} s^2 \exp\left(-\frac{4}{\pi}s^2\right) \\ &\text{GSE:} \quad P(s) = \frac{2^{18}}{3^6\pi^3} s^4 \exp\left(-\frac{64}{9\pi}s^2\right). \end{aligned} \tag{3.48}$$

Recall from Section 3.1 that we define $P(n, s)$ as the probability that between two eigenvalues separated by a distance s there lie exactly $n-1$ other eigenvalues. Then a similar Wigner surmise approach gives [93]

$$P(n, s) = a_n s^{d_n} \mathrm{e}^{-b_n s^2}, \qquad d_n = n - 1 + \frac{1}{2}n(n+1)\beta \tag{3.49}$$

with a_n and b_n fixed by the normalization

$$\int_0^\infty P(n, s)\mathrm{d}s = 1, \qquad \int_0^\infty sP(n, s)\mathrm{d}s = n. \tag{3.50}$$

3.3.6 Distribution of ratios: a Wigner-like surmise

By analogy with the Wigner surmise for nearest-neighbour spacings obtained from exact calculations for 2×2 matrices, we proposed in [OG036] a surmise for the distribution of ratios (3.9), obtained from the joint distribution (3.26) by performing the exact calculation for 3×3 matrices. The surmise was shown to take the form

$$P(r) = \frac{1}{Z_\beta}\frac{(r + r^2)^\beta}{(1 + r + r^2)^{1+\frac{3}{2}\beta}}, \tag{3.51}$$

with Z_β the normalization constant given by

$$\frac{8}{27} \qquad \text{(GOE)} \tag{3.52}$$

$$\frac{4}{81}\frac{\pi}{\sqrt{3}} \qquad \text{(GUE)} \tag{3.53}$$

$$\frac{4}{729}\frac{\pi}{\sqrt{3}} \qquad \text{(GSE)}. \tag{3.54}$$

Similarly as the Wigner surmise (3.46), these expressions reproduce very accurately large–N numerical computations for the Gaussian random ensembles (see Fig. 3.3).

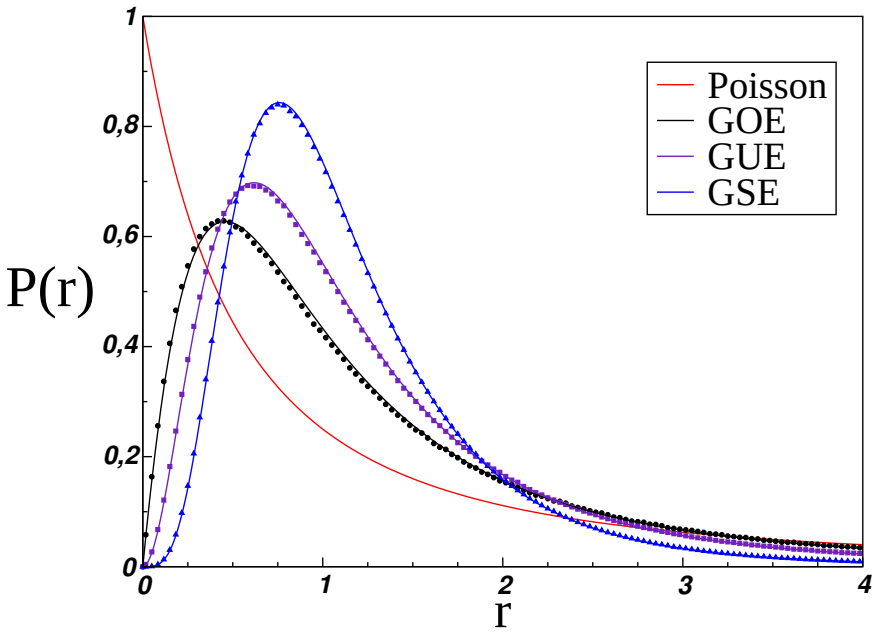

Figure 3.3: Ratio distributions $P(r)$ for 10^5 matrices of size 1000×1000 (black points: GOE, violet: GUE, blue: GSE). Full lines are the surmise (3.51) for random matrices, and (3.23) for Poisson variables (from [OG036]).

The absolute difference $\delta P(r) = P_{\rm num}(r) - P_W(r)$ between large–N numerics and the surmise (3.51) has a maximum relative deviation of about 5% (see Fig. 3.4), which is of similar order of magnitude as the Wigner surmise for $P(s)$ [92]. In a similar way, exact analytic expressions for 4×4 matrices were explicitely derived in [OG037], further reducing the difference $\delta P(r)$ (up to a factor 10 for GUE). The exact 4×4 result reads

$$P(r) = \frac{1}{4\pi}\left[f(r) + \frac{1}{r^2} f\left(\frac{1}{r}\right)\right], \tag{3.55}$$

where f is the function

$$f(r) = \frac{r^2(r+1)^2\left[-(r+2)Q_1(r) + 9\sqrt{3}(4+4r+3r^2)^4\sqrt{4+4r+3r^2}\,Q_2(r)\right]}{(1+r+r^2)^7(4+4r+3r^2)^{9/2}} \tag{3.56}$$

with polynomials Q_1 and Q_2 given by

$$\begin{aligned} Q_1(r) &= 41664 + 291648r + 946144r^2 + 1885440r^3 + 2588464r^4 + 2610064r^5 \\ &+ 2182624r^6 + 1894048r^7 + 1973866r^8 + 2026558r^9 + 1687399r^{10} \\ &+ 1037676r^{11} + 449635r^{12} + 124362r^{13} + 17766r^{14}, \\ Q_2(r) &= 14 + 42r + 39r^2 + 8r^3 + 39r^4 + 42r^5 + 14r^6. \end{aligned} \tag{3.57}$$

An alternative way of improving the surmise was also proposed in our publication [OG036]. It consists of a simple expression which perfectly fits the remaining differ-

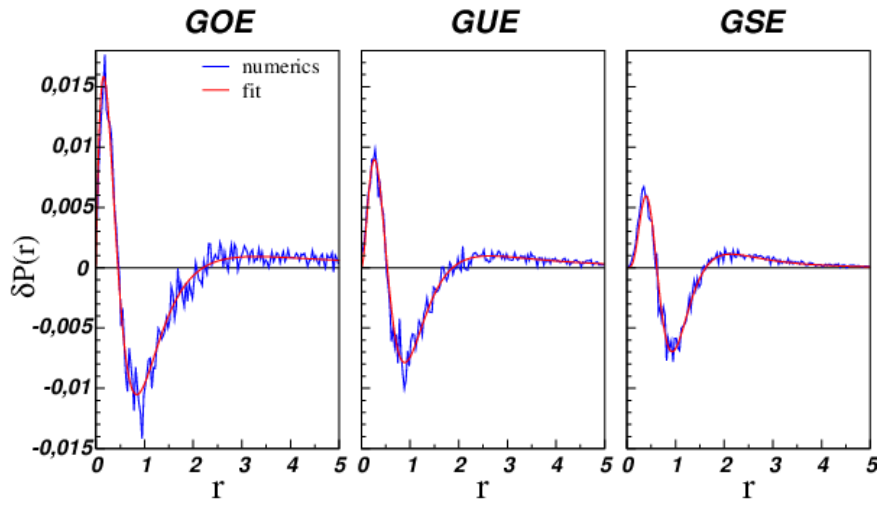

Figure 3.4: Difference $\delta P(r) = P_{\rm num}(r) - P_W(r)$ between numerically obtained $P(r)$ and the Wigner-like surmise (3.51), same data as Fig. 3.3. Smooth curve is the heuristic expression (3.58).

ence (see Fig. 3.4):

$$\delta P_{\rm fit}(r) = \frac{C}{(1+r)^2}\left[\left(r+\frac{1}{r}\right)^{-\beta} - c_\beta\left(r+\frac{1}{r}\right)^{-(\beta+1)}\right], \tag{3.58}$$

where C is the normalization constant and c_β, imposed by the condition $\int_0^\infty \delta P(r)dr = 0$, reads

$$\text{GOE} \qquad c_\beta = 2\tfrac{\pi-2}{4-\pi} \tag{3.59}$$

$$\text{GUE} \qquad c_\beta = 4\tfrac{4-\pi}{3\pi-8} \tag{3.60}$$

$$\text{GSE} \qquad c_\beta = 8\tfrac{32-9\pi}{45\pi-128}. \tag{3.61}$$

Exact asymptotic expressions for $P(s)$ and $P(r)$ at large matrix size can be found. As we showed in [OG037], starting from Eq. 5.4.29 of Mehta [72] one can check that the probability $p(-t, y, t)$ of having three consecutive levels at points $-t, y, t$ can be rewritten as

$$p(-t, y, t) = \det(1-K)\det[R(x,z)_{x,z=-t,y,t}], \tag{3.62}$$

where $R(x, y)$ is the resolvent kernel, i.e. the kernel of the operator $(1-K)^{-1}K$, and $\det(1-K)$ is the Fredholm determinant of K. Here K is an integral operator whose action is defined as

$$(Kf)(x) = \int_{-t}^{t} K(x,y)f(y)\mathrm{d}y \tag{3.63}$$

with the kernel

$$K(x,y) = \frac{\sin\pi(x-y)}{\pi(x-y)}. \tag{3.64}$$

It is known (see e.g. [94]) that for a kernel of this form the resolvent kernel can be written as

$$R(x,y) = \frac{Q(x)P(y) - Q(y)P(x)}{x-y}, \tag{3.65}$$

with functions $Q(x)$ and $P(x)$ obeying integral equations

$$\begin{aligned} Q(x) - \int_{-t}^{t} K(x,y)Q(y)\mathrm{d}y &= \frac{\sin \pi x}{\pi}, \\ P(x) - \int_{-t}^{t} K(x,y)P(y)\mathrm{d}y &= \cos \pi x. \end{aligned} \tag{3.66}$$

In [OG036] we computed the quantity $\det(1-K)$ via a quadrature method for numerical evaluation of the integrals

$$\int_{-t}^{t} f(x)dx = \sum_{k=1}^{m} w_k f(x_k) \tag{3.67}$$

appearing in the definition (3.63) of the integral operator K [95]. Such a discretization allowed us to approximate the determinant of the integral operator as a finite $m \times m$ determinant

$$\det(1-K) \approx \det\left(\delta_{jk} - K(x_j,x_k)w_k\right), \tag{3.68}$$

and functions $Q(x)$ and $P(x)$ defined in (3.66) can be obtained by solving a linear system of m equations. This allowed us to estimate more precisely the discrepancy between large–N expressions and our surmise (3.51).

3.4 Intermediate systems

Among the vast class of systems whose classical dynamics is neither integrable nor chaotic, it may be possible to identify a third universality class of systems which have intermediate features. At a classical level, these systems have a non-chaotic dynamics which might be affected by discontinuities in the phase space Hamiltonian flow, leading to diffraction in the quantum regime. At the quantum level, their nearest-neighbour statistics exhibits level repulsion

$$P(s) \sim_{s\to 0} s^{\alpha}, \qquad \alpha > 0, \tag{3.69}$$

reminiscent of that of the Wigner-Dyson distribution (3.48), but it decreases exponentially at large argument, as the Poisson spacing distribution, namely

$$P(s) \sim_{s\to\infty} \exp(-as). \tag{3.70}$$

The value of the form factor $K(\tau)$ at $\tau \sim 0$ lies between 0 and 1, that is, intermediate between the Poissonian result $K(0) = 1$ and the Random Matrix value $K(0) = 0$. The number variance is linear in L, as in the Poisson case, but with a level compressibility which is smaller than 1 [96]:

$$\Sigma^2(L) \sim_{L\to\infty} \chi L, \qquad 0 < \chi < 1, \tag{3.71}$$

in accordance with the fact that $K(0) \in]0,1[$. The value of χ is expected to be a universal characteristic of the underlying critical theory.

A simple random sequence which has the characteristic behaviour (3.69)–(3.71) is easily obtained by constructing, from a sequence $x_1 \leq x_2 \leq ...$ of i.i.d. random variables, the subsequence $y_n = (x_n + x_{n+1})/2$ [48]. The sequence (y_n) then follows the so-called "semi-Poisson" law

$$P(s) = 4se^{-2s}. \tag{3.72}$$

Such a distribution is also obtained for the so-called *daisy* model with $y_n = x_{2n}$, that is, removing every second level [97]. More generally, semi-Poisson distributions can be obtained by considering a joint probability given by a Coulomb gas model of the form (3.27) but with a repulsion between particles restricted to the first neighbours, for instance

$$W(\lambda_1, \lambda_2, ..., \lambda_N) = -\frac{1}{4\sigma^2\beta}\sum_i \lambda_i^2 + \beta\sum_j \ln|\lambda_j - \lambda_{j+1}| \tag{3.73}$$

for nearest-neighbour interaction. In fact, the quadratic confinement λ_i^2 does not play any role asymptotically and could be replaced by any confining potential. For such a model, the nearest-neighbour spacing distribution is given for $N \to \infty$ by [73]

$$P(s) = a_\beta s^\beta e^{-(\beta+1)s}, \qquad a_\beta = \frac{(\beta+1)^{\beta+1}}{\Gamma(\beta+1)}. \tag{3.74}$$

The two-point form factor reads

$$K(\tau) = 1 + 2\mathcal{R}e\ \frac{1}{(1 + 2i\pi\tau/(\beta+1))^{\beta+1} - 1}, \tag{3.75}$$

so that the level compressibility is

$$\chi = \frac{1}{\beta+1}. \tag{3.76}$$

For $\beta = 1$, the two-point correlation function reads

$$R_2(s) = 1 - e^{-4s}, \tag{3.77}$$

and the number variance is given by

$$\Sigma^2(L) = \frac{L}{2} + \frac{1 - e^{-4L}}{8}, \tag{3.78}$$

which indeed follows (3.71) with $\chi = 1/2$. Similar expressions can be obtained for any β and for arbitrary (but constant) next-to-nearest interaction range [73].

Various types of systems with such intermediate features of spectral statistics have been identified. Some of these models correspond to a transition between integrable and chaotic systems when a parameter is varied. This is for instance the case certain two-dimensional Hamiltonians describing two particles in a potential [98, 99, 100], or the Moshe-Neuberger-Shapiro model of random matrices [101]. For

other systems, the intermediate nature seems to correspond to the presence of regular motion together with diffraction. For instance, a rectangular billiard with a potential of the form $V(r) = \lambda r^{-\alpha}$ at its center [102] has Poisson features for $\alpha < 2$ and Wigner-Dyson for $\alpha > 2$; at $\alpha = 2$, statistics become intermediate. In a similar way, an electron in a non-hydrogenoid atom in the presence of an external magnetic field displays an intermediate level statistics; the ionic nucleus plays the role of a diffracting center [103]. This is also the case for low-lying energy levels of the Kepler billiard, a rectangular billiard with a potential of the type $V(r) = \lambda e^{-\kappa r}/r$ centered at some point inside the billiard [104].

In the same spirit as the Wigner-Dyson approach, random matrix ensembles with critical spectral statistics were constructed. Most of them realize a crossover from Random matrix to Poisson statistics. Starting with Brody [105], many models have been proposed, such as the Rosenzweig-Porter model [106], based on a symmetry breaking of the RMT matrix distribution which singles out a preferential basis, or the Moshe-Neuberger-Shapiro model ([101] for GUE, [107] for the GOE case). The latter is based on a Coulomb gas model with quadratic potential $V(x) = x^2$, as in Wigner-Dyson RMT, to which a symmetry-breaking term of the form $\mathrm{tr}([U, H][U, H]^\dagger)$, with U a fixed unitary matrix, is added; varying the strength of this term allows to interpolate between Poisson and Wigner-Dyson statistics. On the other hand, other models, such as the short-range plasma model [48], keep the form of the Wigner-Dyson RMT distribution (3.29) but limit the logarithmic interaction to nearest-neighbours. This leads to a linear number variance and exponential decay of $P(s)$, as expected for integrable systems.

Such properties were also observed in Coulomb gas models with unitary invariance (no preferential basis) but logarithmic confining potentials [108, 109, 110, 111]; spectral correlation functions for a model with logarithmic potential $V(x) = (1/a)(\ln x)^2$ were shown to be of intermediate type and to fit perfectly correlation functions of the 3D Anderson model at criticality (as well as the level compressibility) for a certain value of a [109, 111]. This was generalized to Lévy-like ensembles with potential $V(x) \sim \mathrm{arcsinh}^{1+\lambda} x$ in [112]. Lévy ensembles, with random matrix entries drawn from a power-law $P(H_{ij}) \sim 1/|H_{ij}|^{1+\mu}, 0 < \mu < 1$ were introduced in [113], displaying intermediate statistics together with a mobility edge. The origin for the common features observed in the spectral properties of all these models, in particular in the near-RMT limit, where they share the same two-point correlation function, is discussed e.g. in [114]. Outside this regime, they still have very close properties: for instance, the level compressibility for PRBM was computed numerically in [115] and shown to be in remarkable agreement with the analytic expression for the Moshe-Neuberger-Shapiro model. However, virial expansion calculations [116] have shown that in the opposite (near-Poisson) limit the two models have different first-order contributions to the density of states.

My earliest contributions to the problem of finding examples of systems where intermediate statistics could be observed was concerned with quantum billiards. Billiards are two-dimensional closed compact domains which provide a testbed for quantum chaos ideas. Classical dynamics corresponds to the free motion of a point-like particle in the enclosure with hard walls and specular reflection at boundaries. Quantum-mechanically, the problem can be seen as that of a particle in a box.

Examples of integrable billiards include the circular billiard, or polygonal billiard paving the Euclidean plance. Among chaotic billiards, one of the most famous is the Bunimovich stadium billiard. Intermediate statistics can be observed in so-called pseudo-integrable billiards [117], [118], for instance in polygonal billiards where all angles are of the form $\pi m_i/n_i$, with m_i and n_i some positive integers. Periodic orbits of the billiard play a prominent role in the quantum-to-classical correspondence. This correspondence can be explicited via the semiclassical trace formulas, which relate the quantum spectrum to a sum over periodic orbits of the classical system. Since an integrable billiard has two constants of motion, a typical trajectory in phase space lies on a two-dimensional torus of genus 1. By constrast, a typical trajectory in a chaotic system covers ergodically the three-dimensional surface of constant energy. In pseudo-integrable billiards trajectories lie on two-dimensional surfaces but with higher genus ($g \geq 2$) [118]. The underlying classical dynamics is also reflected in the localization properties of wavefunctions. While wavefunctions are localized in integrable billiards and extended in chaotic ones, eigenstates of pseudo-integrable billiards are mixtures of scarred states [11].

In [OG001], using trace formulas, we have obtained analytical expressions for the value of the form factor at $\tau = 0$ for two different types of diffractive systems. For a billiard in the form of a right triangle with one angle equal to π/n, using the underlying mathematical structure allowing to characterize entirely the periodic orbits, we have obtained

$$\chi = K(0) = \frac{n + \epsilon(n)}{3(n-2)} \tag{3.79}$$

with $\epsilon(n) = 0$ when n is odd, 2 when n is even not divisible by 3, and 6 when n is even and divisible by 3. For a rectangular billiard with an Aharonov-Bohm flux line at some point inside the rectangle, described by a potential given in polar coordinates centered at the flux by $A_\varphi = \alpha/r$, the form factor at $\tau = 0$ is given by

$$K(0) = 1 - 3\bar{\alpha} + 4\bar{\alpha}^2 \tag{3.80}$$

when the coordinates of the flux line are non-commensurate with the corresponding sides (and more cumbersome explicit expressions in the commensurate case) [OG001]. Here $\bar{\alpha}$ is the fractional part $\{\alpha\}$ of the flux if $0 \leq \{\alpha\} \leq 1/2$ and $\bar{\alpha} = 1 - \{\alpha\}$ if $1/2 \leq \{\alpha\} \leq 1$. In [OG007] I investigated a family of rectangular billiards with a barrier of height irrational with respect to the side of the billiard and located at any rational position p/q from the side. These billiards are pseudo-integrable but with an underlying mathematical structure which is different from that of the previous examples above. I showed in [OG007] that for these billiards $K(0) = 1/2 + 1/q$.

If the flux line or the barrier inside the rectangle is replaced by a small scattering impurity, a scattering version of the semiclassical trace formula allowed us to calculate analytically all orders of the series expansion of $K(\tau)$, both for periodic and Dirichlet boundary conditions on the rectangular billiard [OG002], as well as the nearest-neighbour spacing distribution $P(s)$ [OG003]. In particular the spacing distribution is shown to decrease as (3.70). These results show that such a scattering system is of intermediate nature.

However, the complexity of calculations does not give any hope when it comes to investigation of eigenstates. This is why I then concentrated on the more tractable approach of quantum maps, the framework of which I will now present.

Chapter 4

Quantum maps and random matrix ensembles

Quantum maps provide simple toy models to investigate properties of quantum systems, in particular the validity of the conjectures of quantum chaos, and properties of systems at criticality. Their spectral statistics is more easily accessible analytically, while numerical investigation of their wavefunction properties is feasable by simple diagonalization. This allows to make new predictions for more realistic systems. Moreover, for many of the systems that we will consider, the critical model depends on a parameter, so that there is a whole line of criticality. This allows to investigate situations from the almost integrable, or almost localized, case, to the almost chaotic, or almost extended, case.

In this chapter we shortly review, among various models that have been proposed in the literature, those which will be useful for our subsequent discussion. We then introduce the models that we have been investigating and discuss their spectral properties.

4.1 Chaotic maps

4.1.1 Cat maps

Among the simplest examples of linear maps, the classical cat map is defined on the torus $\mathbb{T}^2 = \mathbb{R}^2/\mathbb{Z}^2$ as

$$\begin{pmatrix} \bar{q} \\ \bar{p} \end{pmatrix} = \begin{pmatrix} t_{11} & t_{12} \\ t_{21} & t_{22} \end{pmatrix} \begin{pmatrix} q \\ p \end{pmatrix} \qquad (\text{mod } 1), \tag{4.1}$$

where $(t_{ij})_{1\leq i,j\leq 2}$ is a matrix with integer entries, unit determinant and such that $|t_{11} + t_{22}| > 2$ [119]. Here and below, $(\bar{q}, \bar{p})$ is the image of (q, p) after one iteration of the map. The quantization of a torus map associates with it a unitary operator acting on the N-dimensional Hilbert space of functions $\psi : \mathbb{Z}_N \to \mathbb{C}$ with inner product $\langle\psi|\phi\rangle = N^{-1}\sum_{Q=0}^{N-1}\psi^*(Q)\phi(Q)$. Here $\mathbb{Z}_N = \mathbb{Z}/N\mathbb{Z}$ denotes the integers modulo N, and N has the physical interpretation of an inverse Planck's constant. The quantized version of the cat map (4.1) is an $N \times N$ unitary matrix U, with

$N = 1/(2\pi\hbar)$, given by [53]

$$U_{qq'} = \sqrt{\frac{t_{12}}{iN}} \langle e^{\frac{i\pi}{Nt_{12}}\left(2t_{11}q^2 - 2q(q'+Nm) + t_{22}(q'+Nm)^2\right)} \rangle_m. \tag{4.2}$$

Trace formulas can relate the density of eigenphases (3.15) to a sum over periodic orbits of the classical system via a Poisson summation formula. It turns out that for such systems periodic orbit sums can be performed analytically, yielding analytic expressions for spectral statistics. For instance the number variance $\Sigma^2(L)$ defined in (3.11) can be expressed as a simple function of L, involving number-theoretic properties of the Hilbert space dimension N. Detailed investigation [119] has shown that these statistics differ from the ones expected for quantum chaotic systems, due to the high degeneracy of long periodic orbits. However, thanks to its relative simplicity this toy model allows to precisely understand how the underlying classical structure affects quantum properties.

4.1.2 Baker maps

In a similar spirit, the Baker's map, defined on the torus by

$$\begin{pmatrix} \bar{q} \\ \bar{p} \end{pmatrix} = \begin{pmatrix} 2q \\ p/2 \end{pmatrix} \quad \text{if } 0 \le q < 1/2, \qquad \begin{pmatrix} 2q-1 \\ (p+1)/2 \end{pmatrix} \quad \text{if } 1/2 \le q < 1, \tag{4.3}$$

was originally quantized in [120]. A slightly different quantization [121] allows to restore the classical phase space symmetry. Following [121], the quantum map can be expressed as

$$U_{qq'} = F_N \begin{pmatrix} F_{N/2} & 0 \\ 0 & F_{N/2} \end{pmatrix}, \tag{4.4}$$

for N a power of 2; here F_N is the $N \times N$ Fourier transform defined by $(F_N)_{qq'} = \frac{1}{\sqrt{N}} \exp(-\frac{2i}{N}(q+\frac{1}{2})(q'+\frac{1}{2}))$. Such a system, because of its simplicity, has allowed to investigate in great detail the correspondence between classical and quantum features. More recently, it has been used as a toy model of quantum information to illustrate implementation of simple quantum maps [122] and to investigate entangling properties of chaotic systems [123].

4.1.3 Kicked systems

Kicked systems are among the best-studied area-preserving maps. They are defined by their classical dynamics, given by the following Hamiltonian

$$H(q,p) = \frac{p^2}{2} + V(q) \sum_n \delta(t - nT). \tag{4.5}$$

It describes the dynamics of a particle undergoing free motion and periodically kicked (with period T) with a strength $V(q)$ which depends on its position. In the case of a kicked rotor, the particle is constrained to a finite interval with periodic boundary conditions (a ring), so that $q \in [0, 2\pi[$ and $V(q)$ is a periodic function with period

2π [124]. The Hamilton-Jacobi equations of motion can then be integrated over a period of time, yielding the classical map

$$\begin{aligned} \bar{p} &= p - V'(q) \\ \bar{q} &= q + \bar{p} \qquad\qquad (\text{mod } 2\pi). \end{aligned} \tag{4.6}$$

Starting from a point $(q_0, p_0 + 2k\pi)$ with k some integer number, the first iterate is given by $p_1 = p_0 + 2k\pi - V'(q_0)$ and $q_1 = q_0 + p_0 - V'(q_0)$ (mod 2π). Repeating the process, we see that the dynamics in the variable q is not modified by the value of k, so that the phase picture of the map repeats itself in the p direction with a period 2π. One can therefore restrict the study of the classical map to the torus $[0, 2\pi]^2$.

The quantum evolution operator $\hat{U}(t) = \exp(-i \int^t \hat{H}/\hbar)$, where $\hat{H}$ is the quantization of the Hamiltonian (4.5), is the quantum version of the classical map (4.6), and can be integrated over a time period of the map. It can be decomposed into a free motion propagator $\exp(-i\hat{p}^2/(2\hbar))$ between two kicks and a quantification of the kick $\exp(-iV(\hat{q})/\hbar)$, so that

$$\hat{U} = \exp(-i\hat{p}^2/(2\hbar)) \exp(-iV(\hat{q})/\hbar) \tag{4.7}$$

in mixed position-momentum representation [125, 53, 126, 127]. Note that the free motion propagator is diagonal in position representation, while the kick is diagonal in momentum representation. This feature makes these systems very convenient for numerical investigation of the evolution of a wave packet, as one can easily go from a representation to the other by fast Fourier transform.

In the momentum basis, the kick reads

$$\langle p'|e^{-iV(\hat{q})/\hbar}|p\rangle = \frac{1}{2\pi} \int_{-\infty}^{\infty} dq e^{i(p'-p)q/\hbar - iV(q)/\hbar} \tag{4.8}$$

which, in view of the periodicity of $V(q)$, vanishes unless $p' - p = n\hbar$ for some integer n. Thus, a kick applied to a wavefunction localized in the momentum basis, $|p\rangle = |\hbar(n+\beta)\rangle$, with n an integer and $0 \leq \beta < 1$, does not change β. Since the free motion part of the evolution is diagonal in the momentum basis, the action of $\hat{U}$ on such a wavefunction does not change the value of β: the quantity β (the "quasi-momentum") is conserved under the quantum map evolution. Therefore we can consider separately states with fixed quasi-momentum. If an initial state is localized in momentum, the quantum dynamics is thus restricted to a Dirac comb with spacing $\hbar$. Numerically, this comb has to be truncated. Let N be the number of teeth of the comb that are kept, that is, let $[0, N\hbar[$ be the interval of p values which is kept. In order that the map dynamics be unaffected by the truncation, this truncation should correspond to a periodicity in p; we thus need to have $\exp(-ip^2/(2\hbar)) = \exp(-i(p + N\hbar)^2/(2\hbar))$ for all $p = n\hbar, 0 \leq n \leq N-1$. This is equivalent to having for some integer k the relation $\hbar = 2k\pi/N$ if N is even, or $\hbar = 4k\pi/N$ if N is odd. For those values of $\hbar$, it is thus possible to truncate the phase space without making any approximation. For instance, taking $k = 1$, this amounts to keeping a single classical cell of size 2π (for even N) or two classical cells (for N odd). In that case, the system is periodic in p, so that the positions $q \in [0, 2\pi]$ can in turn be restricted

to a discrete set, with the comb in q having teeth spaced by $2\pi/N$. The operator $\hat{U}$ then becomes an $N \times N$ matrix labeled by integer indices P (in momentum representation) or Q (in position representation) with $0 \leq P, Q \leq N-1$, such that $p = P\hbar$ and $q = 2\pi Q/N$. It is such finite-size matrices that we will consider here. If $\hbar$ is irrational with respect to π, the kinetic term is no longer periodic and truncation at $N\hbar$ induces an approximation: the matrix U is no longer unitary. Note that in experimental realizations of the kicked rotor $\hbar$ is in fact an effective Planck constant which can be tuned at will (see e.g. [34]).

4.2 Localization-delocalization transition

4.2.1 Anderson model

The original Anderson model was proposed by Anderson in 1958 [2] to describe the motion of an electron in a disordered solid. It is described by the Hamiltonian

$$H = \sum_i \epsilon_i a_i^\dagger a_i + \sum_{<i,j>} a_j^\dagger a_i \tag{4.9}$$

where $\langle i, j \rangle$ are nearest neighbours on a d-dimensional lattice. Written in matrix form, the 1D map reads

$$\begin{pmatrix} \epsilon_1 & V & 0 & \cdots & \\ V & \epsilon_2 & V & 0 \cdots & \\ 0 & V & \epsilon_3 & V & 0 \\ \vdots & & \ddots & \ddots & \end{pmatrix}, \tag{4.10}$$

with $V = 1$ being the tight-binding coefficient bewteen neighbouring sites and ϵ_i the onsite disorder, given by independent random variables usually taken as uniformly distributed between $-W/2$ and $W/2$. In 1D, eigenvectors of (4.10) are localized for any strength of disorder (see the illustration in Fig. 4.1).

For $d = 3$, there is a transition for a critical value W_c of the strength of disorder W. For $W > W_c$, eigenfunctions are exponentially localized, which corresponds to an insulating behaviour. Correspondingly eigenvalues have a statistics which tends for large system sizes to that of Poisson random variable: this can be understood by the fact that states with nearby energies are typically localized at distances of the order of the size of the sample (as illustrated for $d = 1$ in Fig. 4.1), so that when the system size goes to infinity eigenfunctions do not interact. For $W < W_C$, there is a mobility edge E_c such that around the band centre $|E| < E_c$ states are extended, while eigenvalues behave (for large system size) according to random matrix statistics (outside this energy interval, eigenfunctions are localized and eigenlevels behave as independent random Poisson variables). Many works have looked numerically for the phase diagram of localization and the value of W_c, obtaining typically a value $W_c \simeq 16.3 \pm 0.5$ at the band centre for box-distributed onsite disorder [128]. On the insulating side, the localization length approaches the mobility edge as a power-law $\xi \sim |E_c - E|^{-\nu}$. On the metallic side, the diffusion constant decays according to a power law $D \sim |E_c - E|^s$. Values of ν have been obtained experimentally [34, 35], yielding $\nu = 1.4 \pm 0.3$, while numerical simulations have given $\nu = 1.57 \pm 0.02$

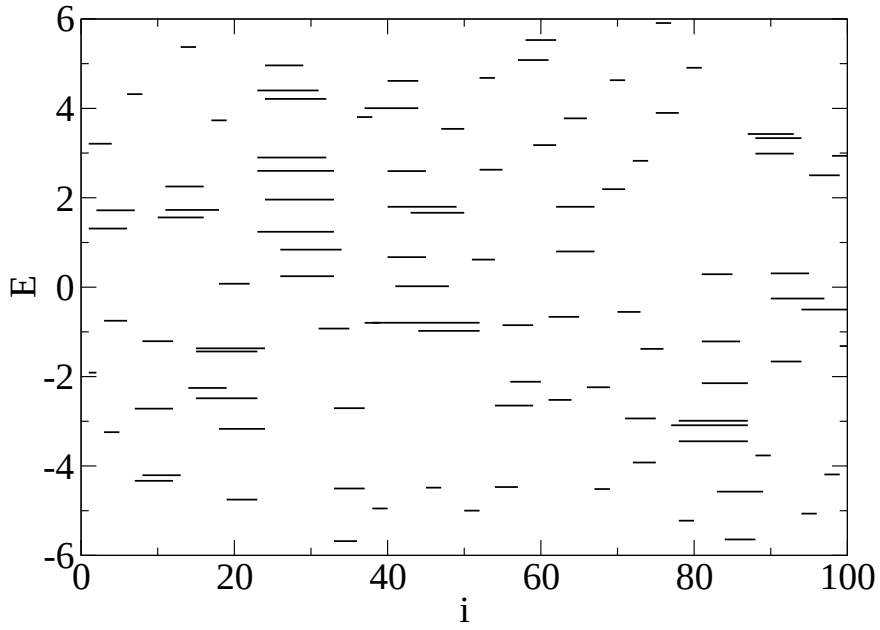

Figure 4.1: Localization width of eigenvectors of the map (4.10) for $W = 10$ and $N = 100$; each segment represent the position of indices i such that $|\psi_i| > 0.1 \max_j |\psi_j|$; its y-position is the corresponding eigenvalue.

[26]. For cold atoms in a disordered speckle, measurement of the mobility edge was achieved experimentally very recently [129], with results differing from numerical simulations [130].

Level statistics in the vicinity of the Anderson transition in $d > 2$ dimensions was investigated in [131], and shown to differ from Wigner-Dyson and Poisson statistics. The behaviour of the system at the transition is expected to be size-independent, and universal, that is, it should not depend on its microscopic structure [47, 132]. Nevertheless, the universal behaviour of the spectral statistics $P(s)$ and $\Sigma^2(L)$ for this system depends on boundary conditions [132].

4.2.2 Banded matrices

Anderson [2] and Levitov [133, 134] considered a generalized Anderson model with power-law long-range hopping term $V(\mathbf{r} - \mathbf{r}') = 1/|\mathbf{r} - \mathbf{r}'|^\alpha$. It was found that a transition occurs in dimension d at the critical value $\alpha = d$.

In order to model such systems, a simpler toy model, the power-law random banded matrix ensemble (PRBM) was introduced in [12]. It was inspired from earlier random banded matrix ensembles with exponential decay describing the transition from integrability to chaos [135].

The PRBM model is defined as a symmetric or Hermitian matrix M whose elements M_{mn} are independently distributed Gaussian random variables with zero

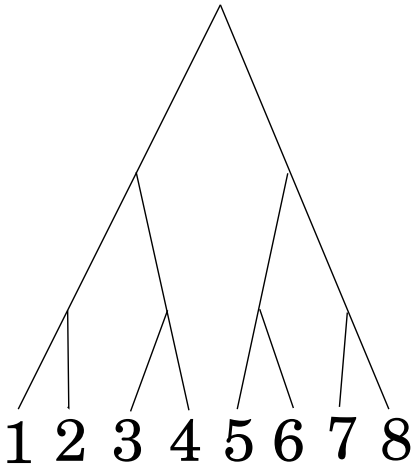

	1	1/2	1/2	1/4	1/4	1/4	1/4
1		1/2	1/2	1/4	1/4	1/4	1/4
1/2	1/2		1	1/4	1/4	1/4	1/4
1/2	1/2	1		1/4	1/4	1/4	1/4
1/4	1/4	1/4	1/4		1	1/2	1/2
1/4	1/4	1/4	1/4	1		1/2	1/2
1/4	1/4	1/4	1/4	1/2	1/2		1
1/4	1/4	1/4	1/4	1/2	1/2	1	

Figure 4.2: Left: Binary tree of depth $n = 3$; leaves are labeled by integers from 1 to 2^n. Right: matrix of variances (4.13)–(4.14).

mean and variance given by

$$\begin{aligned} \langle |M_{nn}|^2 \rangle &= \frac{1}{\beta}, \\ \langle |M_{mn}|^2 \rangle &= \frac{1}{2}\left[1 + \left(\frac{m-n}{g}\right)^{2c}\right]^{-1}, \quad m \neq n, \end{aligned} \tag{4.11}$$

with $\beta = 1$ for real symmetric matrices and $\beta = 2$ for complex Hermitian matrices. At $c < 1$ states are delocalized, and at $c > 1$ they are localized with power-law tails $|\psi(r)|^2 \propto r^{-2c}$ [12]. A transition takes place at the critical value $c = 1$. The parameter g gives the width of the band around the diagonal. It can be varied continuously, yielding a one-parameter family of critical models. Spectral properties for this model are reviewed in [21]. A periodic version of (4.11) has also been considered in the literature [136, 137]. In this model the variance of off-diagonal elements is given by

$$\langle |M_{mn}|^2 \rangle = \left[1 + \frac{\sin^2(\pi(m-n)/N)}{g^2(\pi/N)}\right]^{-1}, \quad m \neq n. \tag{4.12}$$

In a similar way, the ultrametric ensemble [14] is defined as the set of $2^K \times 2^K$ Hermitian matrices with independent Gaussian entries with zero mean and variance given by

$$\langle |H_{nn}|^2 \rangle = W^2 \tag{4.13}$$

for diagonal elements,

$$\langle |H_{mn}|^2 \rangle = 2^{2-d_{mn}} J^2 \tag{4.14}$$

for off-diagonal ones, with d_{mn} = the ultrametric distance between m and n along the binary tree, as illustrated in Fig. 4.2.

4.2.3 Dynamical localization

There is a correspondence between the kicked rotor (4.7) and the Anderson model (4.10), which goes as follows [138, 139]. Let us consider the system in a state $\psi^-(q)$, just before the kick, that would be an eigenvector of the operator $\hat{U}$ given by (4.7), with eigenvalue $e^{-i\omega}$, and let $\psi^+(q)$ be the state just after the kick. We have

$$\psi^+(q) = e^{-iV(\hat{q})/\hbar}\psi^-(q) \tag{4.15}$$

$$\psi^-(q) = e^{-i\hat{p}^2/(2\hbar)+i\omega}\psi^+(q) \tag{4.16}$$

Making the transformation

$$e^{-iV(q)/\hbar} = \frac{1+iW(q)}{1-iW(q)} \tag{4.17}$$

with $W(q)$ a Hermitian operator, or, equivalently, $W = -\tan(V/(2\hbar))$, Eq. (4.15) yields

$$\psi^{\pm}(q) = (1 \pm iW(q))\frac{\psi^+(q)+\psi^-(q)}{2}. \tag{4.18}$$

Writing both $W(q)$ and $\frac{1}{2}(\psi^+(q)+\psi^-(q))$ in the Fourier basis, with components respectively W_m and ψ_m, Eq. (4.16) gives

$$\psi_m - i\sum_n W_{m-n}\psi_n = e^{-im^2/(2\hbar)+i\omega}\left(\psi_m + i\sum_n W_{m-n}\psi_n\right), \tag{4.19}$$

which is equivalent to

$$\epsilon_m\psi_m + \sum_{n\neq m} W_{m-n}\psi_n = E\psi_m, \tag{4.20}$$

with $\epsilon_m = \tan(\omega - \frac{m^2/(2\hbar)}{2})$ and $E = -W_0$. This corresponds to a generalized Anderson model with onsite (pseudo-random) disorder ϵ_m and coupling W_n to the nth neighbour. The Anderson model (4.10) corresponds to taking a potential $V(q)$ such that only components $W_{\pm 1}$ are nonzero.

This correspondence allows to understand localization phenomena in kicked quantum maps. One of the best-studied models of kicked maps is the Chirikov standard map [140, 141], corresponding to $V(q) = K\cos q$. Classically, the phase space picture of the system depends on the parameter K, which governs its stochasticity. For small K the system is close to integrability; only small chaotic regions exist, and motion starting in such a region cannot escape it. For larger K only small regular islands survive in the chaotic sea. If K is large enough, namely $K > K_c$ for some critical value of the kicking strength, the motion becomes diffusive in momentum. More specifically, when averaging over initial conditions (p_0, q_0), the variance of the momentum p_t at time t scales as $\langle(p_t - p_0)^2\rangle \sim Dt$, where D is the diffusion constant. The quantized version of the kicked rotor is given by (4.7), that is,

$$\hat{U} = e^{-i\frac{\hat{p}^2}{2\hbar}}e^{-i\frac{K}{\hbar}\cos\hat{q}}. \tag{4.21}$$

The quantum mechanical dynamics is very different from the classical one: indeed, the mean momentum square $\langle \hat{p}^2 \rangle$ saturates to a finite value as time increases, a phenomenon known as dynamical localization. The eigenfunctions of U in momentum space are exponentially localized as $\psi_n \sim \exp(-|n - n_0|/\xi)$, with $\gamma_0 = 1/\xi$ the smallest Lyapunov exponent [142]. The interference effects destroy the momentum diffusion due to classical chaos. This can be understood via the mapping presented above between the kicked model and the Anderson model.

A variation of this model corresponds to the kicked Harper model. The Harper model is an integrable model describing electrons in a lattice in a strong magnetic field. In the kicked Harper model, the kinetic term $p^2/2$ in (4.5) is replaced by $L\cos(p)$ and $V(q) = K\cos q$ as in the standard map; it reduces to the Harper model in the limit where $K = L \to 0$ and displays a fractal spectrum ("Hofstadter butterfly"). Again, this model displays dynamical quantum localization in the regime of classical diffusion. Depending on the values of the two parameters, it can show different multifractal behaviours linked to specific transport properties [143]. Dynamical quantum localization with normal or anomalous classical diffusion was observed in several different kicked systems, such as the Chirikov typical map [144] or systems with non-analytic potential $V(q) = |q|^\alpha$ [19], the three-dimensional kicked rotor [145], and in "triangle maps" [146].

A different kind of model was developed in [147] in order to get an insight on the 3D Anderson transition using only one-dimensional maps. The potential $V(q)$ of the kick is now replaced by a time-dependent potential with ω_1 and ω_2 incommensurate, for instance

$$V(\theta, t) = K(1 + \epsilon \cos \omega_1 t \cos \omega_2 t) \cos \theta. \tag{4.22}$$

It can in fact be seen as a three-dimensional rotor, periodically kicked by a potential $V(\theta, \theta_1, \theta_2)$ depending on its position θ and on the value taken by two variables θ_i, $1 \leq i \leq 2$, evolving with constant velocity ω_i so that $\theta_i = \omega_i t$. Similarly as for the 1D rotor, one can show that the dynamics can be mapped onto an Anderson map (4.10), but the coupling to nearest-neighbour, which arises from the Fourier expansion of the potential, is now 3D. The pseudo-randomness of the onsite energy comes from the incommensurability of the ω_i. Of course, the great advantage is that the map itself is of the form (4.21): the evolution of a wave packet is the same as in a 3D model, but the numerical advantage is massive. In the localized regime eigenfunctions decay exponentially with localization length ξ, while in the extended regime $\langle (n-n_0)^2 \rangle \sim Dt$; both $1/\xi$ and D vanish at the critical transition point [147]. This model gained additional interest very recently as it was implemented on cold atoms and enabled to detect the Anderson transition experimentally [34, 35, 36]. The localization length critical exponent was found to be $\nu = 1.59 \pm 0.01$ from numerical simulations [148], in agreement to the one found for the 3D Anderson transition.

4.3 Intermediate maps

As explained above, many examples of chaotic maps were known and investigated as toy models for quantum chaos. We proposed for the first time in [OG006] an

example of a quantized map displaying intermediate statistics. It was found as the quantization of a one-parameter family of classical maps, whose spectral statistics turned out to be of a similar intermediate type as these observed in pseudo-integrable polygonal billiards (see Section 3.4).

4.3.1 Definition

The underlying classical map is defined on the torus $\mathbb{T}^2 = \mathbb{R}^2/\mathbb{Z}^2$ for any real constant γ by

$$\begin{aligned} \bar{p} &= p + \gamma \qquad (\text{mod } 1) \\ \bar{q} &= p + \bar{p} \qquad (\text{mod } 1). \end{aligned} \tag{4.23}$$

Up to multiplicative constants, it is of the same type as the kicked maps (4.6), with a sawtooth potential $V(q) = -\gamma\{q\}$, where $\{q\}$ denotes the fractional part of q. In particular, its quantization is given by Eq. (4.7). In momentum representation, for $N\gamma \notin \mathbb{Z}$, it reads

$$U_{PP'} = \frac{1}{N} e^{-2i\pi P^2/N} \frac{1 - e^{2i\pi N\gamma}}{1 - e^{2i\pi(P-P'+N\gamma)/N}}. \tag{4.24}$$

The classical map commutes with the map $p \mapsto p + \frac{1}{2}$. It turns out that for any α and $N \equiv 0 \bmod 4$, the quantum operator (4.24) commutes with $S = e^{i\pi N\{\hat{q}/2\}}$, so that an eigenstate $|\psi\rangle$ is such that either $S|\psi\rangle = |\psi\rangle$ or $S|\psi\rangle = -|\psi\rangle$. In order to investigate spectral statistics one thus treats the two subspectra separately.

4.3.2 Spectral properties

For irrational γ, the classical map is uniquely ergodic; in particular, there are no periodic orbits. Quantum mechanically the system displays quantum unique ergodicity: for *all* eigenstates, the expectation value of a quantum observable converges to the classical phase-space average of the corresponding classical observable [149]. The spacing distribution of the quantum operator resembles that of random matrices. As there is a time-reversal transformation which anti-commutes with U, namely $T = U_0^{1/2}\, C\, U_0^{-1/2}$, where C denotes the complex conjugation operator $C\psi := \psi^*$ and U_0 is the map (4.24) with $\gamma = 0$, the random matrix ensemble which describes the map for irrational γ is the Circular Orthogonal Ensemble (COE) expected for systems with chaotic classical limit and time-reversal symmetry [45, 150].

For rational $\gamma = a/b$, the classical motion can be identified with an interval-exchange transformation. When N (the matrix size) is divisible by b, the spectrum can be derived analytically and is highly singular [149]. If N is not divisible by b, the spacing distribution is intermediate between Poisson and RMT statistics, and the level compressibility takes values between 0 and 1. As mentioned in Section 3.1, the spectral form factor $K(\tau)$ in the limit $\tau \to 0$, or level compressibility, can be seen as a signature of intermediate statistics. In [OG006] we derived a heuristic analytical expression for the level compressibility, based on a number-theoretic analysis. The calculation consists in replacing the nth iterate of the quantized map, appearing in

(3.19), by the quantization of the nth iterate of the classical map (4.23), which can easily be calculated. Restricting ourselves to a subsequence of prime values of N in (3.21), this leads to $\chi \simeq 0$ for irrational γ, while for rational $\gamma = a/b$,

$$\chi = \lim_{n\to\infty} \lim_{\substack{N\to\infty \\ N \text{ prime}}} \frac{1}{n} \sum_{n'=1}^{n} K(n'/N) = \frac{1}{b}. \tag{4.25}$$

It can be noted that both the numerically computed level compressibility and the analytical calculation using (3.21) strongly depend on the number-theoretic properties of the matrix size N [OG006]. Note that we have also observed similar intermediate statistics for the triangle map defined in [151] and quantized in [146], but analytic calculations in that case would be much more involved.

To go beyond this heuristic calculation, it was proposed in [152] to replace the phases P^2/N in (4.24) by random phases ϕ_P. This defines an ensemble of random matrices given by

$$U_{PP'} = \frac{1}{N} e^{i\phi_P} \frac{1 - e^{2i\pi N\gamma}}{1 - e^{2i\pi(P-P'+N\gamma)/N}}. \tag{4.26}$$

The N phases ϕ_P, $1 \leq P \leq N$, are supposed to be either i.i.d. random variables ('non-symmetric' case) or random variables such that $\phi_{N-P} = \phi_P$ ('symmetric' case). It was shown in [152] that for $\gamma = a/b$ and matrices of size N such that $aN = \pm 1 \pmod b$, the spectral statistics is given by a semi-Poisson law (3.74) with $\beta = b - 1$ (non-symmetric case) or $\beta = b/2 - 1$ (symmetric case). A consequence of that is that the level compressibility is given by $\chi = 1/b$ (non-symmetric case) or $\chi = 2/b$ (symmetric case), which coincides with the result (4.25) for the non-random case. A generalization to cases where $aN = \pm r \pmod b$ was obtained in [23] using a transfer operator method. The nearest-neighbour spacing distribution was shown to be of the form

$$P(s) = \sum_{k=2}^{r(b-r)} a_k s^k e^{-bs} \tag{4.27}$$

in the non-symmetric case, and

$$P(s) = \sum_{k=1}^{r(b-r)-1} a_{k/2} s^{k/2} e^{-bs/2} \tag{4.28}$$

in the symmetric case, with a_i explicitely known constants. These distributions are all of intermediate type, with level repulsion at $s \sim 0$ and exponential decay.

4.3.3 Connection with the tight-binding model

The mapping between kicked maps and the Anderson model, detailed in Section 4.2.3, shows that a kicked map model corresponds to a tight-binding model with couplings given in momentum space by the coefficients W_{m-n} of the Fourier transform of $W(q)$ defined by (4.17). For a smooth potential such as $V(q) = \cos(q)$ the coefficients decrease exponentially, so that the corresponding tight-binding model has short-range interaction. For a potential with a discontinuity, such as $V(q) = -\gamma\{q\}$

considered here, the Fourier coefficients have a power-law decay, so that the properties of the map should be similar to those of the PRBM ensemble. As we will see in the next chapters, this is indeed the case.

In a similar spirit, a kicked map with step potential $V(x) = v_0$ constant inside the interval $[-a, a]$ and $V(x) = 0$ outside, for some fixed $a > 0$, was considered in [153]. It was found that in the region $\tan(v_0/2) \gg 1$ level-statistics is semi-Poisson and eigenstates are multifractal (see also [12] for a discussion of this point).

4.4 Maps from classical N-body integrable systems

The above intermediate kicked map turns out to have some connections with seemingly totally unrelated physical systems. In this section we will introduce ensembles of random Hermitian or unitary matrices constructed from the Lax matrices of classical integrable systems. We consider a system of N particles on a line, characterised by their positions q_i and their momenta p_i, with $1 \leq i \leq N$. Their dynamics is given by the Hamilton-Jacobi equations of motion, derived from a certain Hamiltonian $H(\mathbf{p}, \mathbf{q})$ which depends on the vector of positions $\mathbf{p} = (p_1, \ldots, p_N)$ and the vector of momenta $\mathbf{q} = (q_1, \ldots, q_N)$. The systems we consider here are classical integrable Hamiltonian systems.

4.4.1 Integrable systems

An N-dimensional integrable system is such that there exist N functions $\{I_1, ..., I_N\}$, defined on the $2N$-dimensional phase space of the system, which are time-independent and in involution. That is, $\forall i, \{I_i, H\} = 0$ and $\forall i, j, \{I_i, I_j\} = 0$, where $\{,\}$ denotes the Poisson bracket. The Hamiltonien H can then be expressed only as a function of the I_i. A canonical transform is a transform of variables (p_i, q_i) into variables (P_i, Q_i) which leave Hamilton equations invariant and verify the conditions

$$\begin{aligned} \{Q_i, Q_j\}_{p,q} &= 0 \\ \{P_i, P_j\}_{p,q} &= 0 \\ \{P_i, Q_j\}_{p,q} &= \delta_{ij}. \end{aligned} \tag{4.29}$$

Liouville theorem [154] states that a system is integrable if and only if there exists a canonical change of coordinates from $\{q_1, ..., q_N, p_1, ..., p_N\}$ to $\{I_1, ..., I_N, \varphi_1, ..., \varphi_N\}$ such that the Hamiltonian does not depend on the φ_i. Since the new variables (I, φ) fulfill Hamilton equations, then the I_i are N constants of motion and $\dot{\varphi}_i$ are some constants (the dot denotes time derivative). The dynamics can thus be easily integrated as

$$\varphi_i = \omega_i t + \varphi_{i0}, \quad 1 \leq i \leq N, \tag{4.30}$$

where $(\omega_1, ..., \omega_N)$ are N frequencies defined by $\omega_i(I_1, \ldots, I_N) = \nabla_i H(I_1, \ldots, I_N)$. Each trajectory in phase space is then confined to a torus labeled by $(I_1, \ldots, I_N)$.

A Lax pair [155] consists of two time-dependent functions L and M defined on phase space and belonging to some Lie algebra, such that the equations of motion (the Hamilton equations derived from the Hamiltonian) are equivalent to

$$\dot{L} = [M\,, L] \tag{4.31}$$

where $[,]$ is the Lie algebra bracket. If we consider an N-dimensional representation of the Lie algebra, then the Lax pair is a pair of $N \times N$ matrices L and M such that

$$\dot{L} = M\,L - L\,M. \tag{4.32}$$

Equation (4.32) implies in particular that the eigenvalues of L are time-independent, and therefore $\mathrm{tr}L^k$ are conserved quantities. For any system for which a Lax pair can be exhibited, constants of motion can thus easily be constructed from eigenvalues of L. For any integrable Hamiltonian system, equations of motion can be put under Lax form (4.31), at least in the vicinity of generic phase space points [156]. However there is no systematic way to construct a Lax pair [157].

A characteristic property of the N-particle systems with Hamiltonian $H(\mathbf{p},\mathbf{q})$ which we consider here is the existence of an explicit construction of a Lax pair and an explicit canonical action-angle transformation for the system dynamics, with the actions being the eigenvalues of L. Here we construct random matrix ensembles defined by Lax matrices $L(\mathbf{p},\mathbf{q})$ of a given Hamiltonian $H(\mathbf{p},\mathbf{q})$, endowed with some measure

$$\mathrm{d}L = P(\mathbf{p}\,,\mathbf{q}\,)\,\mathrm{d}\mathbf{p}\,\mathrm{d}\mathbf{q}. \tag{4.33}$$

The action-angle transformation is canonical, so that the symplectic 2-form on the phase space is preserved. This allows to transform (4.33) into

$$\mathrm{d}L = \mathcal{P}(\boldsymbol{\lambda}\,,\boldsymbol{\phi}\,)\,\mathrm{d}\boldsymbol{\lambda}\,\mathrm{d}\boldsymbol{\phi} \tag{4.34}$$

where $\boldsymbol{\lambda} = (\lambda_1,\ldots,\lambda_N)$, the eigenvalues of L, are the action variables, and ϕ_i are the angle variables. Integration over $\boldsymbol{\phi}$ then yields the joint distribution of eigenvalues

$$P(\boldsymbol{\lambda}) = \int \mathcal{P}(\boldsymbol{\lambda}\,,\boldsymbol{\phi}\,)\mathrm{d}^N\boldsymbol{\phi}, \tag{4.35}$$

from which all statistical quantities can be calculated [OG022].

This choice of interpreting the Lax matrix of a classical system as a random matrix is motivated by the fact that for a certain Hamiltonian and a given choice of parameter and random distribution of (p_i, q_i), these Lax matrices exactly coincide with the intermediate map (4.26) (see section 4.4.5). Therefore, this construction can be considered as a generalization of the model described in 4.3.

For various models we were able to give analytic expressions for level statistics. We present with some detail this approach in the rational case. Other cases are studied in detail in [OG030], and only the results will be summarized.

4.4.2 Rational Calogero-Moser ensemble

The rational Calogero-Moser ensemble (CMr) is defined by the Hamiltonian

$$H(\mathbf{p}\,,\mathbf{q}\,) = \frac{1}{2}\sum_j p_j^2 + g^2 \sum_{j<k} \frac{1}{(q_j - q_k)^2}, \tag{4.36}$$

where g is a real constant [158]. The corresponding Lax matrix is a Hermitian matrix which reads

$$L_{kr} = p_r\delta_{kr} + \mathrm{i}g\frac{1-\delta_{kr}}{q_k - q_r}, \tag{4.37}$$

with δ the Kronecker symbol. The key property of these matrices is the following. Let U be the unitary matrix whose columns are eigenvectors of L, and λ_i its eigenvalues, so that

$$L = U \begin{pmatrix} \lambda_1 & & 0 \\ & \ddots & \\ 0 & & \lambda_N \end{pmatrix} U^\dagger. \tag{4.38}$$

Then the matrix defined by

$$Q \equiv U^\dagger \begin{pmatrix} q_1 & & 0 \\ & \ddots & \\ 0 & & q_N \end{pmatrix} U \tag{4.39}$$

is such that

$$Q_{\alpha\beta} = \phi_\alpha \delta_{\alpha\beta} - \mathrm{i}g \frac{1-\delta_{\alpha\beta}}{\lambda_\alpha - \lambda_\beta} \tag{4.40}$$

with ϕ_α defined as $\phi_\alpha \equiv Q_{\alpha\alpha}$. The action-angle variables can be shown to be given by the λ_α and ϕ_α respectively. The matrix Q can be seen as the dual matrix of L, with angles ϕ_α playing the role of momenta and actions λ_α the role of positions (and $g \to -g$). It is this duality property which allows to construct an ensemble of random matrices for which the joint distribution of eigenvalues can be derived analytically, as follows.

We define [OG022] the CMr random matrix ensemble as the set of matrices (4.37) with positions $\mathbf{q}$ and momenta $\mathbf{p}$ given by random variables with joint distribution

$$P(\mathbf{p}\,,\mathbf{q}\,) \sim \exp\left[-A\Big(\sum_j p_j^2 + g^2 \sum_{j\neq k} \frac{1}{(q_j - q_k)^2} \Big) - B \sum_j q_j^2 \right], \tag{4.41}$$

with A and B some positive constants. The quadratic terms correspond to a confining potential, while the inverse square term corresponds to repulsion between particles. This choice allows to cast the joint distribution under the form

$$P(\mathbf{p}\,,\mathbf{q}\,) \sim \exp(-A\mathrm{tr}L^2 - B\mathrm{tr}Q^2). \tag{4.42}$$

Using the duality property between matrices L and Q, the joint distribution of eigenvalues for this ensemble is easily expressed as

$$P(\boldsymbol{\lambda}) = C \exp\left[-A \sum_\alpha \lambda_\alpha^2 - g^2 B \sum_{\alpha\neq\beta} \frac{1}{(\lambda_\alpha - \lambda_\beta)^2} \right], \tag{4.43}$$

where C is the normalization constant containing the integrals over the ϕ_α.

The most probable distribution of the λ_i is readily obtained from (4.43): after rescaling $x_k = \lambda_k (Bg^2/A)^{-1/4}$, it corresponds to

$$x_k = 2 \sum_{j\neq k} \frac{1}{(x_k - x_j)^3}\ , 1 \leq k \leq N. \tag{4.44}$$

These are the Calogero relations, which turn out to be equivalent to the Stieltjes relations (3.30) for real x_i [159]. Thus asymptotically the density of eigenvalues is the same as for usual random matrices, i.e. the semi-circle law (3.38).

From the expression (4.43) for the joint distribution, one can guess a surmise for the nth nearest-neighbour spacing distributions $P(n, s)$,

$$P(n, s) = as^d \exp\left(-\frac{b}{s^2} - cs\right). \tag{4.45}$$

It depends on four parameters, two fitting constants depending on n and two constants fixed by the normalization (3.50). A characteristic property of (4.45) is the strong level repulsion $\sim \exp(-b/s^2)$ at small argument and the exponential decay $\sim \exp(-cs)$ at large argument, which are a signature of intermediate statistics. This heuristic surmise can be compared with calculations from numerical diagonalization of the matrices L. Since numerically distributions such as (4.41) are hard to implement, we chose to replace it by fixed values $q_j = j$, $j = 1, \ldots N$ and independent random Gaussian p_j with zero mean and variance 1. It is clear in Fig. 4.3 that despite this choice being quite different from the distribution (4.41), the analytic expression (4.45) works very well.

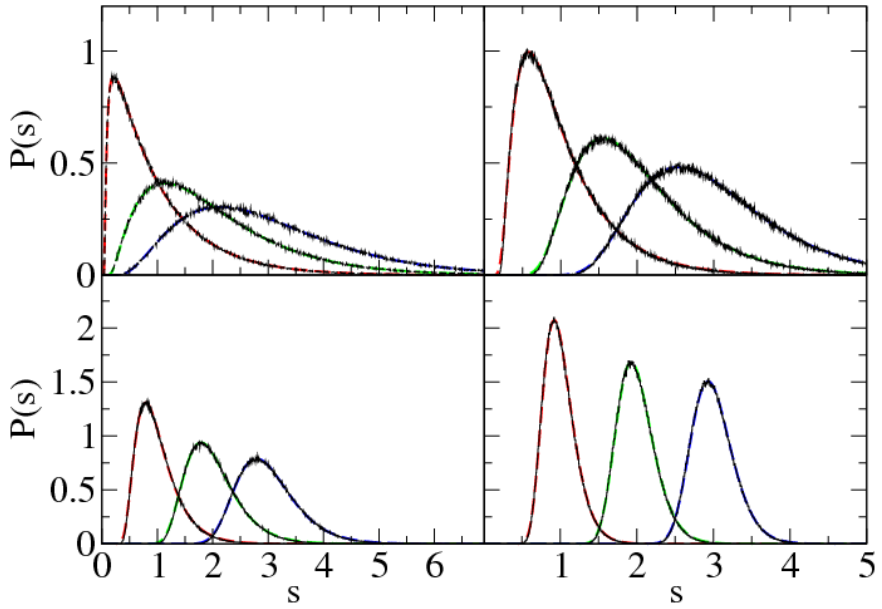

Figure 4.3: Nearest-neighbour distributions $P(n, s)$ for the random matrices of model CM_r with $g = 0.05$ (top left), 0.25 (top right), 0.5 (bottom left), and 1 (bottom right), averaged over the central quarter of the unfolded spectrum for 8000 realizations of matrices of size $N = 512$. Solid lines are numerical results, dashed lines indicate the fits (4.45) for $P(n, s)$ with (in each panel from left to right) $P(s) = P(1, s)$ (red), $P(2, s)$ (green) and $P(3, s)$ (blue).

4.4.3 Trigonometric Calogero-Moser ensemble

The trigonometric Calogero-Moser ensemble (CMt) is defined by the Hamiltonian

$$H(\mathbf{p}\,,\mathbf{q}\,) = \frac{1}{2}\sum_j p_j^2 + g^2 \sum_{j<k} \frac{\left(\frac{\mu}{2}\right)^2}{\sin^2[\frac{\mu}{2}(q_j - q_k)]}, \tag{4.46}$$

where g and μ are real constants. The corresponding Lax matrix is a Hermitian matrix which reads

$$L_{kr} = p_r\delta_{kr} + \mathrm{i}g\frac{1-\delta_{kr}}{\frac{2}{\mu}\sin[\frac{\mu}{2}(q_j - q_k)]}. \tag{4.47}$$

These matrices enjoy a duality property similar to that of the CMr ensemble. Diagonalizing L as in (4.38), matrix Q is now defined as

$$Q \equiv U^\dagger \begin{pmatrix} e^{i\mu q_1} & & 0 \\ & \ddots & \\ 0 & & e^{i\mu q_N} \end{pmatrix} U. \tag{4.48}$$

Introducing

$$V_\alpha(z) = \prod_{\beta\neq\alpha}\left(1 - \frac{z}{\lambda_\alpha - \lambda_\beta}\right), \tag{4.49}$$

one can show that Q can be written

$$Q_{\alpha\beta} = \mathrm{e}^{\mathrm{i}\mu\phi_\alpha/2} V_\alpha^{1/2}(-g\mu)\frac{g\mu}{\lambda_\alpha - \lambda_\beta + g\mu} V_\beta^{1/2}(g\mu)\mathrm{e}^{\mathrm{i}\mu\phi_\beta/2}, \tag{4.50}$$

where we have defined ϕ_α from the diagonal elements of Q as

$$Q_{\alpha\alpha} = V_\alpha(-g\mu)^{1/2} V_\alpha(g\mu)^{1/2}\mathrm{e}^{\mathrm{i}\mu\phi_\alpha}. \tag{4.51}$$

Again, action and angle variables are given by λ_α and ϕ_α respectively. An important property of the V_α defined in (4.49) is that

$$V_\alpha(g\mu) > 0, \qquad V_\alpha(-g\mu) > 0 \tag{4.52}$$

which for $g\mu > 0$ entails

$$\lambda_{\alpha+1} - \lambda_\alpha > g\mu \qquad \forall\alpha. \tag{4.53}$$

We then define the CMt random matrix ensemble as the set of matrices (4.47) with positions $\mathbf{q}$ and momenta $\mathbf{p}$ given by random variables with $q_j \in [0, 2\pi/\mu]$ and joint distribution

$$P(\mathbf{p}\,,\mathbf{q}\,) \sim \exp\left[-A\left(\sum_j p_j^2 + g^2\sum_{j\neq k}\frac{\mu^2}{4\sin^2[\frac{\mu}{2}(q_j - q_k)]}\right)\right], \tag{4.54}$$

with A some positive constant. This joint distribution can be cast under the form $\exp(-A\mathrm{tr}L^2)$.

Since the only restriction on the λ_α is the condition (4.53), the joint distribution of eigenvalues for this ensemble is then given, using (4.33)–(4.34), by

$$P(\boldsymbol{\lambda}) = C \exp\left(-A \sum_\alpha \lambda_\alpha^2\right) \chi(\boldsymbol{\lambda}), \tag{4.55}$$

where C is the normalization constant and

$$\begin{aligned} \chi(\boldsymbol{\lambda}) &= 1 \qquad \text{if } \lambda_1 < \lambda_2 < \ldots < \lambda_N \text{ and } \forall \alpha,\ \lambda_{\alpha+1} - \lambda_\alpha > \mu g \\ &= 0 \qquad \text{otherwise.} \end{aligned} \tag{4.56}$$

One can then derive the nearest-neighbour spacing distribution [OG030]

$$P(n,s) = \begin{cases} 0, & 0 < s < nb \\ \dfrac{(s-nb)^{n-1}}{(n-1)!(1-b)^n} \mathrm{e}^{-(s-nb)/(1-b)}, & s > nb, \end{cases} \tag{4.57}$$

with b some fitting constant.

Figure 4.4 shows the nearest-neighbour spacing distribution for numerically diagonalized matrices with $q_j = j$, $j = 1, \ldots N$ and p_j independent random Gaussian variables with zero mean and variance 1.

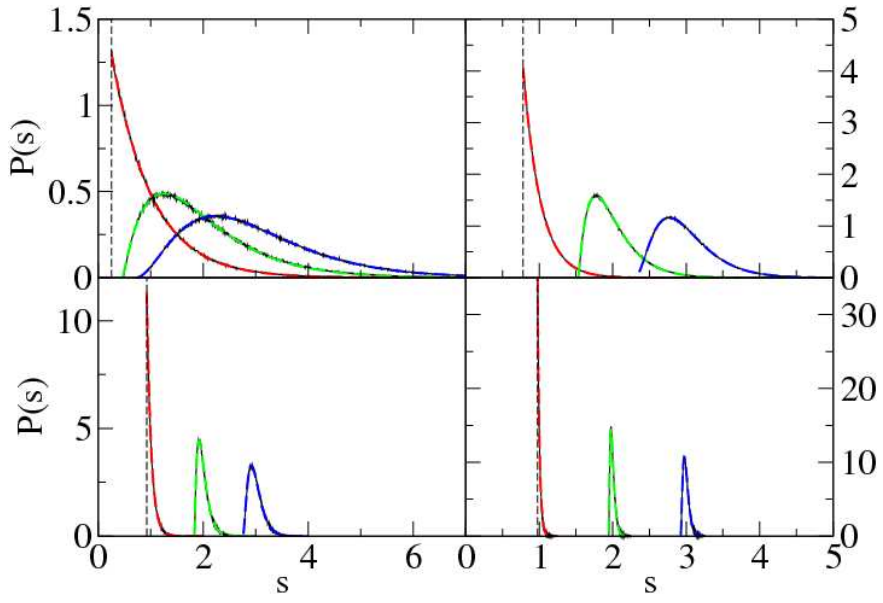

Figure 4.4: Nearest-neighbour spacing distributions $P(n,s)$ for the random matrices of model CM_t with $\mu = 4\pi/N$ and $g = 0.05$ (top left), 0.25 (top right), 0.5 (bottom left), and 1 (bottom right), averaged over the central quarter of the spectrum for 32000 realisations of matrices of size $N = 256$. Solid lines are numerical results, dashed lines indicate the fit (4.57) for $P(n,s)$ with (in each panel from left to right) $P(s) = P(1,s)$ (red), $P(2,s)$ (green) and $P(3,s)$ (blue).

4.4.4 Hyperbolic Calogero-Moser ensemble

The hyperbolic Calogero-Moser ensemble (CMh) is defined by the Hamiltonian

$$H(\mathbf{p}\,,\mathbf{q}\,) = \frac{1}{2}\sum_j p_j^2 + g^2 \sum_{j<k} \frac{\left(\frac{\mu}{2}\right)^2}{\sinh^2[\frac{\mu}{2}(q_j - q_k)]}, \tag{4.58}$$

where g and μ are real constants. The corresponding Lax matrix is a Hermitian matrix which reads

$$L_{kr} = p_r\delta_{kr} + \mathrm{i}g\frac{1-\delta_{kr}}{\frac{2}{\mu}\sinh[\frac{\mu}{2}(q_j - q_k)]}. \tag{4.59}$$

The CMh random matrix ensemble is then defined as the set of matrices (4.59) with positions $\mathbf{q}$ and momenta $\mathbf{p}$ given by random variables with $q_j \in [0, 2\pi/\mu]$ and joint distribution

$$P(\mathbf{p}\,,\mathbf{q}\,) \sim \exp\left[-A\Big(\sum_j p_j^2 + g^2\sum_{j\neq k}\frac{\mu^2}{4\sinh^2\left[\mu(q_j-q_k)/2\right]}\Big) - B\sum_j \cosh\mu q_j\right]. \tag{4.60}$$

with A and B some positive constants. The joint distribution of eigenvalues for this ensemble is then given by

$$P(\boldsymbol{\lambda}) = C\exp\left(-A\sum_\alpha \lambda_\alpha^2\right)\prod_\alpha K_0\left(B\prod_{\beta\neq\alpha}\Big|1+\frac{\mathrm{i}g\mu}{\lambda_\alpha-\lambda_\beta}\Big|\right) \tag{4.61}$$

where C is the normalization constant and $K_0(x)$ is the modified Bessel function of the second kind. One can then derive surmises for the nearest-neighbour spacing distributions

$$P(n,s) = as^d\exp\left(-\frac{b}{s} - cs\right), \tag{4.62}$$

an expression similar as Eq. (4.45) but with level repulsion $\sim \exp(-b/s)$ at small argument.

Figure 4.5 shows the nearest-neighbour spacing distribution for numerically diagonalized matrices with $q_j = j$, $j = 1, \ldots N$ and p_j independent random Gaussian variables with zero mean and variance 1.

4.4.5 Ruijsenaars-Schneider ensembles

The Ruijsenaars-Schneider ensemble (RS) is defined by the Hamiltonian

$$H(\mathbf{p}\,,\mathbf{q}\,) = \sum_{j=1}^N \cos(\sigma p_j)\prod_{k\neq j}\left(1 - \frac{\sin^2\left[\mu g/2\right]}{\sin^2\left[\mu(q_j-q_k)/2\right]}\right)^{1/2}, \tag{4.63}$$

where g, μ and σ are real constants [160]. The corresponding Lax matrix is a unitary matrix which reads

$$L_{kr} = \mathrm{e}^{\mathrm{i}\sigma p_k/2}\tilde{V}_k(-g\sigma)^{1/2}\frac{\sin\left[\mu g\sigma/2\right]}{\sin\left[\mu(q_k - q_r + g\sigma)/2\right]}\tilde{V}_r(g\sigma)^{1/2}\mathrm{e}^{\mathrm{i}\sigma p_r/2}, \tag{4.64}$$

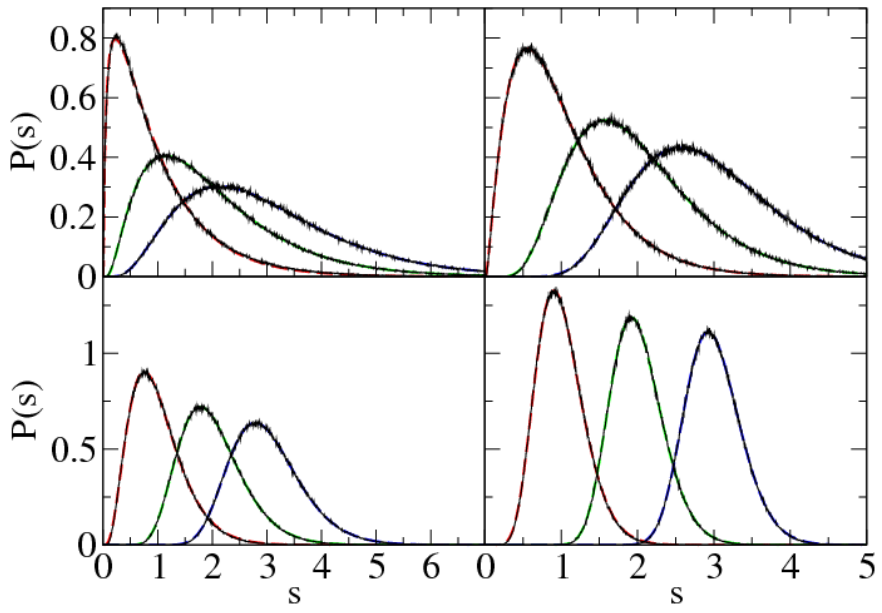

Figure 4.5: Nearest-neighbour spacing distributions $P(n,s)$ for the random matrices of model CM_h with $\mu = 4\pi/N$ and $g = 0.05$ (top left), 0.25 (top right), 0.5 (bottom left), and 1 (bottom right), averaged over the central quarter of the spectrum for 32000 realisations of matrices of size $N = 256$. Solid lines are numerical results, dashed lines indicate the fit (4.62) for $P(n,s)$ with (in each panel from left to right) $P(s) = P(1,s)$ (red), $P(2,s)$ (green) and $P(3,s)$ (blue).

with

$$\tilde{V}_k(z) = \prod_{j\neq k} \frac{\sin\left[\mu(q_k - q_j - z)/2\right]}{\sin\left[\mu(q_k - q_j)/2\right]}. \tag{4.65}$$

One has

$$H(\mathbf{p},\mathbf{q}) = \frac{1}{2}\mathrm{Tr}(L + L^\dagger). \tag{4.66}$$

We choose to denote eigenvalues of L as $\exp(i\sigma\lambda_\alpha)$. Defining Q as in (4.48), one can prove that

$$Q_{\alpha\beta} = \mathrm{e}^{\mathrm{i}\mu\phi_\alpha/2} V_\alpha(-g\mu)^{1/2} \frac{\sin\left[\sigma g\mu/2\right]}{\sin\left[\sigma(\lambda_\beta - \lambda_\alpha + g\mu)/2\right]} V_\beta(g\mu)^{1/2} \mathrm{e}^{\mathrm{i}\mu\phi_\beta/2} \tag{4.67}$$

with

$$V_\alpha(z) = \prod_{\beta\neq\alpha} \frac{\sin\left[\sigma(\lambda_\alpha - \lambda_\beta - z)/2\right]}{\sin\left[\sigma(\lambda_\alpha - \lambda_\beta)/2\right]}. \tag{4.68}$$

Phase variables ϕ_α are again defined from the diagonal elements of Q. From Eqs. (4.64) and (4.67) one sees that Q is the dual of L, with angles ϕ_α playing the role of momenta and actions λ_α the role of positions (and $g \leftrightarrow -g$).

The matrix L is unitary if and only if $\mathbf{q} \in \tilde{\Omega}$, where $\tilde{\Omega}$ is the set

$$\tilde{\Omega} = \left\{ \{q_1, \ldots, q_N\}; \forall k, \quad \text{sign } \tilde{V}_k(g\sigma) = \text{sign } \tilde{V}_k(-g\sigma) = \text{sign } \frac{\sin(N\frac{\mu g\sigma}{2})}{\sin(\frac{\mu g\sigma}{2})} \right\}. \quad (4.69)$$

The condition $\mathbf{q} \in \tilde{\Omega}$ is equivalent to the condition that the sets $\{\mu q_j, 1 \leq j \leq N\}$ and $\{\mu q_j + \sigma\mu g, 1 \leq j \leq N\}$, intertwine on the unit circle. By duality, unitarity of Q, implied by its definition (4.48), is equivalent to a similar restriction on the values of λ_α, that is, the sets $\{\sigma\lambda_\gamma, 1 \leq \gamma \leq N\}$ and $\{\sigma\lambda_\gamma + \sigma\mu g, 1 \leq \gamma \leq N\}$ intertwine on the unit circle. This restriction is the analog of (4.53), with the difference that (4.53) was a property of eigenvalues of a Hermitian matrix, while here the λ_α are defined on the unit circle.

Our RS random matrix ensemble is then defined as the set of matrices (4.64) with positions $\mathbf{q}$ and momenta $\mathbf{p}$ given by uniformly distributed random variables with $\mathbf{q} \in\in \tilde{\Omega}$ and $p_j \in [0, 2\pi/\sigma[$. The joint distribution of eigenvalues for this ensemble is then the uniform distribution over the set defined by the intertwining condition of the sets $\{\sigma\lambda_\gamma, 1 \leq \gamma \leq N\}$ and $\{\sigma\lambda_\gamma + \sigma\mu g, 1 \leq \gamma \leq N\}$. For instance for $\mu = 2\pi/N$, $\sigma = 1$ and $g = a$, this intertwining condition is equivalent (for sufficiently large N) to the condition that at a distance $2\pi a/N$ from any λ_α there exist exactly $[a]$ other eigenvalues (with $[a]$ the integer part of a). The joint distribution of eigenvalues is the uniform distribution over the set of λ_α such that any interval $]\lambda_\alpha, \lambda_\alpha + 2\pi a/N[$ contains exactly $[a]$ eigenvalues. All spectral correlation functions can be calculated analytically using a transfer operator approach [OG030]. Their expressions depend on the interval in which a lies. For $0 < a < 1$, the nearest-neighbour spacing distribution is a Poisson distribution shifted by a, namely

$$P(s) = \frac{1}{1-a} \mathrm{e}^{-(s-a)/(1-a)}, \ s > a, \quad P(s) = 0, \ s < a. \quad (4.70)$$

The generalized spacing distributions are given by similar expressions

$$P(n, s) = \frac{1}{(1-a)^n (n-1)!} \mathrm{e}^{-(s-na)/(1-a)}, \ s > na, \quad P(n, s) = 0, \ s < na. \quad (4.71)$$

These expressions are illustrated in Fig. 4.6. For $1 < a < 2$, we get explicit expressions

$$P(s) = A^2 \sinh^2(Bs), \quad s < a \quad (4.72)$$

for $1 < a < 4/3$, and

$$P(s) = A^2 \sin^2(Bs), \quad s < a \quad (4.73)$$

for $4/3 < a < 2$, with A and B obtained from normalization conditions. Analytic expressions for $a = 4/3$ are

$$P(s) = \frac{81}{64} s^2, \ 0 < s < a \quad (4.74)$$

for the nearest-neighbour spacing distribution,

$$P(2, s) = \left(-\frac{3}{2} + \frac{27}{16} s - \frac{81}{512} s^3 \right) \mathrm{e}^{3s/4-1}, \ \frac{4}{3} < s < \frac{8}{3} \quad (4.75)$$

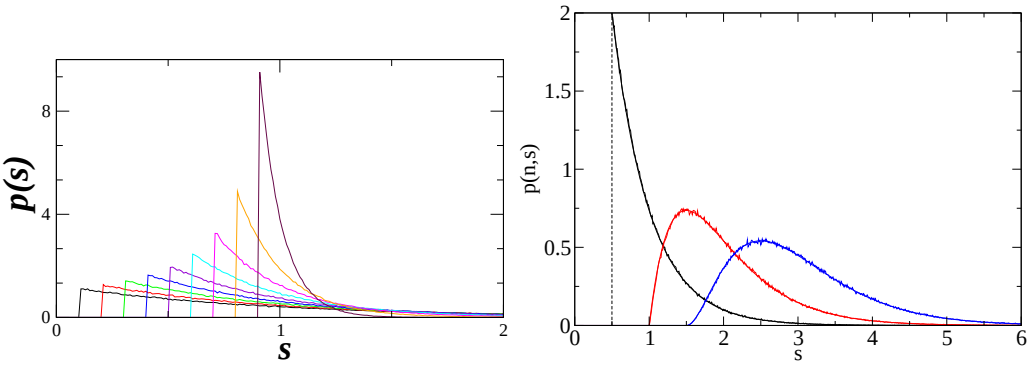

Figure 4.6: Left panel: $P(s)$ for $a = 0.1, 0.2, \ldots, 0.9$ and $N = 701$. Right panel: $P(n, s)$ for $a = 0.5$ and $n = 1, 2, 3$, $N = 701$.

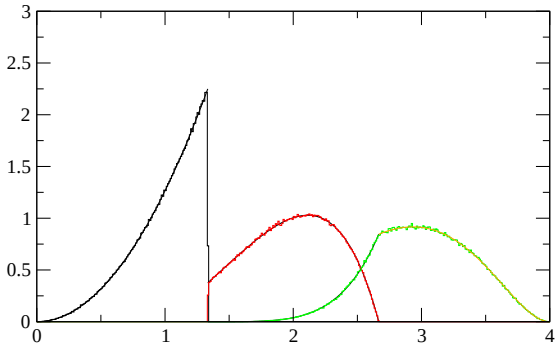

Figure 4.7: Distributions $P(n, s)$ for $a = 4/3$ and $n = 1, 2, 3$, $N = 701$.

and

$$P(3,s) = \begin{cases} \left(\frac{3}{4} - \frac{81}{32}s + \frac{81}{512}s^3\right) \mathrm{e}^{3s/4-1} + \frac{81}{64}s^2, & \frac{4}{3} < s < \frac{8}{3} \\ \left(-\frac{9}{4} + \frac{27}{32}s - \frac{81}{512}s^3\right) \mathrm{e}^{3s/4-1} + 9\mathrm{e}^{3s/2-4}, & \frac{8}{3} < s < 4 \end{cases} \tag{4.76}$$

for the smallest values of n. These expressions are illustrated in Fig. 4.7. The calculations get quite tedious for $2 < a < 3$, and the expressions obtained are complicated. We only present some numerical results in Fig. 4.8, together with the analytic expressions of [OG030].

The level compressibility for this model can be easily obtained from the expansion (3.14) of the Laplace transform of the two-point correlation function. For instance for $0 < a < 1$, since all $P(n, s)$ are known, (3.14) gives the explicit expression

$$g_2(t) = \frac{1}{\mathrm{e}^{at}(1 + t - at) - 1}, \tag{4.77}$$

from which one gets

$$\chi = (1 - a)^2. \tag{4.78}$$

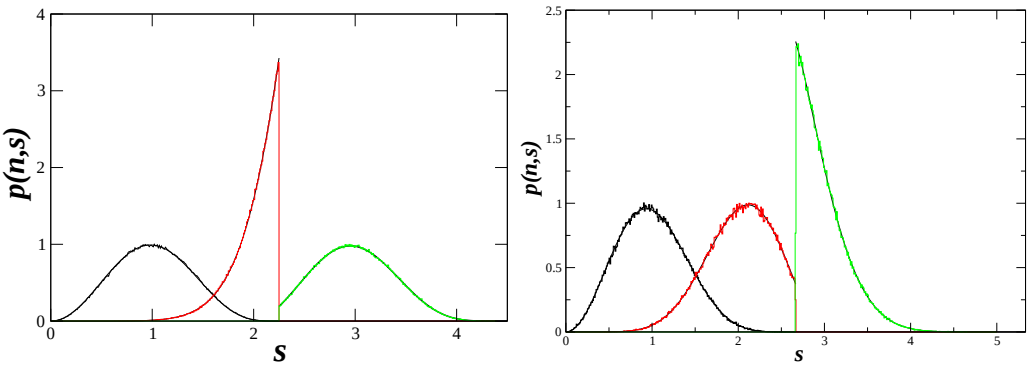

Figure 4.8: $P(n,s)$ for $a = 9/4$ (left) and $8/3$ (right).

For $a > 1$ expressions get more complicated. We nevertheless give them here as they will show up in Chapter 7. For $1 < a < 2$ we obtained

$$\chi = \left(\frac{a^2}{4} - \frac{4a(1-a)z^2 + a^2 \sinh^2 z}{(2z - \sinh 2z)^2} \sinh^2 z \right) \frac{\sinh^2 z}{z^2}, \tag{4.79}$$

where z is the solution of

$$a = \frac{2z^2 - z \sinh 2z}{z^2 + \sinh^2 z - z \sinh 2z}, \tag{4.80}$$

which is real when $1 < a < 4/3$ and imaginary when $4/3$. For $a = 4/3$ one has $\chi = 1/9$.

In the range $2 < a < 3$ we got

$$\chi = \frac{1}{a(\sin^2 z + z^2 - z \sin 2z)^2} \Big[(a-3)^2(a-2)z^2 - 6(a-2)z^2 \sin^2 z$$
$$-(a-3)(a-1)(2a-5)z^3 \sin 2z + 2(a-2)(\cos 2z + 2)(a-1)(a-2)z^2 \sin^2 z$$
$$-2a(a-2)(2a-3)z \cos z \sin^3 z + a(a-1)^2 \sin^4 z \Big] \tag{4.81}$$

where

$$x = \frac{a \sin^2 z + (a-2)z^2 + (1-a)z \sin 2z}{(a-1)\sin^2 z + (a-3)z^2 + (2-a)z \sin 2z} \tag{4.82}$$

and

$$\frac{e^x}{x} = \frac{\sin z}{z} e^{z/\tan z}. \tag{4.83}$$

These expressions are illustrated in Fig. 4.9 for numerically diagonalized matrices with $q_j = j$, $j = 1, \ldots N$ and p_j random variables uniformly distributed in $[0, 2\pi]$.

4.4.6 Analogy between RS and the intermediate map

For the particular choice of parameters $\mu = 2\pi/N$ and $\sigma = 1$, and when $q_j = j$, $j = 1, \ldots N$, Eq. (4.65) reduces to

$$\tilde{V}_k(z) = \frac{\sin(\pi g/N)}{N \sin \pi g}. \tag{4.84}$$

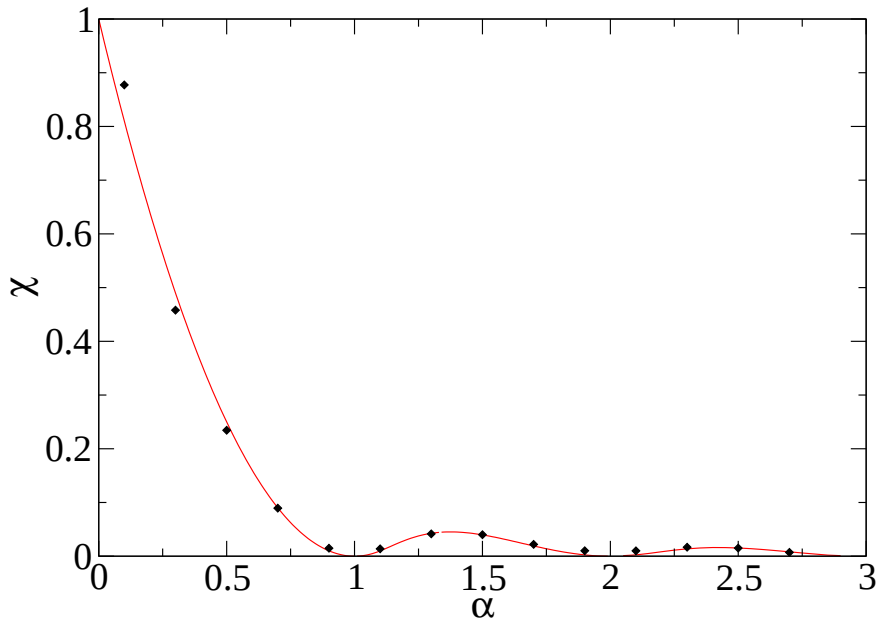

Figure 4.9: Level compressibility χ. Black diamonds are the numerical values extracted from a cubic fit of $\Sigma^2(L)$ over the range $L \in [0, 80]$, with $\Sigma^2(L)$ the variance of the number of levels in an interval of length L averaged over 50 windows of length L, calculated from the unfolded spectrum with mean level spacing $\Delta = 1$, for 10000 realisations of the random matrix with matrix size $N = 256$. Red curve is the theoretical prediction (4.78), (4.79) and (4.81).

Choosing p_j as independent random phases Φ_j uniformly distributed between 0 and 2π, the Lax matrix, Eq. (4.64), can then be rewritten, up to a simple phase change,

$$L_{jk} = \frac{e^{i\Phi_j}}{N} \frac{1 - e^{2i\pi g}}{1 - e^{2i\pi(j-k+g)/N}}. \tag{4.85}$$

Remarkably, this matrix is very similar to the intermediate map (4.26). Namely, it exactly coincides with (4.26) provided the constant g is chosen to be N-dependent, as $g = N\gamma$.

The intermediate map can be interpreted as the unfolded version of the Ruijsenaars-Schneider map (4.64). Indeed, recall from the discussion in 4.1.3 that quantum dynamics of a kicked map takes place on a cylinder that has to be truncated. Any choice of N and $\hbar$ (or of the integer k such that $\hbar = 2k\pi/N$) defines a certain truncation of the cylinder. The quantum system does not feel what happens at a scale smaller than $\hbar$. There are two extreme situations (for simplicity let us consider the case N even):

1. One chooses $k = 1$, that is, $\hbar = 2\pi/N$. This amounts to truncate the cylinder at $p = 2\pi$ (one classical cell). The phase space has thus the structure of a torus $[0, 2\pi[^2$;

2. One chooses $k = N$, that is, $\hbar = 2\pi$, so that the quantum scale $\hbar$ encompasses a whole classical cell. This amounts to look at the quantum system while blurring structures at the scale of a classical cell. The truncation of the cylinder takes place at $p = 2\pi N$, which depends on N.

The classical intermediate map (4.23) is defined on a torus $[0,1[^2$ rather than $[0,2\pi[^2$. In order to make the connection between (4.23) and the kicked maps (4.6) on the torus $[0,2\pi[^2$, one first reintroduces a mass $\mu = 1/2$ in the Hamiltonian (4.5), so that the kinetic term becomes $p^2/(2\mu)$. For a potential $V(q) = -4\pi^2\gamma\{\frac{q}{2\pi}\}$, the classical map (4.6) becomes

$$\begin{aligned} \bar{p} &= p + 2\pi\gamma \qquad (\mathrm{mod}\, 2\pi) \\ \bar{q} &= p + 2\bar{p} \qquad (\mathrm{mod}\, 2\pi), \end{aligned} \tag{4.86}$$

where the factor 2 in front of $\bar{p}$ comes from $1/\mu = 2$. The corresponding kinetic operator is $\exp(-ip^2/(2\mu\hbar))$, and the above periodicity argument implies that for a given N we should choose a truncation at a multiple of $\hbar = \pi/N$ (N even) or $\hbar = 2\pi/N$ (N odd). If we choose to take $\hbar = 2\pi/N$ (whether N be even or odd), then using $p = P\hbar$ and $q = 2\pi Q/N$ we get that $\hat{U}$ is the product of two operators with diagonal elements given by $\exp(-ip^2/(2\mu\hbar)) = \exp(-2i\pi P^2/N)$ and $\exp(-iV(q)/\hbar) = \exp(2i\pi\gamma Q)$ respectively. This exactly coincides with the quantum operator considered in [OG006] and given by Eq. (4.24) in momentum representation. On the other hand, for the choice $\hbar = 2\pi$, and with μ (or the period of the kick) taken as an irrational number (so that the kinetic term can be replaced by a random phase) we get the Ruijsenaars map (4.85).

Therefore the intermediate map and the Ruijsenaars map correspond to the same quantum kicked dynamics; only the scale ($\hbar = 2\pi/N$ or $\hbar = 2\pi$) at which the underlying classical structure is taken into account differs. This explains why the Ruijsenaars map is insensitive to the rational or irrational nature of its parameter, while the intermediate map is: the former does not see the classical structure below the scale of the torus, but feels the discontinuity of the potential, which is at the scale of a classical cell.

Chapter 5

Quantum multifractality

While the two previous chapters were concerned with statistical properties of spectra, we now move on to eigenvector properties. Here we give an introduction to quantum multifractality and present some results for simple models.

5.1 Definition and properties

5.1.1 Some mathematical definitions

There are several mathematical definitions of multifractal dimensions, which all satisfy the criteria one might intuitively expect from such a notion: monotonicity, value for d–dimensional submanifolds or for countable sets, etc. We only briefly mention the main ones.

Let $\Omega \subset \mathbb{R}^n$. The Hausdorff dimension [161] characterizes the small-ϵ behaviour of the moments

$$Z_{q,\epsilon} = \sum_i \mu(B_i(\epsilon))^q, \tag{5.1}$$

where $\{B_i(\epsilon)\}$ is an ϵ–cover of Ω, i.e. a countable ensemble of open subsets of $\mathbb{R}^n$ such that $\Omega \subset \bigcup_i B_\epsilon$ and the diameter of each $B_i(\epsilon)$ is $\mu(B_i(\epsilon)) < \epsilon$. The Hausdorff measure of Ω with parameter q is the limit for $\epsilon \to 0$ of the inf of $Z_{q,\epsilon}$ over all covers. The Hausdorff dimension is the critical value of q at which the Hausdorff measure becomes equal to 0.

The box-counting dimension D_{bc} corresponds to taking $\mu(B_i(\epsilon)) = \epsilon$. It characterizes the small-ϵ behaviour of the smallest number of sets of size ϵ necessary to cover of Ω. If N_ϵ is this number, then the box-counting dimension is $-\lim_{\epsilon\to 0}(\ln N_\epsilon)/(\ln \epsilon)$, that is, $N_\epsilon \sim \epsilon^{-D_{bc}}$.

The packing dimension characterizes the small-ϵ behaviour of the largest number of disjoint balls of size less than ϵ with their centers within Ω.

We refer to the book by Falconer [42] for more detail on these mathematical definitions.

5.1.2 Physical definitions

Physicists obviously have to deal with finite systems (finite time, finite measurements, discrete nature of computer implementations), so that they have to adapt these definitions of fractals. The Hausdorff dimension is favored by mathematiciens because of its nice analytical properties. Physicists tend to prefer the box-counting dimension, which can be extracted by extrapolation from a finite range of diameters ϵ. A different approach favored by physicists is to fix ϵ and let the system size go to infinity, thus considering moments of the wavefunction.

For a wavefunction ψ defined on a d-dimensional lattice of linear size L and lattice spacing a (thus with $N = (L/a)^d$ sites), multifractal dimensions are defined via the scaling of the inverse participation ratios (IPR)

$$P_q = \int d^d r |\psi(\mathbf{r})|^{2q} \tag{5.2}$$

when L/a goes to infinity. For disordered systems, the average IPR behaves as

$$\langle P_q \rangle \propto \left(\frac{L}{a}\right)^{-\tau_q}, \qquad \tau_q = D_q(q-1), \tag{5.3}$$

for real q. This relation can be reexpressed as

$$\langle |\psi(\mathbf{r})|^{2q} \rangle \propto \left(\frac{L}{a}\right)^{-\Delta_q - qd}, \tag{5.4}$$

where the average now also runs over lattice sites, and we have introduced the anomalous dimensions

$$\Delta_q = \tau_q - d(q-1), \tag{5.5}$$

which characterize the departure from a uniform state (for a uniform state with constant entries one has $\Delta_q = 0$). This scaling translates onto the LDOS $\rho(E, \mathbf{r}) = \sum_n \delta(E - E_n)|\psi(\mathbf{r})|^2$ as

$$\langle \rho(E, \mathbf{r})^q \rangle \propto L^{-\Delta_q}. \tag{5.6}$$

There are similar expressions for the asymptotic behaviour of n–point correlation functions: for instance the two-point function behaves as [162, 163]

$$\langle |\psi(\mathbf{r})|^{2q} |\psi(\mathbf{r}')|^{2s} \rangle \propto \left(\frac{|\mathbf{r} - \mathbf{r}'|}{a}\right)^{-z_{q,s}} \left(\frac{L}{a}\right)^{y_{q,s}}. \tag{5.7}$$

If we make the further assumption that intensities are uncorrelated at scale L, that is,

$$\langle |\psi(\mathbf{r})|^{2q} |\psi(\mathbf{r}')|^{2s} \rangle \sim \langle |\psi(\mathbf{r})|^{2q} \rangle \langle |\psi(\mathbf{r}')|^{2s} \rangle, \qquad |\mathbf{r} - \mathbf{r}'| \sim L, \tag{5.8}$$

and that they do not vary much over the scale a, i.e.

$$\langle |\psi(\mathbf{r})|^{2q} |\psi(\mathbf{r}')|^{2s} \rangle \sim \langle |\psi(\mathbf{r})|^{2(q+s)} \rangle \qquad |\mathbf{r} - \mathbf{r}'| \sim a, \tag{5.9}$$

then using (5.4) one directly gets

$$y_{q,s} = -\Delta_{q+s} - d(q+s), \qquad z_{q,s} = \Delta_q + \Delta_s - \Delta_{q+s}, \tag{5.10}$$

so that the set of exponents Δ_q, or equivalently τ_q or D_q, entirely characterize correlations (5.7) of the multifractal pattern. In particular D_2 plays an important role, as it governs the correlation function of eigenfunction intensities according to the relation

$$\langle |\psi(\mathbf{r})|^2 |\psi(\mathbf{r}')|^2 \rangle \propto \left(\frac{|\mathbf{r}-\mathbf{r}'|}{L} \right)^{D_2-d} \left(\frac{a}{L} \right)^{2d}. \tag{5.11}$$

Similarly, the overlap between functions at different energies is expected to follow the behaviour

$$\left\langle \sum_{|E_i-E_j|=\omega} |\psi^{(i)}(\mathbf{r})|^2 |\psi^{(j)}(\mathbf{r})|^2 \right\rangle \sim \omega^{-\mu}, \qquad \mu = 1 - D_2/d \tag{5.12}$$

for $\omega \gg \Delta$ [9, 164, 165]. This means that only eigenfunctions corresponding to energy levels not too far from each other have a significant overlap and can interact. This translates to a level repulsion at small argument for the nearest-neighbour energy spacing [165]. The relation (5.12) between μ and the fractal dimension D_2 has been observed numerically for integer quantum Hall systems, the 3D Anderson model [166] or the PRBM model [167]. It has been shown analytically to hold in the strong multifractality limit by calculating the perturbative expansion of the exponents D_2 and μ up to second order in the band parameter $g \ll 1$ via the supersymmetric virial expansion technique [168, 169] (see Section 8.2.2).

Note that, since multifractality can be seen as a scaling property of local averages of a certain measure, some remaining multifractal features may be observed at certain scales in the vicinity of a critical point. For instance, close to Anderson transition on the insulating side, there is still multifractality at box sizes small compared to the localization length [167].

While the above definitions are related to scaling properties of eigenfunctions in the whole sample, for a finite system such properties may differ in the vicinity of boundaries. Surface multifractal exponents were introduced in [170] to describe scaling properties at boundaries, and investigated in [171] for the PRBM model, showing specific features.

We now specialize to the one-dimensional case, which will be our main point of interest.

5.1.3 One-dimensional multifractal dimensions

In the case of a one-dimensional wavefunction on a Hilbert space of finite dimension N, one has $d = 1$ and $L/a = N$, while ψ is specified by its components ψ_n, $1 \leq n \leq N$. The moments, or inverse participation ratios, of the wavefunction, are then defined by

$$Z_q = \sum_{k=1}^{N} |\psi_k|^{2q} \tag{5.13}$$

The exponent τ_q characterizes the large–N behaviour of Z_q, namely

$$\langle Z_q \rangle \propto_{N\to\infty} N^{-\tau_q}. \tag{5.14}$$

Multifractal dimensions D_q are then given from (5.3) by

$$D_q = \frac{\tau_q}{q-1}. \tag{5.15}$$

Note that from the definition given above the multifractal dimensions depend on the basis in which the vector $|\psi\rangle$ is expressed.

Let us now point out some elementary facts. For $q = 1$, normalization of the measure or the wavefunction implies that $Z_q = 1$, and thus $\tau_1 = 0$. In the limit $q \to 1$, the undefined form (5.15) gives the information dimension D_1, defined by

$$-\langle \sum_{k=1}^{N} |\psi_k|^2 \ln |\psi_k|^2 \rangle \underset{N\to\infty}{\sim} D_1 \ln N, \tag{5.16}$$

which corresponds to the Shannon entropy of the $|\psi_j|^2$. A commonly used measure of localization is given by the inverse participation ratio

$$\xi = \frac{1}{\sum_{k=1}^{N} |\psi_k|^4}, \tag{5.17}$$

which is often used in the mesoscopic physics literature to measure the localization length (a state uniformly spread on exactly M basis vectors is such that $\xi = M$).

Let $E_k = -\ln |\psi_k|^2$. Since the vector ψ is normalized to 1, the E_k are positive. The moments Z_q can then be rewritten as

$$Z_q = \sum_{k=1}^{N} e^{-qE_k}, \tag{5.18}$$

which can be seen as a partition function at inverse temperature q. Simple algebra then yields

$$-\frac{\partial}{\partial q} \ln Z_q = \frac{\sum_{k=1}^{N} E_k e^{-qE_k}}{\sum_{k=1}^{N} e^{-qE_k}} = \langle E_k \rangle \tag{5.19}$$

and

$$\frac{\partial^2}{\partial q} \ln Z_q = \langle E_k^2 \rangle - \langle E_k \rangle^2, \tag{5.20}$$

which are both positive quantities. If $\tau_q^{(N)}$ is defined as

$$\tau_q^{(N)} = -\frac{\ln Z_q}{\ln N} \tag{5.21}$$

so that τ_q corresponds to the large–N limit of $\tau_q^{(N)}$, then from (5.19)–(5.20) one has $\tau_q' \geq 0$ and $\tau_q'' \leq 0$. That is, the function τ_q is an increasing function of q and is concave.

The tangent to the curve $q \mapsto \tau_q$ at point q is given by the equation

$$y = \tau_q + (x - q)\tau_q'. \tag{5.22}$$

In particular, taking $x = 1$, we have that the tangent to the curve at point q goes through the point of coordinates $(1, \tau_q + (1-q)\tau'_q)$. Concavity of τ_q implies that the curve is always below its tangent, and since $\tau_1 = 0$, one has the inequality

$$\tau_q + (1-q)\tau'_q \geq 0. \tag{5.23}$$

From the definition (5.15) of D_q, we get that its derivative with respect to q reads

$$D'_q = \frac{-\tau_q + (q-1)\tau'_q}{(q-1)^2} \leq 0 \tag{5.24}$$

according to (5.23). This shows that D_q is always a decreasing function of q. At $q \to \pm\infty$ only the extreme values of $|\psi_k|^2$ survive in the sum (5.13), so that $D_{\pm\infty}$ characterize the asymptotic behaviour of extremes.

Exponents can also be defined for wavefunction correlations, following Eq. (5.7): multifractals are characterized by a power-law correlation of intensities

$$\langle |\psi_i|^{2q} |\psi_j|^{2s} \rangle \sim N^{y_{q,s}} |i-j|^{-z_{q,s}}, \quad q, s \geq 0, \quad 1 \ll |i-j| \ll N. \tag{5.25}$$

5.1.4 Singularity spectrum $f(\alpha)$

The singularity spectrum characterizes the fractal dimensions of sets of points having the same singularity strength. It was introduced in [172] and [173]. Mathematically, sets of points with Hölder exponent α have a Hausdorff dimension given by a quantity $f(\alpha)$ which depends on α [42]. This dependence justifies the term of "multifractal". In the discrete case we are considering here, the number of values of i such that $|\psi_i|^2 \sim N^{-\alpha}$ scales as $N^{f(\alpha)}$. More specifically, the multifractal Ansatz expresses the density of exponents α as

$$\rho(\alpha) = \sum_{i=1}^{N} \delta\left(\frac{\ln |\psi_i|^2}{\ln N} + \alpha \right) \propto N^{f(\alpha)}. \tag{5.26}$$

As emphasized in [42], $f(\alpha)$ is related to, but different from the multifractal dimension of the set of i such that $|\psi_i|^2 \sim N^{-\alpha}$; indeed, that set is defined by the behaviour of the function around point i as a function of the system size N (or the box size $1/N$), and therefore the set itself changes when the system (or box) size varies.

From its definition, the singularity spectrum can be related to the multifractal exponents: from (5.13) and (5.26) one gets

$$Z_q = \int_0^\infty d\alpha N^{-\alpha q} \rho(\alpha) \propto \int_0^\infty d\alpha N^{-\alpha q + f(\alpha)}. \tag{5.27}$$

Evaluating this integral by the Laplace method in the limit $\ln N \gg 1$, one obtains the multifractal exponent τ_q defined by Eq. (5.14) as the Legendre transform of $f(\alpha)$, namely

$$\tau_q = \min_\alpha (\alpha q - f(\alpha)). \tag{5.28}$$

Conversely, the singularity spectrum is related to τ_q via

$$f(\alpha) = \min_q(q\alpha - \tau_q). \tag{5.29}$$

For each q, we denote α_q the value of α which achieves the minimum in (5.28) (and depending on the situation we may drop the index q). From (5.29) we have

$$\alpha_q = \tau_q' \tag{5.30}$$

(that is, the derivative of τ_q with respect to q). In particular we have $\alpha_1 = D_1$ and $\alpha_0 = d - D_0'$. In a symmetric way, one has

$$q(\alpha) = f'(\alpha), \tag{5.31}$$

so that the slope of the singularity spectrum gives the corresponding value of q. The equation of the slope is $y - f(\alpha) = f'(\alpha)(x - \alpha)$, which using (5.29) and (5.31) is equivalent to $y = -\tau_q + xq$ (with here $q \equiv q(\alpha)$). Thus τ_q appears as the distance to the origin of the intersection point of the tangent of slope q.

The singularity spectrum for a multifractal is a concave function which usually looks like a parabola pointing downwards (see e.g. Fig. 5.1). Its maximum is reached at $\alpha = \alpha_0 \geq d$, where $f(\alpha_0) = d$. Inequality (5.23) is equivalent to

$$f(\alpha) \leq \alpha. \tag{5.32}$$

From (5.28) and since $\tau_1 = 0$, one has that $\min_\alpha(\alpha - f(\alpha)) = 0$ and is reached for $\alpha = \alpha_1$, which implies that the line $f(\alpha) = \alpha$ is tangent to the curve for $f(\alpha)$ at $\alpha = \alpha_1$.

The quantity $q\alpha - \tau_q$ in (5.29) has no minimum outside an interval $[\alpha_+, \alpha_-]$. These two values $\alpha_\pm$ of the singularity exponents define the support of the singularity spectrum. From the relation (5.30) we get that there exists an interval $[q_-, q_+]$ outside of which the exponents τ_q are given by the linear relation $\tau_q = q\alpha_+$ for $q > q_+$ and $\tau_q = q\alpha_-$ for $q < q_-$.

5.1.5 Annealed vs typical averaging

Most of the models investigated in the present work describe disordered systems, and therefore relevant quantities should be computed after ensemble averaging. Multifractal dimensions will depend on the shape of the distribution of moments Z_q (see next section) and on the way in which the average is performed. One distinguishes the annealed average $\langle Z_q \rangle$, which may be dominated by the contribution of rare wavefunctions with much larger moments, and the typical average $Z_q^{\rm typ} = \exp\langle \ln Z_q \rangle$, which corresponds to the typical value of the moments. One can therefore define two sets of multifractal exponents, corresponding to the asymptotic behaviour of these two different averages, namely

$$\langle Z_q \rangle \propto N^{-\tau_q},\ \tau_q = D_q(q-1), \tag{5.33}$$

$$Z_q^{\rm typ} \propto N^{-\tau_q^{\rm typ}},\ \tau_q^{\rm typ} = D_q^{\rm typ}(q-1). \tag{5.34}$$

Historically the discrepancy between annealed and typical (quenched) averaging in the context of multifractality was seen in the context of the Anderson transition [137, 21] and was very recently confirmed by the analytical calculations of [24, 174] in the same model.

Similarly as for the multifractal exponents, one can define an annealed singularity spectrum $f(\alpha)$ and a typical singularity spectrum $f^{\rm typ}(\alpha)$ [21, 175]. While the typical singularity spectrum is always positive, the annealed one can take negative values. The singularity strengths α such that $f(\alpha) < 0$ correspond to singularities that occur in average less than once in a given vector, so that the number of points having this singularity decreases with N (numerically it is therefore necessary to have much more random realizations of a system when N increases in order to capture correctly rare events). The terminating points of $f^{\rm typ}(\alpha)$ correspond to $q \to q_\pm$, which according to (5.31) are given by the slope of the singularity spectrum at the x-axis. The left terminating point of the annealed spectrum $f(\alpha)$ corresponds to $\alpha = 0$, and may take a finite value (e.g. for the REM (5.42)). Figure 5.3 illustrates these features for the random energy model defined in section 5.2.2 and the Spohn-Derrida model of section 5.2.3.

The multifractal exponents described in Section 5.1.4 correspond to the typical ones, as they are defined for a single realization. In particular, the interval $[\alpha_+, \alpha_-]$ corresponds to the support of the singularity spectrum $f^{\rm typ}(\alpha)$. One has $\tau_q^{\rm typ} = q\alpha_+$ for $q > q_+$ and $\tau_q^{\rm typ} = q\alpha_-$ for $q < q_-$, so that as $q \to \infty$ one has $D_q^{\rm typ} \to \alpha_+$. In the same limit, the $f(\alpha)$ plot goes down to $\alpha \to 0$. From Eq. (5.30), this implies that τ_q has a horizontal asymptote, and thus that $D_q \to_{q\to\infty} 0$. The two singularity spectra are expected to coincide over the interval $[\alpha_+, \alpha_-]$. However, analytic formulas for typical and average multifractal exponents obtained for the Anderson model by perturbation expansion showed that $f(\alpha)$ and $f^{\rm typ}(\alpha)$ differ even in the region $f(\alpha) > 0$ [174]. These properties depend on the tails of the moment distribution, which we now discuss.

5.1.6 Moment distribution

Obviously, the generalized IPRs $Z_q = \sum_i |\psi_i|^{2q}$ defined in (5.13) are only the moments of the distribution of eigenvalue intensities $|\psi_i|^2$. In order to go beyond the average values of moments, one can consider the whole distribution itself, or, equivalently, the distribution $P(x)$ of the rescaled variable $x = N|\psi_i|^2$. This distribution can be related to the singularity spectrum by

$$P(x) \propto \frac{1}{Nx} e^{f(\alpha)\ln N}, \tag{5.35}$$

where α is related to x via $|\psi_i|^2 = N^{-\alpha}$, i.e. $x = N^{1-\alpha}$. In other words, $f(\alpha)$ is (up to some linear shift) the large deviation function of the distribution of $\ln|\psi_i|^2$.

For mesoscopic metallic samples that can be described by a nonlinear σ-model, analytic expressions were obtained for the distribution of eigenfunction amplitudes [176, 177]). The leading term coincides with the Porter-Thomas distribution (3.45) of RMT (accordingly, spectral statistics correspond to RMT ones).

The moments Z_q themselves have a certain distribution, which was investigated for instance in weakly disordered metallic grains at finite conductivity g [178]. It

was conjectured that at large system size, the moments

$$y_q = \frac{Z_q}{Z_q^{\rm typ}}, \tag{5.36}$$

normalized by their typical value, should have a limiting distribution. This was checked e.g. in [136] for the periodic PRBM (4.12), where the distribution of y_2 was shown to be scale-invariant, or in [179] for the PRBM (4.11). Since for large N one has $Z_q^{\rm typ} \propto D_2^{\rm typ} \ln N$, the distribution of $\ln Z_2$ is the distribution $P(y_2)$ shifted by $D_2^{\rm typ} \ln N$. Note that in [179] the distribution of correlation dimension D_2 for PRBM was also investigated, showing that at $N \to \infty$ it gets peaked at a fixed value which coincides with the value obtained from the scaling of $Z_q^{\rm typ}$. A similar approach was used in the case of the 3D Anderson model in [180].

It was suggested [136, 137] that the distribution of the normalized moments y_q at criticality has a power-law tail

$$\mathcal{P}(y_q) \sim \frac{1}{y_q^{1+x_q}}. \tag{5.37}$$

for large y_q. When $x_q > 1$ the two multifractal exponents τ_q and $\tau_q^{\rm typ}$ coincide. When the moment distribution has a heavy tail ($x_q < 1$), the averages $\langle Z_q \rangle$ and $\exp\langle \ln Z_q \rangle$ yield different exponents, since the former depends on the cut-off chosen to perform the average. The exponents τ_q and $\tau_q^{\rm typ}$ thus only coincide over the interval $[q_-, q_+]$ where $x_q > 1$, the points $q = q_\pm$ being characterized by an exponent $x_q = 1$.

Other properties were proposed for the exponents x_q. In Chapter 7 we will illustrate them for the Anderson map and the intermediate map.

5.2 A few simple examples

We are currently investigating various properties of simple models such as REM and Spohn-Derrida models defined below, in particular extreme value statistics, and the connections between these models and our quantum maps and random matrix ensembles (see [OG042]). As an illustration of the way multifractal spectra look like, we present here a few of the numerical results obtained in this context.

5.2.1 The multiplicative cascade

Multiplicative cascades are the simplest examples of a multifractal measure. They were originally suggested as a useful model of turbulent velocity field [181, 182], and shown to display multifractal properties [182]. Random multiplicative cascades were studied in more detail by Kahane [183, 184, 185].

A deterministic multiplicative cascade is obtained by dividing the interval $[0, 1]$ into two segments of equal length and assigning a weight p to the left half and $1 - p$ to the right half. Recursively iterating this process on each half yields a measure on the interval $[0, 1]$ after n steps. This measure is such that the interval $I_{b_1 \ldots b_n}$ defined as $[\sum_i b_i 2^{-i}, \sum_i b_i 2^{-i} + 2^{-n}]$, with $b_1 \ldots b_n$ a binary string, has measure $\mu(I_{b_1 \ldots b_n}) = p^k (1-p)^{n-k}$, where k is the number of zeros in the string $b_1 \ldots b_n$. It is easy to derive

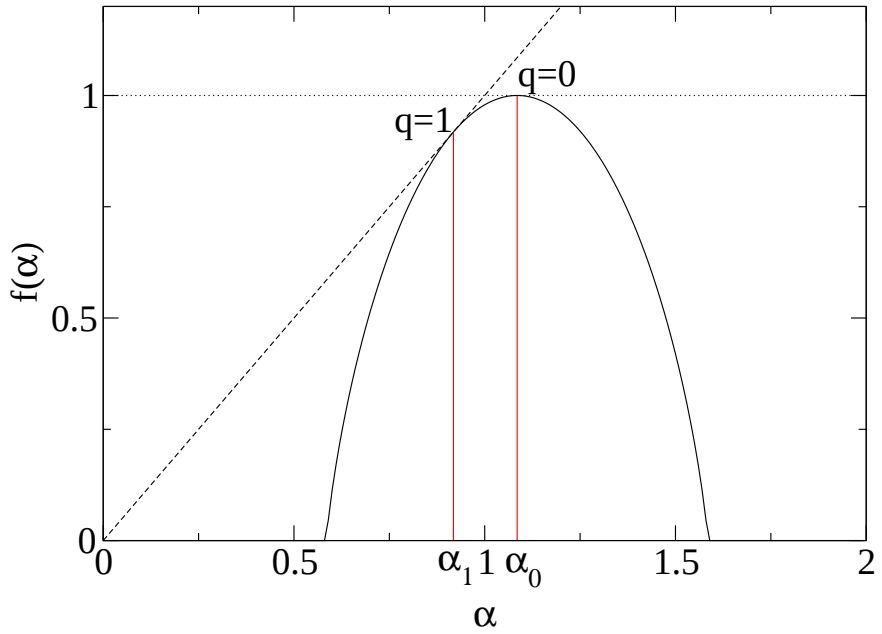

Figure 5.1: Singularity spectrum $f(\alpha)$ for the deterministic multiplicative cascade with $p = 1/3$ (solid black). Dashed line is $f(\alpha) = \alpha$, red vertical lines have abscissas $\alpha_0 \simeq 1.085$ and $\alpha_1 \simeq 0.918$ obtained from (5.38).

exact expressions for the multifractal exponents τ_q, generalized dimensions D_q and singularity spectrum $f(\alpha)$ [186, 187]. For instance, the multifractal exponents read

$$\tau_q = -\log_2 \left(p^q + (1-p)^q\right) \tag{5.38}$$

However this simple example does not allow to study more subtle effects that arise when averages over ensembles of multifractal distributions are considered, as explained in Section 5.1.5. It is therefore suitable to consider a stochastic version of the multiplicative cascade. Such a stochastic multiplicative cascade can be obtained [188] by replacing p by a random variable X, so that k independent random variables $X_1, \ldots, X_k$ are drawn at step k and $\mu(I_{b_1 \ldots b_n}) = \prod_i X_i^{1-b_i}(1-X_i)^{b_i}$. An analytic expression can be derived for the fractal dimensions and the function τ_q. In the stochastic case, it reads

$$\tau_q = -\log_2 \int_0^\infty \left((2^{-t})^q + (1-2^{-t}))^q\right) 2^{-t} \ln 2 \rho(2^{-t}) dt, \tag{5.39}$$

with $\rho(t)$ the probability density function of the random variable X.

5.2.2 Random energy model (REM)

A slightly more elaborate model is the Random energy model introduced by Derrida [189]. It is defined by

$$p_i = \frac{1}{Z(\beta)} e^{\beta V_i} \qquad Z(\beta) = \sum_{i=1}^{N} e^{\beta V_i} \tag{5.40}$$

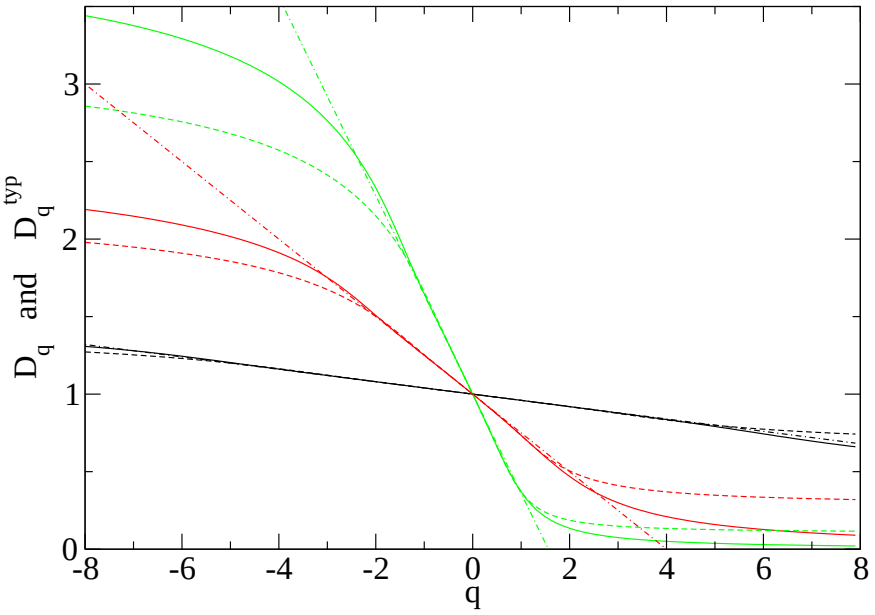

Figure 5.2: Multifractal dimensions D_q (solid) and $D_q^{\rm typ}$ (dashed) for the REM with $\beta = 0.2$ (black), 0.5 (red) and 0.8 (green), obtained by fitting over vector sizes $N = 2^7$ to 2^{12} and averaging over 2^{12} realizations. The dashed-dotted straight line corresponds to the analytic expression (5.41).

where V_i are i.i.d. Gaussian variables with $\langle V_i \rangle = 0$ and $\langle V_i^2 \rangle = 2 \ln N$. It can be shown that for $|\beta| < 1$ multifractal exponents are given by

$$\tau_q^{\rm typ} = q(1+\beta^2) - q^2\beta^2 - 1 \tag{5.41}$$

for $|q| < 1/\beta$, and $\tau_q^{\rm typ} = q\alpha_+$ for $q > 1/\beta$, $\tau_q^{\rm typ} = q\alpha_-$ for $q < -1/\beta$, with $\alpha_\pm = (1 \mp \beta)^2$. The singularity spectrum is then given by

$$f^{\rm typ}(\alpha) = 1 - \frac{1}{4\beta^2}(1+\beta^2-\alpha)^2 \tag{5.42}$$

for $\alpha \in [(1-\beta)^2, (1+\beta)^2]$ and zero outside this interval. These formulas are illustrated in Figs. 5.2 and 5.3 left. When the parameter β is larger than 1 a freezing phenomenon occurs, that is, the exponent $\tau_q^{\rm typ}$ vanishes for $q > 1$, which indicates localization on a number of sites independent on N. Using a replica trick, it is also possible to get analytic expressions for the annealed exponents [175]: for $|\beta| < 1$ one has the same expression as in (5.42), but over the range $0 \le \alpha \le 1 + \beta^2$.

5.2.3 Spohn-Derrida model

In this model the weights p_i are still of the form (5.40), but with V_i obtained as a sum of independent Gaussian random variables. Namely, we consider a binary tree with $N = 2^n$ leaves, and attribute to each edge a centered Gaussian random variable

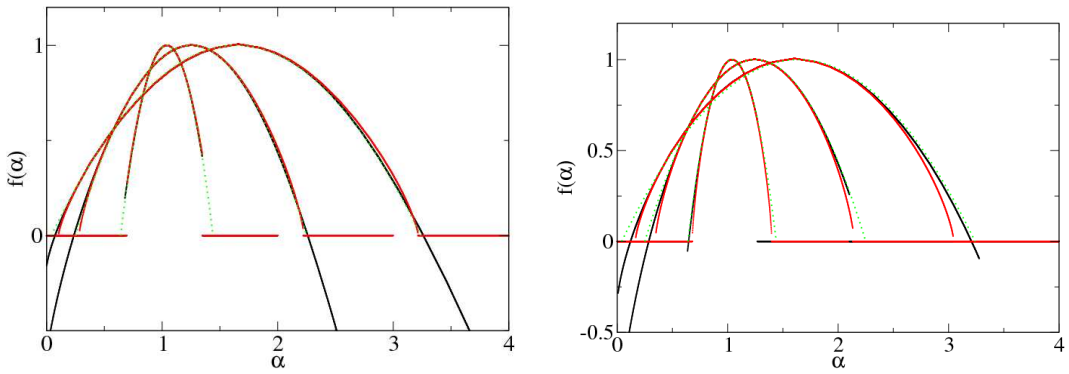

Figure 5.3: Singularity spectrum $f(\alpha)$ (black) and $f^{\rm typ}(\alpha)$ (red) for the REM (left) and Spohn-Derrida model (right), from narrowest to widest $\beta = 0.2, 0.5, 0.8$. The dotted green curve corresponds to the analytic expressions. Here $f(\alpha)$ is extracted from τ_q calculated over the range $q \in [-12, 12]$.

with variance $\frac{2n}{n+1} \ln 2$. Then V_i is the sum of all $n+1$ variables along the path going from the root to leaf i of the tree. As a sum of independent Gaussian variables, they are Gaussians with variance $2n \ln 2 = 2 \ln N$, and the singularity spectrum is still given by (5.42). This is checked in Fig. 5.3 (right panel).

5.3 Numerical methods

In [OG027] we compared various methods for the computation of multifractal dimensions. Here I briefly review the methods used.

5.3.1 Moment method

The simplest way of extracting multifractal exponents is to directly compute the asymptotic scaling of moments (5.13) with system size: the exponents τ_q are given by the slope of $\ln\langle Z_q \rangle$ as a function of $\ln N$. For numerical purposes, it is necessary to average locally the wavefunction over neighbouring sites since vanishing components of the wavefunction can lead to a diverging moment. In order to get more precise results, a fit of the form $a + D_q \ln N + b/N$ allows to take into account lowest-order corrections. Alternatively one can compute $\langle 1/Z_q \rangle$ to avoid instabilities due to very small values of the wavefunction. Coarse-graining of wavefunction components allows to correctly estimate the scaling behaviour for negative moments $q < 0$ [190].

In some cases, some care should be taken in the choice of matrix sizes. As an illustration (see [OG014]), we computed the dimension D_2 for eigenvectors of the intermediate map (4.26). As explained in 4.3, spectral statistics for this model depend on the map parameter, and more precisely, for rational $\gamma = a/b$, on the remainder of aN modulo b. The mean value of the IPR (5.17) is expected to scale as N^{D_2}, so that the dimension D_2 is given by the asymptotic value of $(\ln\langle \xi \rangle)/\ln N$. However in practice, for finite N there is an additional constant term which turns

out to depend, as the spectral statistics, on arithmetic properties of N. If sizes are chosen in such a way that $aN \bmod b$ is constant, then $\ln\langle\xi\rangle$ is indeed a linear function of $\ln N$ and the slope only depends on the denominator b (see Fig. 5.4).

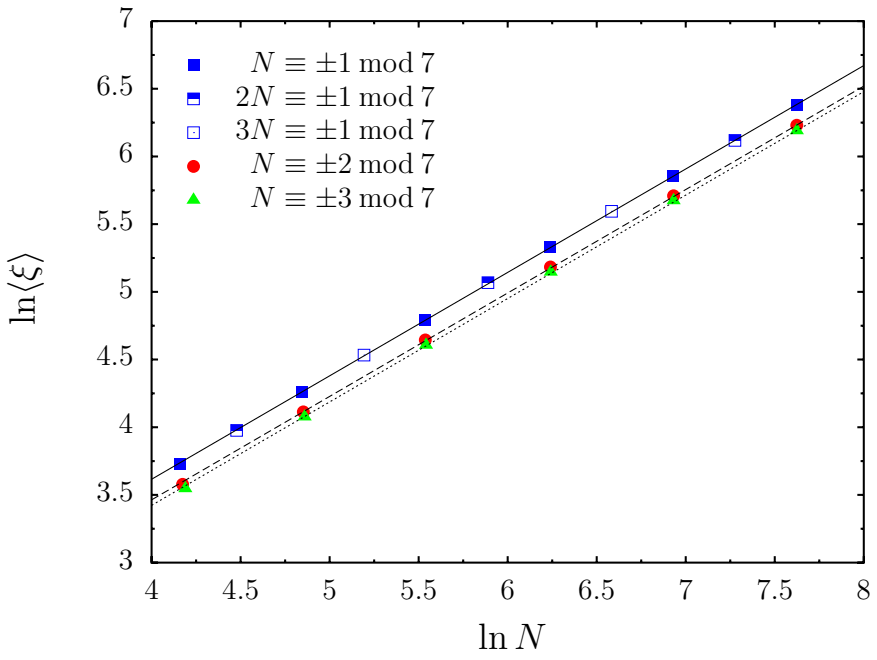

Figure 5.4: Mean IPR of eigenvectors of (4.26) as a function of the vector size N for $\gamma = 1/7$ (filled symbols), 2/7 (half-filled squares), 3/7 (empty squares). Straight lines correspond to the best linear fits (from [OG014]).

A related method, proposed in [25] where it was applied to the Anderson model, is to extract the singularity spectrum directly from the distribution of intensities $|\psi_i|^2$, by transforming (5.35) to

$$P_N(\alpha) = C_N N^{f(\alpha)-d}, \tag{5.43}$$

where C_N a normalization constant. The scaling of this constant can be obtained by evaluating the normalization condition $C\int_0^\infty N^{f(\alpha)-d}d\alpha$ by the Laplace method for large N, yielding $C_N \sim \sqrt{\ln N}$. Extracting numerically C_N as the maximum of $P_N(\alpha)$, the singularity spectrum appears as $d + \ln(P_N(\alpha)/C_N)/\ln N$, so that curves $P_N(\alpha)$ for different N should collapse onto the same $f(\alpha)$ after this rescaling.

5.3.2 Box counting method

The multifractal exponents for a vector ψ of size N can be obtained by dividing it into $N_b = N/\ell$ boxes B_k of size ℓ. Each box has measure $\mu_k(\ell) = \sum_{i\in B_k} |\psi_i|^2$, $1 \le k \le N_b$. Multifractal dimensions describe the scaling of the partition function

$$Z(q,\ell) \equiv \sum_{k=1}^{N_b} \mu_k(\ell)^q \propto \ell^{\tau_q}, \qquad \tau_q \equiv D_q(q-1), \tag{5.44}$$

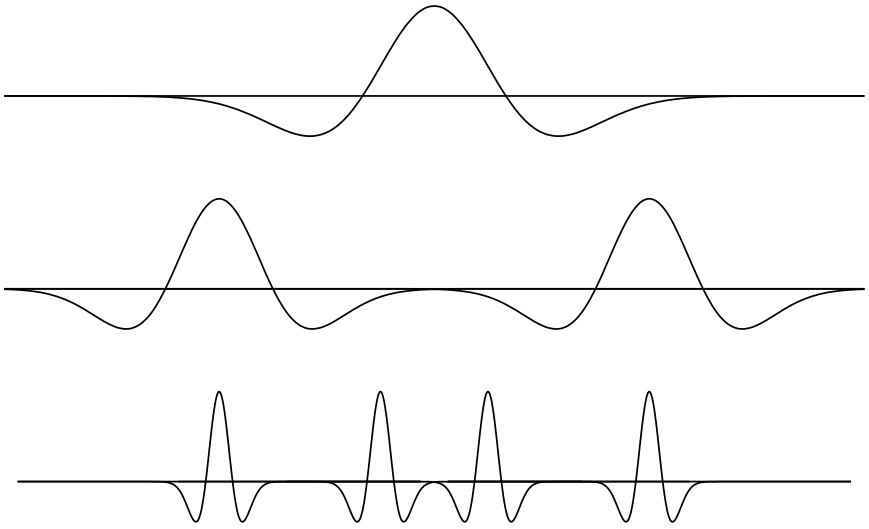

Figure 5.5: 'Mexican hat' continuous wavelet basis.

which is a coarse-grained version of (5.13)–(5.15). In practice, either the system size N is fixed and box sizes ℓ goes 0, or ℓ is fixed and the system size goes to infinity. For fixed N, removing the smallest boxes often yield more reliable results [OG027]. The asymptotic large–N result may then be obtained by a fit of the form $\tau_q(N) = \tau_q(\infty) + f_q(\ell)$ (see e.g. [191]).

Introducing the normalized measures $\mu_k(q,\ell) = \mu_k(\ell)^q / \sum_i \mu_i(\ell)^q$, one can also extract directly the singularity spectrum (5.29) and the exponents α by calculating

$$\alpha_q = \lim_{\ell/N \to 0} \frac{\sum_i \mu_i(q,\ell) \ln \mu_i(\ell)}{\ln(\ell/N)} \tag{5.45}$$

and

$$f(\alpha_q) = \lim_{\ell/N \to 0} \frac{\sum_i \mu_i(q,\ell) \ln \mu_i(q,\ell)}{\ln(\ell/N)}, \tag{5.46}$$

as was proposed in [192]. This is typically used in numerical investigations of the 3D Anderson model [193, 190].

It was checked in [190] for the Anderson model or in [OG027] for the intermediate maps that the box counting method gives results similar to the moment method, although in the Anderson case the moment method with ensemble averaging was claimed to give better results [190].

5.3.3 Wavelet transform

Wavelets have been introduced as an efficient approach to data analysis and data compression, and have become an essential tool for image and sound processing [194]. The wavelet transform is a kind of generalization of the Fourier transform which allows to probe a signal not only at various frequencies but also at various times.

Wavelets can therefore be used as a versatile tool to multiscale analysis, in particular to describe multifractality properties of phenomena such as DNA sequences, turbulence, or cloud structure [187].

The continuous wavelet transform is based on a family of functions which form a basis (as does the Fourier basis). From a square-integrable function g (the 'mother function') one constructs the basis functions as translated and rescaled copies of g, namely

$$g_{a,b}(x) = \frac{1}{A} g\left(\frac{x-B}{A}\right). \tag{5.47}$$

Here A corresponds to the scaling variable and B to the translation variable. An example of such a basis is given in Fig. 5.5. The continuous wavelet transform of a function $\psi(x)$ is the expansion of $\psi(x)$ onto this wavelet basis, and can be expressed as

$$T_\psi(A,B) = \frac{1}{A}\int dx\, \psi(x)\; g\left(\frac{x-B}{A}\right). \tag{5.48}$$

It probes the local variations of ψ in the vicinity of point B and at a scale A. Note that this is close to what does the box-counting approach. The 'wavelet transform modulus maxima method' allows to extract multifractal exponents by considering the maxima of the wavelet transform at each scale [187].

Analogously as for the discrete Fourier transform, discrete wavelet transforms can be defined starting from a discrete mother wavelet. Such discrete wavelet transforms are adapted to our purpose, where the vectors we want to probe are finite-dimensional. We based our investigations in [OG019] on the 'Daubechies 4' wavelet transform corresponding to vector sizes $N = 2^n$ [195], whose mother wavelet is given by

$$g \to \{\frac{1+\sqrt{3}}{4\sqrt{2}}, \frac{3+\sqrt{3}}{4\sqrt{2}}, \frac{3-\sqrt{3}}{4\sqrt{2}}, \frac{1-\sqrt{3}}{4\sqrt{2}}\} \tag{5.49}$$

and the family of basis vectors, illustrated by Fig. 5.6, is constructed from rescalings $A = 1, 1/2, 1/4, ...1/2^{n-1}$ and translations $B \in \{1, 2, \ldots, 1/A\}$ at scale A. Similarly as the fast Fourier transform, this wavelet transform can be implemented efficiently under the form of a unitary transformation.

Multifractal exponents can be extracted from the 'wavelet transform modulus maxima method'. More specifically, we define the partition function

$$\mathcal{Z}(q,A) = \sum_{B_i}\left[\frac{|T_{|\psi|^2}(A,B_i)|}{\sum_{B_i}|T_{|\psi|^2}(A,B_i)|}\right]^q \tag{5.50}$$

where B_i are the local maxima of the wavelet transform of $|\psi_i|^2$ at scale A. Then the multifractal exponents τ_q can be extracted in the limit $A \to 0$ through the scaling

$$Z(q,A) \underset{A\,\to\,0^+}{\sim} A^{\tau_q}. \tag{5.51}$$

Note that a variation of this approach was developed in [196, 197], where the sum of the values of the discrete wavelet transform, properly normalized at each scale, are used instead of the maxima. This was tested in [OG019] on the multiplicative cascade, showing that for large N the correct exponents were extracted.

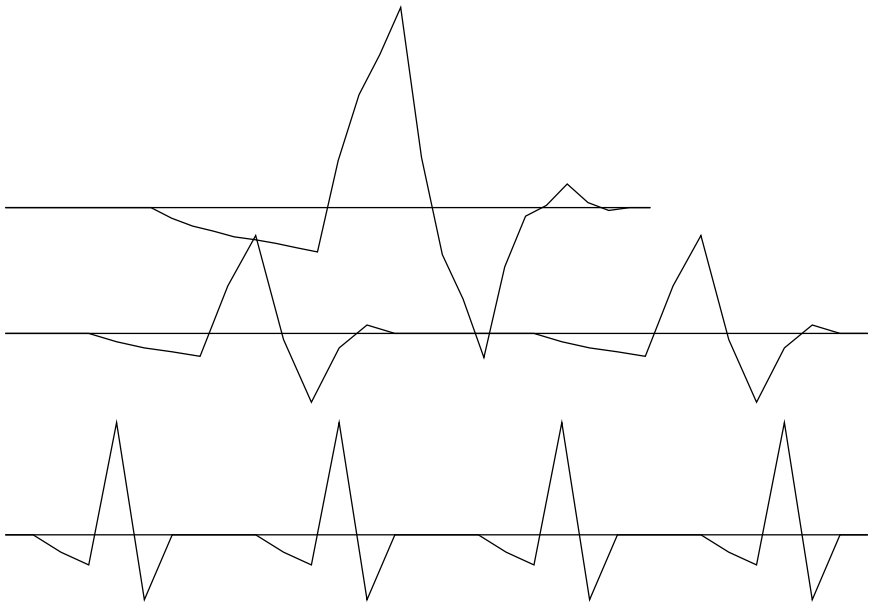

Figure 5.6: Daubechies wavelet basis used in [OG019].

Note that we proposed in [OG019] a quantum algorithm which simulates the discrete wavelet transform on a quantum computer (see Chapter 9).

5.4 Experiments

Progress in experimental techniques allow to observe finer and finer properties of the wavefunctions of quantum or wave systems, as well as to perform experiments with unprecedented control on the dynamics of the systems studied.

Various experiments were performed with cold atoms in optical lattices [34, 35, 36]. In this setting, Anderson transition is observed in momentum space, using the kicked rotor model (see Section 4.1.3). A cloud of about 10^7 Cesium atoms is confined in a magneto-optic trap. Atoms are cooled down to $\sim 3.2\mu$K. They are then submitted to a stationary laser beam in a fundamental Gaussian mode of width larger than that of the cloud. This beam can be pulsed, with pulses of about 0.6 to 1μs. The velocity distribution of the cloud is then measured via Raman velocimetry. In the localized case, the momentum distribution does not vary with time evolution, while in the delocalized case it has a diffusive behavior. At criticality, it displays an anomalous diffusive behavior [36]. Other experiments involve acoustic waves in random media: sound localization was observed in random elastic networks made out of randomly packed aluminium beads [198], and the corresponding multifractal spectrum was investigated in [39]. Further experiments were realized on Bose-Einstein condensates trapped in a region of space and released in a laser speckle potential [31, 32, 33]. Recently many experiments have moved to the underastanding of the role of interactions between particles on the localization transition. This has been investigated e.g. in [199] where multifractality of spatial correlations of the local

density of states was measured in $Ga_{1-x}Mn_x$ samples close to the transition for electronic states in the presence of doping-induced disorder, or in ultracold atoms trapped in 1D quasi-periodic lattices [200].

Chapter 6

Perturbation theory

6.1 Introduction

Multifractal dimensions are hard to handle analytically. In Chapter 7 we will present numerical results obtained for the multifractal dimensions of various models. It is however possible in some cases to treat analytically the limiting cases.

The analytical approach to investigate models such as banded matrices rests on a mapping onto the supersymmetric nonlinear sigma model [201], which is valid in the "large band" (or weak multifractality) limit where matrices are close to the usual random matrix case. The other limit of "narrow band" (or strong multifractality) corresponds to the situation where quantum states are almost localized. It can be investigated analytically by the Levitov renormalization-group technique [134], which consists in considering off-diagonal terms of a Hamiltonian H as a perturbation, and taking into account resonant interactions between energy levels, as exemplified below in Section 6.5. A more rigourous approach for the "narrow band" limit is the virial expansion approach [202, 203, 204] or its supersymmetric version [205]. A third approach based on standard perturbation theory was discussed in [174]; it treats perturbatively both the eigenvectors and its normalization, so that the ratios $\sum_n |\psi_n(\alpha)|^{2q}/(\sum_n |\psi_n(\alpha)|^2)^q$ are regular, even though perturbation terms are singular for $q > 1/2$.

The formulas obtained by these approaches take the same form for most of the systems that we will consider here. In the 'strong multifractality' regime for $q > 1/2$, D_q at first order takes the form

$$D_q = 4g\rho(E)\, s\, \frac{\sqrt{\pi}\,\Gamma\left(q-\frac{1}{2}\right)}{\Gamma(q)} \tag{6.1}$$

where $\rho(E)$ is the density of diagonal elements (which corresponds to the density of states in the unperturbed diagonal matrix case). For later purposes, we will put it under the form

$$D_q = \frac{\Gamma(q-1/2)}{\sqrt{\pi}\Gamma(q)}(1-\eta), \qquad \eta = 1 - 4g\rho(E)\, s\pi. \tag{6.2}$$

For $q < 1/2$, the expression is

$$D_q = \frac{2q-1}{q-1} + \frac{\Gamma(1/2-q)}{\sqrt{\pi}\,(q-1)\Gamma(-q)}(1-\eta) \tag{6.3}$$

with η as in (6.2). This regime corresponds to almost diagonal matrices, which is usually associated with a small value of the map parameter, $g \ll 1$. In the PRBM model it corresponds to a small band size; in Calogero models (4.37), (4.47) and (4.59), or in RS model (4.85), it corresponds to the limit $g \to 0$.

In the opposite 'weak multifractality' regime, where quantum states are almost extended, multifractal dimensions are close to 1. This regime is reached when quantum maps get close to a full matrix: $g \gg 1$ in PRBM or in Calogero models. For the RS ensemble it is reached in the vicinity of all integer points $g = \kappa$ with $|\kappa| \geq 1$. This regime was investigated for PRBM in the framework of the supersymmetric nonlinear sigma model. As we will see below, for our models it can be treated by standard perturbation theory. In this case, at first order, D_q takes the form

$$D_q = 1 - q\eta, \tag{6.4}$$

with η some system-dependent constant. The linear behaviour of D_q in this regime translates into a parabolic singularity spectrum $f(\alpha)$.

In the present chapter we illustrate our analytic perturbation-theoretic approach yielding analytical formulas for multifractal dimensions. In our papers [OG030, OG032, OG034], we derived first-order perturbation expansions for various models. The method is quite general. It was presented explicitly for the Calogero models in [OG032] and [OG034]. Here, as an illustration, we will concentrate on one example, namely the Ruijsenaars-Schneider ensemble (4.85). The reader may jump over this chapter whose aim is to derive the expressions for multifractal dimensions D_q for Ruijsenaars-Schneider, Eqs. (6.21) and (6.59), which correspond to (6.4) and (6.2) respectively. This chapter makes a (hopefully) pedagogic presentation of the calculations, and provides some detail on the explicit derivation of D_q in the two limiting regimes, in a way that was not written elsewhere.

6.2 Perturbative approach

We denote eigenfunctions and eigenvalues respectively by $\Psi_n(\alpha)$ and λ_α. Multifractal dimensions are given by the asymptotic behaviour of

$$\sum_n |\Psi_n(\alpha)|^{2q} \sim N^{-D_q(q-1)} \tag{6.5}$$

at large N. In the unperturbed case with $\epsilon = 0$, multifractal dimensions are given by $D_q^{(0)}$. At $\epsilon > 0$, fractal dimensions are given by $D_q = D_q^{(0)} - \frac{q}{2}d_q$, with d_q some small number, so that

$$\sum_n |\Psi_n(\alpha)|^{2q} \sim N^{-(D_q^{(0)} - q d_q/2)(q-1)} \simeq \frac{1}{N^{(q-1)D_q^{(0)}}}\left(1 + \frac{q(q-1)}{2} d_q \ln N\right). \tag{6.6}$$

The two limiting regimes are the regime of weak multifractality, where unperturbed eigenvectors are extended, and the regime of strong multifractality, where unperturbed eigenvectors are localized. In the weak multifractality limit, the matrix is full, $D_q^{(0)} = 1$ and moments of the eigenvectors can be expanded as

$$\sum_n |\Psi_n(\alpha)|^{2q} \sim \frac{1}{N^{q-1}}(1 + \frac{q(q-1)}{2} d_q \ln N). \tag{6.7}$$

In the strong multifractality limit the matrix is almost diagonal and $D_q^{(0)} = 0$, so that

$$\sum_n |\Psi_n(\alpha)|^{2q} \sim 1 + \frac{q(q-1)}{2} d_q \ln N. \tag{6.8}$$

We will first present the weak multifractality limit where κ is a nonzero integer [OG032]. The strong multifractality limit corresponds to g close to $\kappa = 0$.

6.3 Our model

Recall from Eq. (4.85) that the Ruijsenaars-Schneider ensemble consists of $N \times N$ unitary matrices of the form

$$U_{mn} = \frac{\mathrm{e}^{\mathrm{i}\Phi_m}}{N} \frac{1 - \mathrm{e}^{2\pi \mathrm{i} g}}{1 - \mathrm{e}^{2\pi \mathrm{i}(m-n+g)/N}}, \tag{6.9}$$

with Φ_m independent random phases uniformly distributed between 0 and 2π.

We will consider perturbation expansion of (6.9) around an integer κ, setting $g = \kappa + \epsilon$. We set $M_{mn} = U_{mn} e^{-i\pi\epsilon(1-1/N)}$. This only rescales U_{mn} by a trivial factor, but has the advantage that the matrix M can be expressed as

$$M_{mn} = \delta_{m-n+\kappa} \frac{e^{i\Phi_m}}{N} \frac{\sin \pi\epsilon}{\sin(\pi\epsilon/N)} + (1 - \delta_{m-n+\kappa}) \frac{(1 - e^{2\pi i\epsilon}) e^{-i\pi\epsilon(1-1/N)}}{1 - e^{2\pi i(m-n+\kappa+\epsilon)/N}}. \tag{6.10}$$

Thus it is such that both terms have a definite limit when $\epsilon \to 0$. First-order expansion of M_{mn} reads

$$M_{mn} \simeq e^{i\Phi_m} \delta_{m-n+\kappa} - \frac{2i\pi\epsilon}{N} e^{i\Phi_m} \frac{1 - \delta_{m-n+\kappa}}{1 - e^{2\pi i(m-n+\kappa)/N}}. \tag{6.11}$$

6.4 Weak multifractality regime

For simplicity we consider cases where κ and N are coprime, so that we can define κ^{-1} as the inverse of κ modulo N. Unperturbed eigenstates, that is, eigenvectors of $e^{i\Phi_m}\delta_{m-n+\kappa}$, are given by

$$\Psi_n^{(0)}(\alpha) = \frac{1}{\sqrt{N}} e^{iS_{\kappa^{-1}n}(\alpha)}, \qquad S_n(\alpha) = \frac{2\pi}{N} n\alpha + n\tilde{\Phi} - \sum_{j=0}^{n-1} \Phi_{\kappa j} \tag{6.12}$$

with eigenvalues

$$\lambda_\alpha^{(0)} = e^{i\tilde{\Phi} + \frac{2i\pi}{N}\alpha}, \tag{6.13}$$

where $\tilde{\Phi} = \frac{1}{N}\sum_{j=0}^{N-1}\Phi_j$. Standard first-order perturbation expansion gives

$$\Psi_n(\alpha) = \Psi_n^{(0)}(\alpha) + \sum_\beta C_{\alpha\beta}\Psi_n^{(0)}(\beta), \tag{6.14}$$

with

$$C_{\alpha\beta} = \frac{\langle \Psi_m^{(0)*}(\beta)|M_{mn}^{(1)}|\Psi_n^{(0)}(\alpha)\rangle}{\lambda_\alpha^{(0)} - \lambda_\beta^{(0)}} \tag{6.15}$$

and $M_{mn}^{(1)}$ the order-ϵ (off-diagonal) term in (6.11). Replacing $\Psi_n^{(0)}$ by its explicit value in (6.14) we get

$$|\Psi_n(\alpha)|^2 = \frac{1}{N}\left(1 + Q_n(\alpha) + Q_n^*(\alpha) + Q_n(\alpha)Q_n^*(\alpha)\right) \tag{6.16}$$

with

$$Q_n(\alpha) = \sum_\beta e^{2i\pi\beta n/N} C_{\alpha,\beta+\alpha}. \tag{6.17}$$

The normalization condition of the wavefunction reads

$$1 = \sum_n |\Psi_n(\alpha)|^2 = 1 + \frac{1}{N}\sum_n \left(Q_n(\alpha) + Q_n^*(\alpha) + Q_n(\alpha)Q_n^*(\alpha)\right) \tag{6.18}$$

Taking (6.16) to the power q we get, up to order 2 in ϵ,

$$\begin{aligned} |\Psi_n(\alpha)|^{2q} &= \frac{1}{N^q}\left[1 + q(Q_n(\alpha) + Q_n^*(\alpha) + Q_n(\alpha)Q_n^*(\alpha))\right. \\ &+ \left.\frac{q(q-1)}{2}(Q_n(\alpha) + Q_n^*(\alpha))^2\right]. \end{aligned} \tag{6.19}$$

Summing (6.19) over n and using (6.18) we get

$$\sum_n |\Psi_n(\alpha)|^{2q} = \frac{1}{N^q}\left[N + \frac{q(q-1)}{2}\sum_n (Q_n(\alpha) + Q_n^*(\alpha))^2\right]. \tag{6.20}$$

Identifying (6.20) and (6.6), we get

$$\frac{1}{N}\sum_n (Q_n(\alpha) + Q_n^*(\alpha))^2 \simeq d_q \ln N, \tag{6.21}$$

so that the correction to the unperturbed multifractal dimension is given by the logarithmic asymptotic behaviour of the sum in (6.21).

From the definition (6.17) of Q_n we have

$$\begin{aligned} \frac{1}{N}\sum_n Q_n(\alpha)^2 &= \frac{1}{N}\sum_{n,\beta,\beta'} e^{2i\pi(\beta+\beta')n/N} C_{\alpha,\beta+\alpha}C_{\alpha,\beta'+\alpha} \\ &= \sum_{\beta,\beta'} C_{\alpha,\beta+\alpha}C_{\alpha,\beta'+\alpha}\delta_{\beta+\beta'} \\ &= \sum_\beta C_{\alpha,\alpha+\beta}C_{\alpha,\alpha-\beta}, \end{aligned} \tag{6.22}$$

and similarly

$$\frac{1}{N}\sum_n Q_n(\alpha)Q_n^*(\alpha) = \sum_\beta C_{\alpha,\alpha+\beta}C^*_{\alpha,\alpha+\beta}. \tag{6.23}$$

We are interested in quantities averaged over all eigenvectors and random phases. We thus have to perform a sum over α and an integral over the Φ_j. The explicit expression of $C_{\alpha,\beta+\alpha}$ is

$$\begin{aligned} C_{\alpha,\beta+\alpha} &= \frac{i}{2N}\sum_{mn}\frac{t_{(s-r+1)\kappa}}{\sin(\pi\beta/N)}\exp\left[i(r-s-1)(\frac{2\pi\alpha}{N}+\tilde{\Phi})\right. \\ &- \left.\frac{2i\pi}{N}(s+\frac{1}{2})\beta - i\sum_{j=0}^{r-1}\Phi_{\kappa j} + i\sum_{j=0}^{s}\Phi_\kappa\right], \end{aligned} \tag{6.24}$$

with $r=\kappa^{-1}n$ and $s=\kappa^{-1}m$, and

$$t_x = \frac{\pi\epsilon}{N}\frac{e^{-i\pi x/N}}{\sin\pi x/N} \quad \text{if } x\neq 0, \qquad 0 \text{ otherwise.} \tag{6.25}$$

The only dependence on α in (6.24) is $\exp[2i\pi(r-s-1)\alpha/N]$. Upon averaging over α in (6.22), one gets a coefficient

$$\frac{1}{N}\sum_\alpha e^{\frac{2i\pi}{N}(r-s-1+r'-s'-1)\alpha} = \delta_{r-s+r'-s'-2}, \tag{6.26}$$

which kills the terms $\tilde{\Phi}$ in $C_{\alpha,\beta+\alpha}C_{\alpha,\alpha-\beta}$ (the primed indices in (6.26) correspond to the sum appearing in $C_{\alpha,\alpha-\beta}$). The averaging of $C_{\alpha,\alpha+\beta}C_{\alpha,\alpha-\beta}$ over random angles then contains a coefficient

$$\Big\langle \exp\left[-i\sum_{j=0}^{r-1}\Phi_\kappa + i\sum_{j=0}^{s}\Phi_\kappa - i\sum_{j=0}^{r'-1}\Phi_\kappa + i\sum_{j=0}^{s'}\Phi_\kappa\right]\Big\rangle. \tag{6.27}$$

Since condition (6.26) imposes that $r-s+r'-s'-2=0$, and since the term $t_{(s-r+1)\kappa}$ in $C_{\alpha,\beta+\alpha}$ implies that contributions with $s-r+1=0$ vanish, the average (6.27) can only be nonzero when $s=r'-1$ and $s'=r-1$. This yields

$$\Big\langle C_{\alpha,\alpha+\beta}C_{\alpha,\alpha-\beta}\Big\rangle_{\alpha,\Phi} = \frac{1}{4N^2}\sum_{rs}\frac{t_{(s-r+1)\kappa}t_{-(s-r+1)\kappa}}{\sin^2(\pi\beta/N)}e^{-\frac{2i\pi}{N}(s-r+1)\beta}. \tag{6.28}$$

Changing variables $s-r+1=x$ and summing over β, we get from (6.22) and (6.25)

$$\Big\langle \frac{1}{N}\sum_n Q_n(\alpha)^2\Big\rangle_{\alpha,\Phi} = -\frac{\pi^2\epsilon^2}{4N^3}\sum_x\frac{1}{\sin^2(\pi\kappa x/N)}\sum_\beta\frac{e^{-\frac{2i\pi}{N}x\beta}}{\sin^2(\pi\beta/N)}. \tag{6.29}$$

In a similar way, averaging $C_{\alpha,\alpha+\beta}C^*_{\alpha,\alpha+\beta}$ over α yield, instead of (6.26), a coefficient $\delta_{r-s-r'+s'}$, and the average over Φ_j then yields the condition $r=r'$ and $s=s'$, so that

$$\Big\langle C_{\alpha,\alpha+\beta}C^*_{\alpha,\alpha+\beta}\Big\rangle_{\alpha,\Phi} = \frac{1}{4N^2}\sum_{rs}\frac{|t_{(s-r+1)\kappa}|^2}{\sin^2(\pi\beta/N)} \tag{6.30}$$

and

$$\left\langle \frac{1}{N}\sum_n Q_n(\alpha)Q_n(\alpha)^* \right\rangle_{\alpha,\Phi} = \frac{\pi^2\epsilon^2}{4N^3}\sum_x \frac{1}{\sin^2(\pi\kappa x/N)}\sum_\beta \frac{1}{\sin^2(\pi\beta/N)}. \qquad (6.31)$$

Putting together Eqs. (6.30) and (6.31), we get

$$\begin{aligned}\left\langle \frac{1}{N}\sum_n (Q_n(\alpha)+Q_n^*(\alpha))^2 \right\rangle_{\alpha,\Phi} &= \frac{\pi^2\epsilon^2}{N^3}\sum_x \frac{1}{\sin^2(\pi\kappa x/N)}\sum_\beta \frac{\sin^2(\pi\beta x/N)}{\sin^2(\pi\beta/N)} \\ &= \frac{\pi^2\epsilon^2}{N^3}\sum_{x=1}^{N-1}\frac{x(N-x)}{\sin^2(\pi\kappa x/N)}. \qquad (6.32)\end{aligned}$$

From (6.21) we know that the lowest-order contribution to the multifractal exponent is given by the logarithmic behavior of the sum (6.32) for large N. This logarithmic contribution originates from regions where the numerator in (6.32) vanishes, partly compensating the vanishing in the denominator. This occurs whenever $\kappa x/N$ is close to an integer. Expanding the summand in the vicinity of singular points cN/κ, with $0 \le c \le \kappa$, the sum (6.32) can be rewritten

$$\begin{aligned}\frac{\pi^2\epsilon^2}{N^3}\sum_{x=1}^{N-1}\left(\frac{x(N-x)}{\sin^2(\pi\kappa x/N)} - \sum_{c=1}^{\kappa-1}\frac{x(N-x)}{\pi^2\kappa^2\left(\frac{x}{N}-\frac{c}{\kappa}\right)^2} - \frac{N^3}{\pi^2\kappa^2 x} - \frac{N^3}{\pi^2\kappa^2(N-x)}\right) \\ +\frac{\pi^2\epsilon^2}{N^3}\sum_{x=1}^{N-1}\left(\sum_{c=1}^{\kappa-1}\frac{x(N-x)}{\pi^2\kappa^2\left(\frac{x}{N}-\frac{c}{\kappa}\right)^2} + \frac{N^3}{\pi^2\kappa^2 x} + \frac{N^3}{\pi^2\kappa^2(N-x)}\right). \qquad (6.33)\end{aligned}$$

The first line is a Riemann sum which converges to the finite-valued integral

$$\pi^2\epsilon^2\int_0^1\left(\frac{y(1-y)}{\sin^2(\pi\kappa y)} - \sum_{c=1}^{\kappa-1}\frac{y(1-y)}{\pi^2\kappa^2\left(y-\frac{c}{\kappa}\right)^2} - \frac{1}{\pi^2\kappa^2 y} - \frac{1}{\pi^2\kappa^2(1-y)}\right)dy. \qquad (6.34)$$

The second line can be rewritten

$$\frac{\epsilon^2}{\kappa^2}\sum_{x=1}^{N-1}\sum_{c=1}^{\kappa-1}\left(\frac{1-2c/\kappa}{x-cN/\kappa} - \frac{1}{N} + N\frac{\frac{c}{\kappa}(1-\frac{c}{\kappa})}{(x-cN/\kappa)^2}\right) + \frac{\epsilon^2}{\kappa^2}\sum_{x=1}^{N-1}\frac{1}{x} + \frac{\epsilon^2}{\kappa^2}\sum_{x=1}^{N-1}\frac{1}{N-x}. \qquad (6.35)$$

Logarithmic contributions only come from the last two terms; finally, one has from (6.32)

$$\left\langle \frac{1}{N}\sum_n (Q_n(\alpha)+Q_n^*(\alpha))^2 \right\rangle_{\alpha,\Phi} \simeq \frac{2\epsilon^2}{\kappa^2}\ln N, \qquad (6.36)$$

and from (6.21)

$$D_q \simeq 1 - q\frac{(g-\kappa)^2}{\kappa^2}. \qquad (6.37)$$

6.5 Strong multifractality regime, $q > 1/2$

The strong multifractality limit corresponds to parameters g close to zero, that is $\kappa = 0$. In this regime matrices are almost diagonal. A way to obtain first-order corrections is to apply the Levitov renormalization-group technique, which consists in treating off-diagonal terms of the matrix M as a perturbation, that is, for $i \neq j$, $|M_{ij}| \ll |M_{ii}|$. The unperturbed matrix is diagonal, so that unperturbed eigenvectors are localized. States with $|M_{ii} - M_{jj}| < |M_{ij}|$ will be coupled by the perturbation (in resonance).

In the RS case, Eq. (6.11) becomes

$$M_{mn} \simeq e^{i\Phi_m}\delta_{m-n} - \frac{2i\pi\epsilon}{N} e^{i\Phi_m} \frac{1-\delta_{m-n}}{1-e^{2\pi i(m-n)/N}}. \tag{6.38}$$

Following [14, 21, 134, 137], the second order of perturbation theory for $q > 1/2$ is obtained by calculating the contributions of 2×2 submatrices of M along the main diagonal. More specifically, we are interested in the lowest orders of the local participation ratio

$$\frac{1}{\rho(\theta)} \langle \frac{1}{N} \sum_\alpha \sum_i |\Psi_i(\alpha)|^{2q} \delta(\theta - \theta_\alpha) \rangle, \tag{6.39}$$

where the average is performed over random realizations of angles Φ_i and over the N eigenvectors indexed by α, with eigenphases $\exp(i\theta_\alpha)$. Here $\rho(\theta) = 1/(2\pi)$ is the (uniform) density of eigenphases.

6.5.1 Order 0

At zeroth order of perturbation theory, the sum over α in (6.39) is replaced by a sum over all 1×1 submatrices of M. Eigenvectors of these matrices have a single component equal to 1, and eigenphases are given by $\theta_m^{(0)} = \Phi_m$, $1 \leq m \leq N$. Thus in (6.39), the sum over α has to be replaced by a sum over m submatrices. Each 1×1 matrix contributes by an amount

$$\sum_i |\Psi_i(\alpha)|^{2q} \delta(\theta - \theta_\alpha) = \delta(\theta - \Phi_m) \tag{6.40}$$

and the average of this quantity over random angles gives $1/(2\pi)$. Summing over all N submatrices, we finally get from (6.39)

$$\frac{1}{\rho(\theta)} \langle \frac{1}{N} \sum_\alpha \delta(\theta - \Phi_\alpha) \rangle = 1. \tag{6.41}$$

6.5.2 Order 1

At next order one has to consider the contribution from 2×2 submatrices

$$\begin{pmatrix} e^{i\Phi_m} & -\frac{2i\pi\epsilon}{N} \frac{e^{i\Phi_m}}{1-e^{2\pi i(m-n)/N}} \\ -\frac{2i\pi\epsilon}{N} \frac{e^{i\Phi_n}}{1-e^{-2\pi i(m-n)/N}} & e^{i\Phi_n} \end{pmatrix} = \begin{pmatrix} e^{i\Phi_m} & ihe^{i(\Phi_m+\chi)} \\ ihe^{i(\Phi_n-\chi)} & e^{i\Phi_n} \end{pmatrix} \tag{6.42}$$

with

$$-\frac{2\pi\epsilon}{N}\frac{1}{1-e^{2\pi i(m-n)/N}} = he^{i\chi} \tag{6.43}$$

($h \geq 0$ depends on m and n and is proportional to the small parameter ϵ). Setting $\gamma = (\Phi_m + \Phi_n)/2$ and $\beta = (\Phi_m - \Phi_n)/2$, eigenvalues are given by

$$\lambda_\sigma = e^{i\gamma}\left(\cos\beta + i\sigma\sqrt{h^2+\sin^2\beta}\right), \tag{6.44}$$

$\sigma = \pm 1$, and the corresponding eigenvectors (u_σ, v_σ) are given by

$$|u_\sigma|^2 = \frac{h^2}{\left(\sin\beta + i\sigma\sqrt{h^2+\sin^2\beta}\right)^2 + h^2}, \tag{6.45}$$

$$|v_\sigma|^2 = \frac{\left(\sin\beta + i\sigma\sqrt{h^2+\sin^2\beta}\right)^2}{\left(\sin\beta + i\sigma\sqrt{h^2+\sin^2\beta}\right)^2 + h^2} \tag{6.46}$$

(here we only need moduli square of the eigenvector components). In (6.39), the sum over α is replaced by a sum over pairs (m,n) with $m<n$, and each 2×2 matrix eigenvector (indexed by σ) contributes by an amount

$$S_{mn} = \sum_i |\Psi_i(\alpha)|^{2q}\delta(\theta-\theta_\alpha) = (|u_\sigma|^{2q} + |v_\sigma|^{2q})\delta(\theta-\theta_\sigma) \tag{6.47}$$

with θ_σ the eigenphase of λ_σ. The mean over α in (6.39) is replaced at this order by

$$\frac{1}{N}\sum_{m<n}\left(\langle S_{mn}\rangle - 1\right), \tag{6.48}$$

where the -1 is needed to cancel the contribution at order 0 already taken into account previously (see e.g. [14]). The average over Φ_m and Φ_n can be replaced by an average over γ and β. Since γ only appears in the factor $e^{i\gamma}$ in the eigenvalue λ_σ, each value of θ has an equal order-one contribution, so that the delta function in (6.47) can be removed. The $1/(2\pi)$ coming from the integration over γ is canceled by the $\rho(\theta)$ in the denominator of (6.39), so that the total order 1 term reads

$$\frac{1}{N}\sum_{m<n}\sum_{\sigma=\pm 1}\langle |u_\sigma|^{2q} + |v_\sigma|^{2q}\rangle, \tag{6.49}$$

where the brackets correspond to the remaining average over β. In (6.45) the change $\beta \to \beta + \pi$ exchanges eigenvectors, thus the integral over angle β can be restricted to $[-\pi/2, \pi/2]$. Changing variable β by setting $\sin\beta = h\sinh t$, components $|u_\sigma|^2$ and $|v_\sigma|^2$ can be rewritten as

$$|u_\sigma|^2 = \frac{1}{1+\exp(2\sigma t)}, \qquad |v_\sigma|^2 = \frac{1}{1+\exp(-2\sigma t)} \tag{6.50}$$

and the average over β becomes

$$\frac{1}{\pi}\int_{-\pi/2}^{\pi/2} d\beta(|u_\sigma|^{2q}+|v_\sigma|^{2q}) = \frac{h}{\pi}\int_{-\operatorname{arcsinh}\frac{1}{h}}^{\operatorname{arcsinh}\frac{1}{h}} dt \frac{\cosh t}{\sqrt{1-h^2\sinh^2 t}}\frac{2\cosh(qt)}{(2\cosh t)^q}, \quad (6.51)$$

which can in turn be rewritten as

$$\frac{h}{\pi}\int_{-\operatorname{arcsinh}\frac{1}{h}}^{\operatorname{arcsinh}\frac{1}{h}} dt \frac{\cosh t}{\sqrt{1-h^2\sinh^2 t}}\left(\frac{2\cosh(qt)}{(2\cosh t)^q}-1\right) + \frac{h}{\pi}\int_{-\operatorname{arcsinh}\frac{1}{h}}^{\operatorname{arcsinh}\frac{1}{h}} dt \frac{\cosh t}{\sqrt{1-h^2\sinh^2 t}}. \quad (6.52)$$

The second term in (6.52) can be evaluated and is equal to 1. It corresponds to the zeroth order. The first integral has a finite limit which is given by

$$\int_{-\infty}^{\infty} dt \cosh t\left(\frac{2\cosh(qt)}{(2\cosh t)^q}-1\right) = -\frac{\sqrt{\pi}\Gamma(q-\frac{1}{2})}{\Gamma(q-1)}. \quad (6.53)$$

Finally Eq. (6.49) becomes

$$\frac{2}{N}\sum_{m<n}\left(1-h\frac{\Gamma(q-\frac{1}{2})}{\sqrt{\pi}\Gamma(q-1)}\right). \quad (6.54)$$

As in the weak multifractality limit, we are only interested in the logarithmic dependence of (6.54). From (6.43) we have

$$h = \frac{\pi\epsilon}{N}\frac{1}{|\sin(\pi(m-n)/N)|}, \quad (6.55)$$

so that

$$\begin{aligned}\frac{1}{N}\sum_{m<n} h &= \frac{\pi\epsilon}{2N}\sum_{x=1}^{N-1}\frac{1}{\sin(\pi x/N)} \quad (6.56)\\ &= \frac{\pi\epsilon}{2N}\sum_{x=1}^{N-1}\left(\frac{1}{\sin(\pi x/N)}-\frac{N}{\pi x}-\frac{N}{\pi(1-x)}\right)+\frac{\epsilon}{2}\sum_{x=1}^{N-1}\left(\frac{1}{x}+\frac{1}{1-x}\right).\end{aligned}$$

The first sum is a Riemann integral which converges to

$$\frac{\pi\epsilon}{2}\int_0^1\left(\frac{1}{\sin(\pi x)}-\frac{1}{\pi x}-\frac{1}{\pi(1-x)}\right) = \epsilon\ln\frac{2}{\pi}. \quad (6.57)$$

The second term diverges logarithmically as $\epsilon\ln N$, so that finally the logarithmic term in (6.54) reads

$$-\frac{2\epsilon\Gamma(q-\frac{1}{2})}{\sqrt{\pi}\Gamma(q-1)}\ln N. \quad (6.58)$$

Identifying the $\ln N$ term in (6.8) and (6.58), we finally get $d_q = -\frac{4\epsilon\Gamma(q-\frac{1}{2})}{\sqrt{\pi}\Gamma(q+1)}$, so that finally

$$D_q = \frac{2\epsilon\Gamma(q-\frac{1}{2})}{\sqrt{\pi}\Gamma(q)}. \quad (6.59)$$

6.6 Strong multifractality regime, $q < 1/2$

In this regime usual perturbation theory applies. From an expansion of (6.10) we get at first order $|\Psi_\alpha(\alpha)| = 1$ and

$$|\Psi_m(\alpha)| = \frac{\pi\epsilon}{N} \frac{1}{|e^{i\Phi_\alpha} - e^{i\Phi_m}|} \frac{1}{|\sin(\pi(m-\alpha)/N)|} \tag{6.60}$$

for $m \neq \alpha$, so that

$$\langle \sum_{m\neq\alpha} |\Psi_m(\alpha)|^{2q} \rangle = \Big(\frac{\pi\epsilon}{N}\Big)^{2q} \sum_m \Big\langle \frac{1}{|e^{i\Phi_\alpha} - e^{i\Phi_m}|^{2q}} \Big\rangle \frac{1}{\sin^{2q}(\pi(m-\alpha)/N)}. \tag{6.61}$$

The average over random angles yields

$$\Big\langle \frac{1}{|e^{i\Phi_\alpha} - e^{i\Phi_m}|^{2q}} \Big\rangle = \frac{1}{2\pi} \int_0^{2\pi} d\varphi \frac{1}{|1-e^{i\varphi}|^{2q}} = \frac{\Gamma(\frac{1}{2}-q)}{2^{2q}\sqrt{\pi}\Gamma(1-q)}, \tag{6.62}$$

and the sum over m gives a term

$$\sum_{m\neq\alpha} \frac{1}{\sin^{2q}(\pi(m-\alpha)/N)} = \sum_{m=1}^{N-1} \frac{1}{\sin^{2q}(\pi m)/N} = -\frac{2^{2q+1}\Gamma(-2q)}{q\Gamma(-q)^2} N. \tag{6.63}$$

The moment (6.5) for $q < \frac{1}{2}$ thus reads

$$\langle \sum_m |\Psi_m(\alpha)|^{2q} \rangle = 1 - (\pi\epsilon)^{2q} \frac{\Gamma(\frac{1}{2}-q)}{2^{2q}\sqrt{\pi}\Gamma(1-q)} \frac{2^{2q+1}\Gamma(-2q)}{q\Gamma(-q)^2} N^{1-2q}, \tag{6.64}$$

which for $q < \frac{1}{2}$ is dominated by the term in N^{1-2q}. Using the scaling (6.5), at lowest order, multifractal dimensions are thus given by

$$D_q = \frac{2q-1}{q-1}. \tag{6.65}$$

Going to second order of perturbation theory involves calculating the order ϵ^2 in (6.60). The result obtained in [OG034] gives the dependence on ϵ as

$$D_q = \frac{2q-1}{q-1} + 2\epsilon \frac{\Gamma(1/2-q)}{\sqrt{\pi}(q-1)\Gamma(-q)}, \tag{6.66}$$

which corresponds to (6.3) with $\eta = 1 - 2\epsilon$.

Chapter 7

Numerical results

While the techniques mentioned in the previous chapter allow to derive analytical expressions in perturbative regimes, numerical simulations are, in many cases, the only way to access multifractal dimensions. Before turning to numerical results for the random matrix ensembles presented in Chapter 4, let us mention that multifractal analysis has been performed on quantum chaotic systems, such as the quantum baker's map (4.4), where sequences of states were found to have some multifractality [15], or on kicked rotors with a non-analytic potential $V(q) = \ln|q|$, where the value $D_2 = 0.65$ was extracted from the tail of the distribution of eigenvector components for iterates of a wavepacket initially localized [19]. Similarly, multifractal analysis was performed on certain interpolating ensembles discussed in Section 3.4 [206].

While Eqs. (6.2) and (6.4) provide expressions in the limiting regimes of strong or weak multifractality, numerical simulations provide results for intermediate regimes. We now turn to the presentation of our numerical results for the quantum systems considered here, and compare them, in the perturbative regimes, to analytical expressions discussed in the previous chapter.

7.1 Anderson model and Banded matrices

Multifractal properties of the 3D critical Anderson model were investigated very early. In [207] the value $D_2 = 1.7 \pm 0.3$ was obtained for the 3D model. It was also found that wavefunctions of the 2D model are self-similar at scales smaller than the localization length [207, 208].

Exponents τ_q and D_q as well as the singularity spectrum $f(\alpha)$ were calculated in [7], and later with more powerful computer techniques in [190, 25, 26]. The exponent μ governing the two-point correlation function (5.12) was obtained in [166], allowing to verify the relation $\mu = 1 - D_2/d$. Approximate analytic expressions could be obtained by means of an expansion in dimension $2+\epsilon$ with $\epsilon \ll 1$, and eigenfunctions were shown to be multifractal [4, 5, 209]. Many variations on this model were considered in the literature, for instance the 3D Anderson model with anisotropic hopping for weakly coupled chains and weakly coupled planes, where eigenstates were shown to display multifractal behavior at the metal-insulator transition, even for strong anisotropy [193].

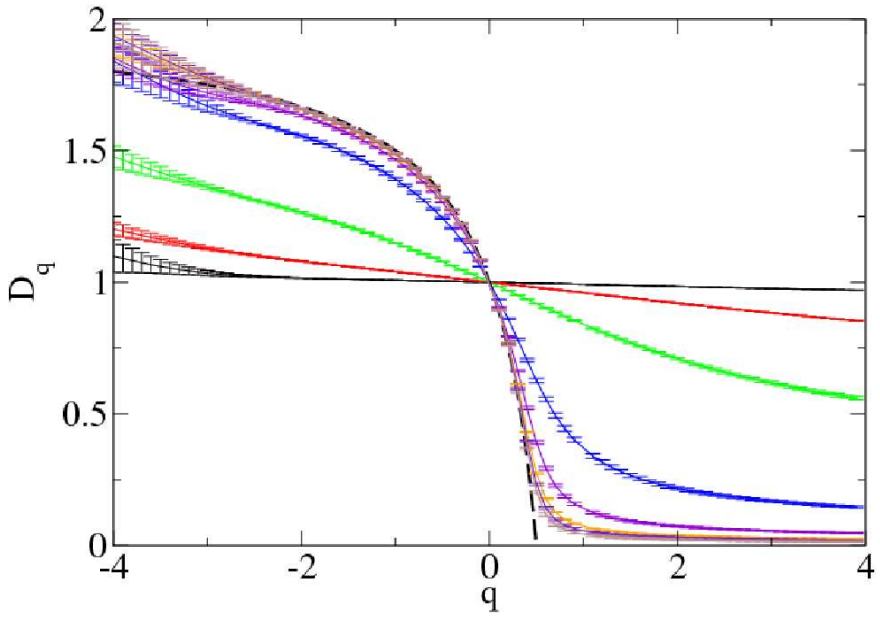

Figure 7.1: (Color online) Fractal dimensions D_q as a function of q for PRBM ensemble with $\beta = 2$. The parameter g is given (from top to bottom at $q = 4$) by $1/g = 0.1$ (black), 0.5 (red), 2 (green), 10 (blue), 30 (violet), 60 (orange), 80 (indigo), 100 (brown). Matrix sizes for numerical fit are $N = 2^n$, $8 \leq n \leq 12$. Average is performed over the $N/16$ eigenvectors closest to the eigenvalue $E = 0$. Number of random realizations of the matrix is between 2560 for $N = 2^8$ and 80 for 2^{12}. Dashed curve is the function $q \mapsto (2q-1)/(q-1)$.

One of the most important models of a random matrix ensemble displaying multifractal eigenstates is the power-law random banded matrix ensemble (PRBM) presented in Section 4.2.1. For all values of the coupling constant g its eigenfunctions are multifractal. When the parameter g is varied from large to small values, the system can be tuned from weak to strong multifractality, and thus plays the same role as the dimension in the Anderson model, where similarly a tuning from weak to strong multifractality can be obtained by varying d from $2+\epsilon$ to infinity.

Numerical results for the PRBM ensemble were calculated e.g. in [OG034] and are displayed in Fig. 7.1. Perturbation series expansions of the D_q were obtained for small and large values of the coupling constant g [137, 21]. In the strong multifractality limit $g \ll 1$ and for $q > 1/2$, the leading term of the perturbation expansion in g for eigenstates close to the center of the spectrum $E = 0$ reads

$$D_q \approx \frac{4g}{\sqrt{\pi}} \frac{\Gamma(q-1/2)}{\Gamma(q)} \begin{cases} \frac{1}{\sqrt{2}}, & \beta = 1 \\ \frac{\pi}{2\sqrt{2}}, & \beta = 2. \end{cases} \tag{7.1}$$

(For $\beta = 1$ this expression differs from the one in [137, 21] by a factor $\sqrt{2}$ due to the factor $1/2$ in my definition (4.11) of the matrix ensemble.) In the weak multifractality limit $g \gg 1$, the first-order of the expansion of D_q in powers of $1/g$

for eigenstates close to $E = 0$ is given by

$$D_q = 1 - q\frac{1}{2\pi\beta g} + \mathcal{O}\left(\frac{1}{g^2}\right). \tag{7.2}$$

Both expressions (7.1) and (7.2) take the form (6.2)–(6.4).

The distribution of IPR (5.13) was obtained numerically in [180] both for PRBM and the Anderson model, while in [179] the distribution of moments as well as the distribution of D_2 for finite N and its limiting behaviour was investigated. In [137], the calculation of cumulants for the distribution of IPR in the weak multifractality limit allowed to obtain an expression for the distribution itself, showing that asymptotically it displays a power-law tail of the form (5.37).

Numerical investigation of higher dimensional generalizations of the PRBM was performed e.g. in [210], where D_2 and $P(s)$ for the 2D and 3D PRBM was obtained. Boundary effects in this model were analyzed in [171].

Similarly, for the critical ultrametric matrix model defined in Section 4.2.1, perturbative expansion in the strong multifractality limit $J/W \ll 1$ reads [14]

$$D_q = \frac{J}{W}\frac{\sqrt{\pi}\,\Gamma(q-1/2)}{\sqrt{2}\,\ln 2\,\Gamma(q)}, \tag{7.3}$$

which again is of the form (6.2).

7.2 Intermediate systems

Multifractality and intermediate statistics for the intermediate map (4.26) were investigated in [OG014]. Multifractal dimensions are plotted in Fig. 7.2. Other numerical results related to the tail exponents x_q defined in (5.37) were investigated in [OG027] and are plotted in Fig. 7.3. We observed that at such small sizes, the values of $q_\pm$ extracted from these plots were not consistent with the regimes where the plots for τ_q and $\tau_q^{\rm typ}$ separate, indicating that the asymptotic regime is still not reached.

7.3 Classical N-body integrable systems

7.3.1 Calogero-Moser ensembles

Results of numerical computations for the CMr and CMt ensembles of Section 4.4 are presented in Figs. 7.4 and 7.5 (results for CMh are very similar to those of CMr). The curves for D_q go smoothly from a regime of weak multifractality where D_q is close to 1, to a regime of strong multifractality with D_q small at large q. These asymptotic regimes can be described accurately via our analytical expressions for multifractal dimensions given by Eqs. (6.2)–(6.4). For CM ensembles, matrices are Hermitian with diagonal elements p_j distributed as independent random Gaussian variables with mean 0 and variance 1, so that in the vicinity of $E = 0$ one has $\rho(E) \simeq 1/\sqrt{(2\pi)}$. In the limiting regime where $g \ll 1$, Eqs. (6.2) and (6.3) yield

$$D_q = 2\sqrt{2}gs\frac{\Gamma(q-1/2)}{\Gamma(q)}, \qquad q > 1/2 \tag{7.4}$$

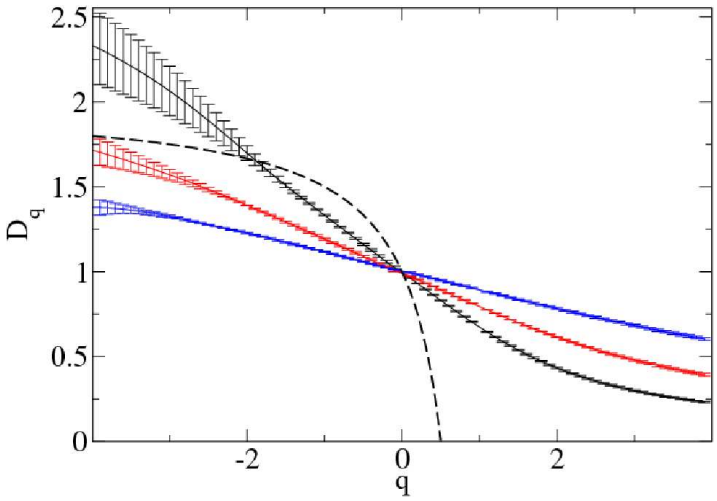

Figure 7.2: Fractal dimensions D_q as a function of q for intermediate map for $a = 1/b$ with (from bottom to top on the right) $b = 3$ (black), 5 (red), 9 (blue). Matrix sizes for numerical fit are the smallest integer $N' \geq N = 2^n$, $8 \leq n \leq 12$ such that $N' \equiv 1$ $[b]$. Average is performed over all eigenvectors. Number of random realizations of the matrix is between 1024 for $N = 2^8$ and 64 for 2^{12}. Dashed curve is the function $q \mapsto (2q-1)/(q-1)$.

and

$$D_q = \frac{2q-1}{q-1} + 2\sqrt{2}gs\frac{\Gamma(1/2-q)}{(q-1)\Gamma(-q)}, \qquad q < 1/2, \tag{7.5}$$

with $s = 1$ for CMr and CMh and $s = [\mu/\pi]$ for CMt. The accuracy of these expressions is illustrated in Fig. 7.6 for various parameter values.

In the weak multifractality limit $g \gg 1$, an approach similar to that of Section 6.4 gives a zero contribution to the multifractal dimension of CM ensembles at first order. Numerical results are consistent with that observation. As in the weak multifractality limit D_q is expected to be a straight line taking the value 1 at $q = 0$, it suffices to know one point of the plot. In Fig. 7.7 we show how D_1 goes to 0 as the map parameter g gets large.

7.3.2 Ruijsenaars-Schneider ensembles

Our numerical results for the RS ensemble are presented in Fig. 7.8. For RS ensemble, matrices are unitary and the density of eigenvalues is given by $\rho(E) = 1/(2\pi)$. Again one can compare numerics with our asymptotic expressions in the limiting regimes. For $g = \epsilon \ll 1$, Eqs. (6.59) and (6.66) hold. These formulas are illustrated in Fig. 7.9.

For the weak multifractality limit, Eq. (6.37) holds. Figure 7.10 shows that the agreement is remarkable.

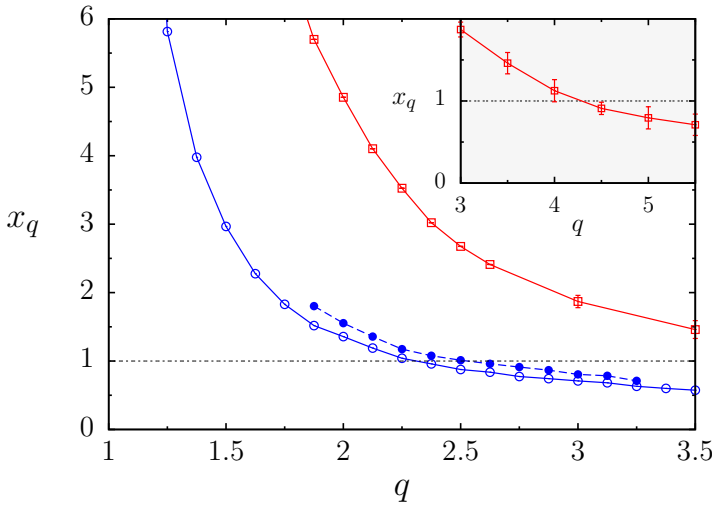

Figure 7.3: Tail exponents x_q for eigenvectors of the intermediate map (4.26) for $\gamma = 1/3$ with $N = 2^{12}$ (blue filled circles) and $N = 2^{14}$ (blue empty circles), and for $\gamma = 1/11$ with $N = 2^{14}$ (red squares). The multifractal analysis was done over 98304 vectors with box sizes ranging from 16 to 1024 and scales ranging from $2-12$ to $2-5$. Inset: Tail exponent for $\gamma = 1/11$ for larger values of q.

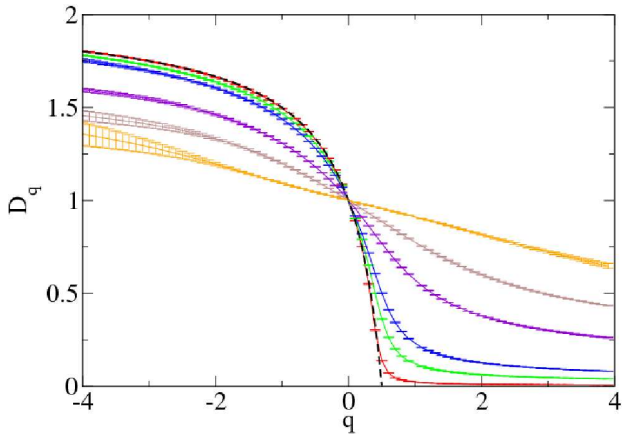

Figure 7.4: Fractal dimensions D_q as a function of q for CM_r ensemble for (from bottom to top at $q = 4$) $g = 0.005$ (red), 0.025 (green), 0.05 (blue), 0.15 (violet), 0.25 (brown), 0.4 (orange). The p_k are independent random variables distributed according to a Gaussian with mean 0 and variance 1. Matrix sizes for numerical fit are $N = 2^n$, $8 \leq n \leq 12$. Average is performed over the $N/16$ eigenvectors closest to the eigenvalue $E = 0$. Number of random realizations of the matrix is between 2560 for $N = 2^8$ and 80 for 2^{12}; error bars correspond to the standard deviation. Dashed curve is the function $q \mapsto (2q-1)/(q-1)$.

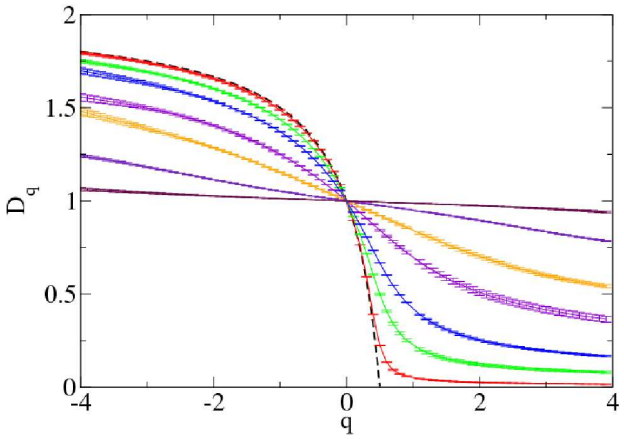

Figure 7.5: Fractal dimensions D_q as a function of q for CM_t ensemble for $\mu = 2\pi/N$ and (from bottom to top at $q = 4$) $g = 0.005$ (red), 0.025 (green), 0.05 (blue), 0.1 (violet), 0.15 (orange), 0.25 (indigo), 0.4 (brown). The p_k are independent random variables distributed according to a Gaussian with mean 0 and variance 1. Matrix sizes for numerical fit are $N = 2^n$, $8 \leq n \leq 12$. Average is performed over the $N/16$ eigenvectors closest to the eigenvalue $E = 0$. Number of random realizations of the matrix is between 2560 for $N = 2^8$ and 80 for 2^{12}. Dashed curve is the function $q \mapsto (2q-1)/(q-1)$.

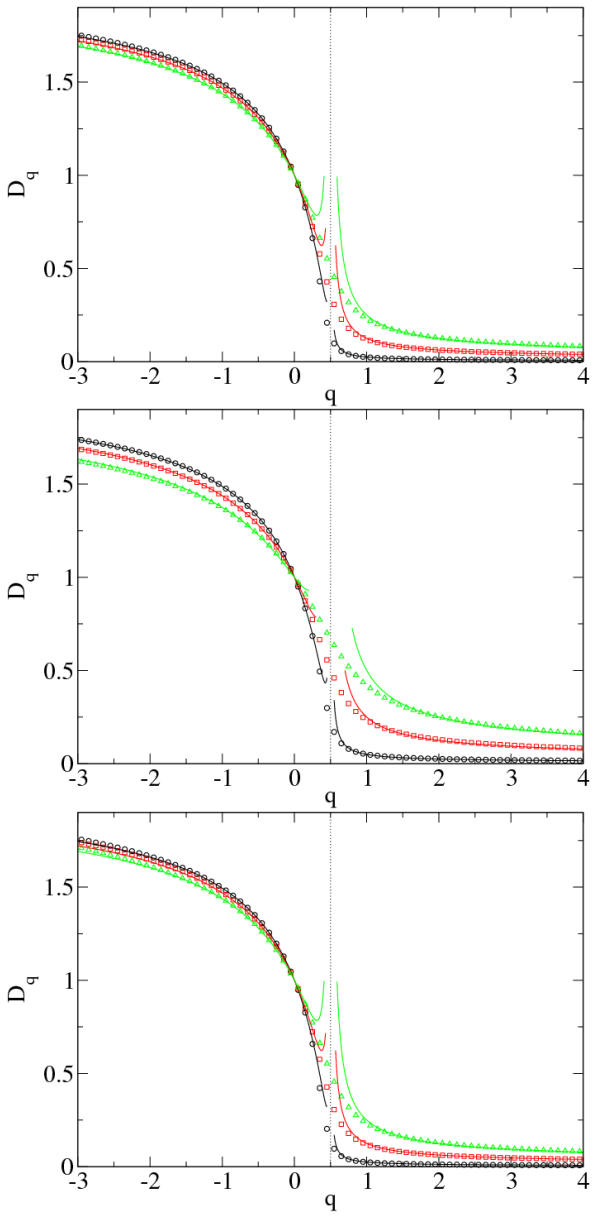

Figure 7.6: Fractal dimensions D_q as a function of q for CM_r (top), CM_t (middle) and CM_h (bottom) ensembles for $g = 0.005$ (black circles), 0.025 (red squares) and 0.05 (green triangles), and $\mu = 2\pi$. The p_k are independent random variables distributed according to a Gaussian with mean 0 and variance 1. Symbols are numerical results (symbols are larger than error bars). Solid lines correspond to formulas (7.4) and (7.5) with $s = 1$ for CM_r, formulas (7.4) and (7.5) with $s = [\mu/\pi] = 2$ for CM_t, and formulas (7.4) and (7.5) with $s = 1$ for CM_h. Matrix sizes for numerical fit are $N = 2^n$, $8 \leq n \leq 13$ ($N = 2^n + 1$ for CM_t). Average is performed over the $N/16$ eigenvectors closest to the eigenvalue $E = 0$. Number of random realizations of the matrix is between 2560 for $N = 2^8$ and 40 for 2^{13}. Dotted vertical line corresponds to $q = \frac{1}{2}$.

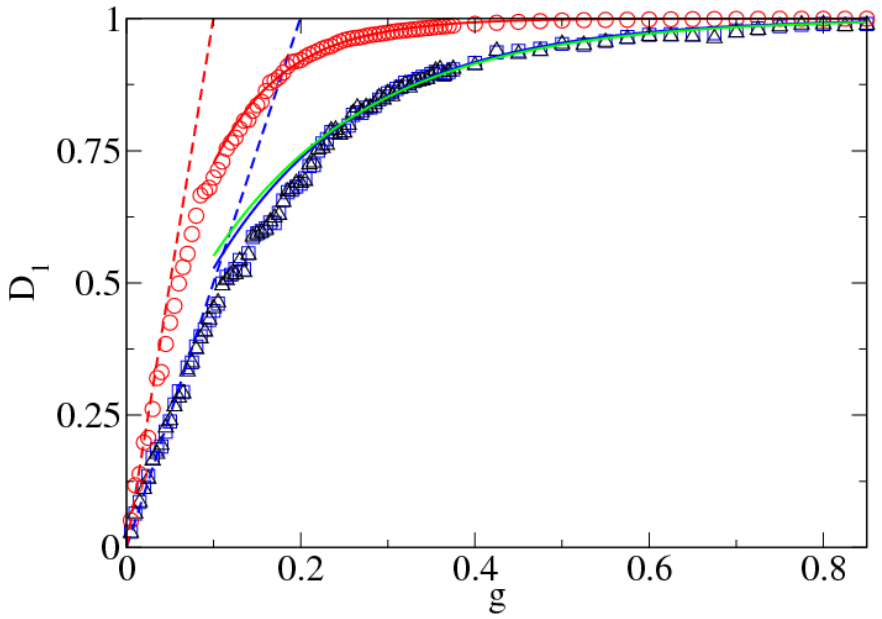

Figure 7.7: D_1 as a function of g for models CM_t (red circles), CM_r (blue squares) and CM_h (black triangles), obtained from 256 realizations of the random matrices for $N = 2^8$ to 32 for $N = 2^{11}$ (only $N/16$ central vectors are considered). Dashed lines indicate the leading perturbation series results for small g: $D_1 = 2\sqrt{2\pi}sg$ with $s = 1$ for models CM_r and CM_h, and $s = 2$ for model CM_t. Solid lines indicate the fits for large g: $D_1 \approx 1 - 0.85\mathrm{e}^{-5.8g}$ for model CM_r, $D_1 \approx 1 - 0.78\mathrm{e}^{-5.5g}$ for model CM_h, and $D_1 \approx 1 - .92\mathrm{e}^{-12.2g}$ for model CM_t.

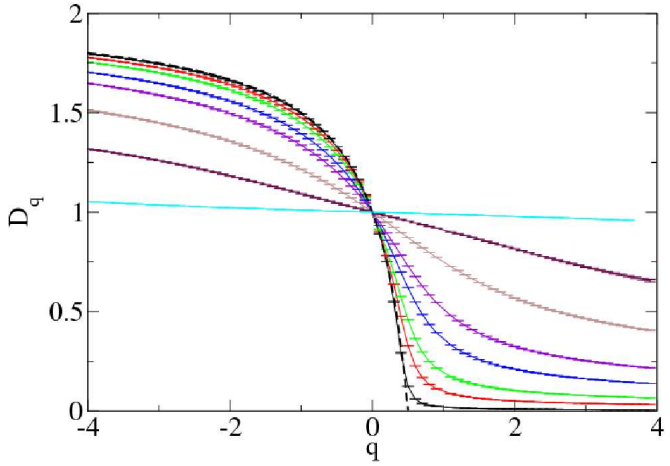

Figure 7.8: Fractal dimensions D_q as a function of q for RS ensemble for (from bottom to top at $q = 4$) $a = 0.01$ (black), 0.05 (red), 0.1 (green), 0.2 (blue), 0.3 (violet), 0.5 (brown), 0.7 (maroon), 0.9 (cyan). Matrix sizes for numerical fit are $N = 2^n$, $8 \leq n \leq 12$. Average is performed over all eigenvectors. Number of random realizations of the matrix is between 1024 for $N = 2^8$ and 64 for 2^{12}. Dashed curve is the function $q \mapsto (2q-1)/(q-1)$.

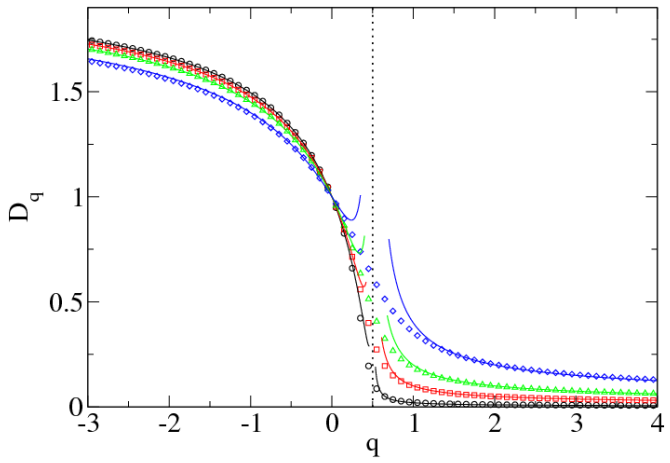

Figure 7.9: Fractal dimensions D_q as function of q for RS ensemble for $g = 0.01$ (black circles), 0.05 (red squares), 0.1 (green triangles) and 0.2 (blue diamonds). The Φ_k are independent random variables distributed uniformly in $[0, 2\pi]$. Symbols are numerical results (symbols are larger than error bars), solid lines correspond to the formula of Eqs. (6.59) and (6.66) with $\epsilon = g$. Matrix sizes for numerical fit are $N = 2^n$, $8 \leq n \leq 12$. Average is performed over all eigenvectors. Number of random realizations of the matrix is from 32 for $N = 2^8$ to 2 for 2^{12}. Dotted vertical line corresponds to $q = \frac{1}{2}$.

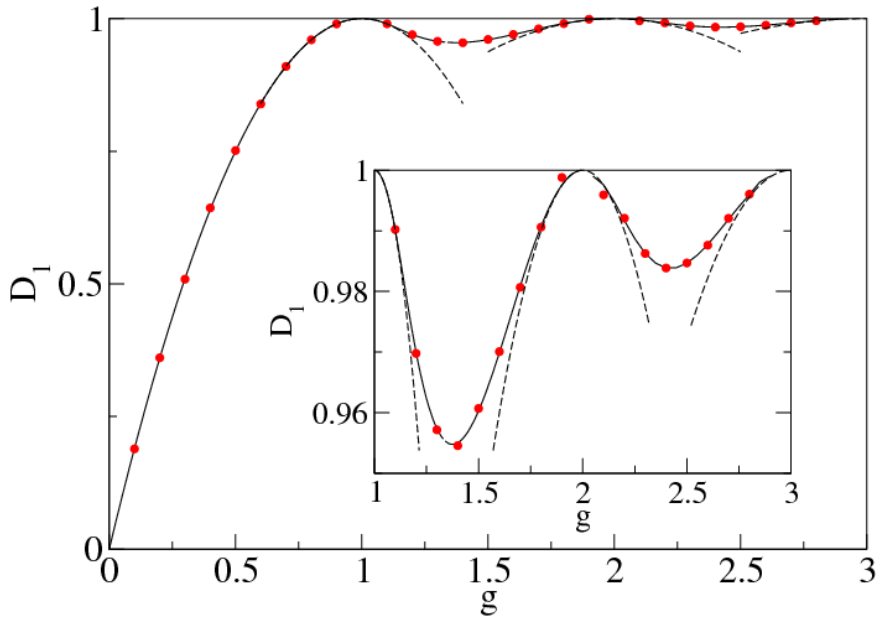

Figure 7.10: D_1 as function of g for the RS model. Circles are numerical results obtained by averaging over all eigenvectors taken from 128 realizations for $N = 2^8$ to 8 realizations for $N = 2^{12}$. Dashed lines indicate the leading perturbation series results (6.37)) for $q = 1$. Solid line is an eye guide corresponding to the theoretical value (4.78)–(4.81), assuming that the conjecture (8.14) holds. Inset: same data zoomed in for $1 < g < 3$.

Chapter 8

Some properties of multifractal wavefunctions

In this chapter we review some features observed in multifractal wavefunctions, and discuss how they apply to our systems.

8.1 Symmetry of the multifractal spectrum

A symmetry law was proposed in [211] for the multifractal spectrum. Recall that $\Delta_q = \tau_q - d(q-1)$ are the anomalous scaling exponents defined in (5.5). Then the symmetry relation

$$\Delta_q = \Delta_{1-q} \tag{8.1}$$

is expected to hold exactly at the critical point. This symmetry mirrors a symmetry relation for the distribution of the normalized local density of states (LDOS)

$$\mathcal{P}(\rho) = \rho^{-3}\mathcal{P}(\rho^{-1}), \tag{8.2}$$

which implies

$$\langle \rho^q \rangle = \langle \rho^{1-q} \rangle \tag{8.3}$$

for the LDOS itself. This symmetry can be derived theoretically in the framework of the nonlinear sigma model [212, 29]. It was observed in the PRBM model (4.11) in [211], in the 3D Anderson model over a large interval of values of q [190], in ultrametric random matrices [14], at the quantum Hall critical point [22], and in simple multifractal cascade models [174]. These models are precisely models that can be treated by a nonlinear sigma model approach in the weak multifractality limit. Note that the symmetry (8.1) was analysed in relation with the Gallavotti-Cohen fluctuation relations in [213], and generalized to other types of critical theories in [29].

Deriving (8.1) with respect to q, we get a symmetry on the exponents $\alpha_q = \tau'_q$ as

$$\alpha_q + \alpha_{1-q} = 2d. \tag{8.4}$$

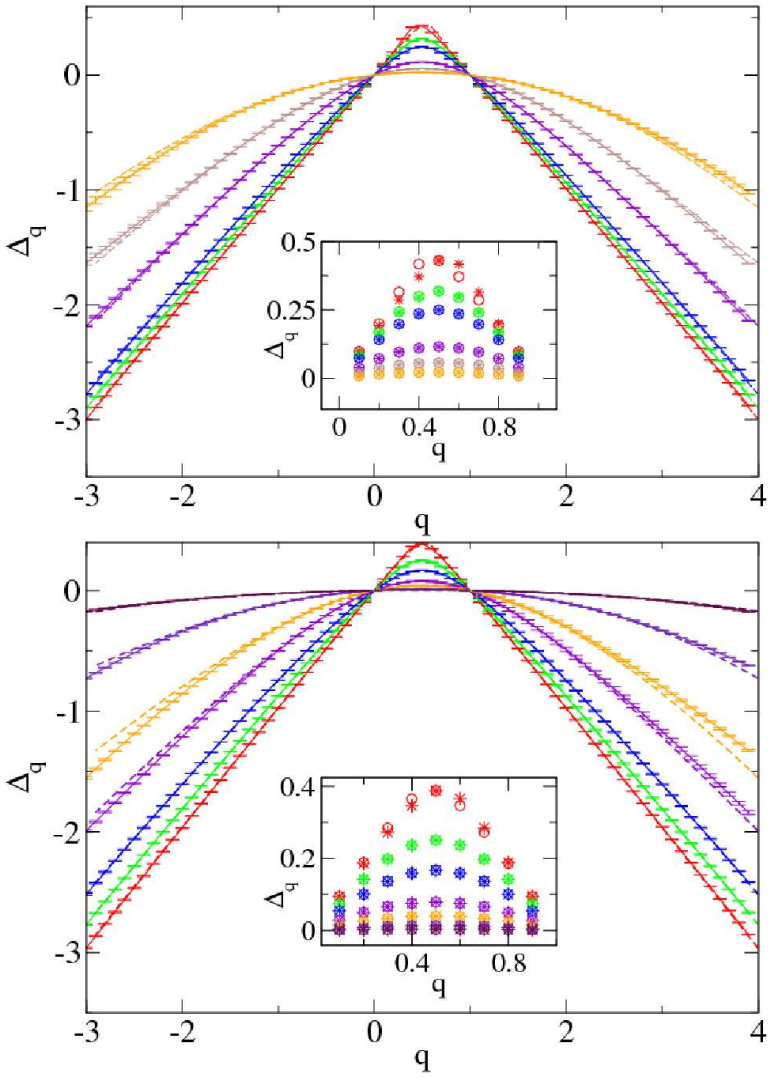

Figure 8.1: Anomalous dimensions Δ_q (solid) and Δ_{1-q} (dashed) as a function of q for CM_r (top) and CM_t (bottom), same data as in Fig. 7.6. The parameter g increases from bottom curve to top curve at $q = 4$. Inset: same data zoomed in, circles correspond to Δ_q, stars to Δ_{1-q}. For almost all data points stars lie inside circles, which indicates symmetry of Δ_q.

This symmetry property reflects in the singularity spectrum. Indeed, by definition of the Legendre transform, α_q is such that $q = f'(\alpha_q)$, and similarly $1-q = f'(\alpha_{1-q})$. Deriving $f(\alpha_{1-q}) - f(\alpha_q)$ with respect to q we thus get

$$f'(\alpha_{1-q})\partial_q\alpha_{1-q} - f'(\alpha_q)\partial_q\alpha_q = -(1-q)\alpha'_{1-q} - q\alpha'_q. \tag{8.5}$$

Deriving (8.4) we get $\alpha'_q = \alpha'_{1-q}$, so that (8.5) reduces to $-\alpha'_q$. Thus,

$$f(\alpha_{1-q}) - f(\alpha_q) = -\alpha_q + \mathrm{cst}. \tag{8.6}$$

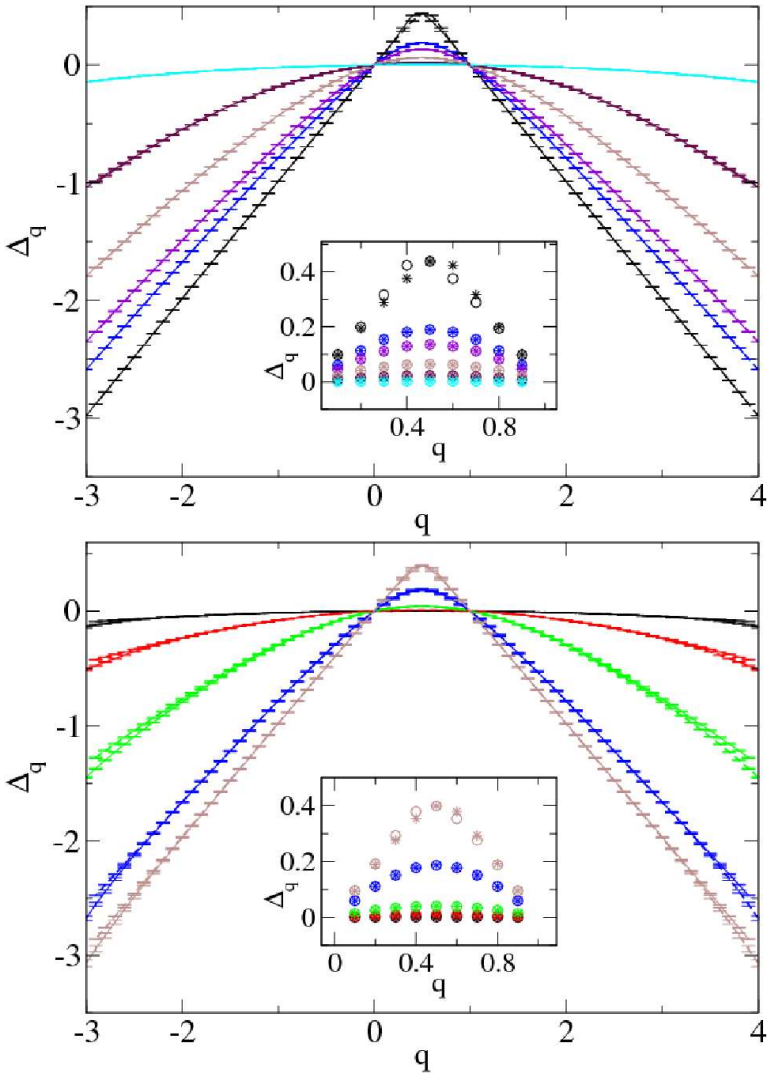

Figure 8.2: Anomalous dimensions Δ_q (solid) and Δ_{1-q} (dashed) as a function of q. Top: RS ensemble, same data as in Fig. 7.9; for better clarity, data corresponding to $a = 0.05$ and 0.1 have been removed. Bottom: PRBM, same data as in Fig. 7.1; for better clarity, data corresponding to $1/g = 30$, 60 and 80 have been removed. g increases from bottom curve to top curve on the right. For RS ensemble, the plot for Δ_{1-q} is almost indistinguishable from the plot for Δ_q. Inset: same data zoomed in, circles correspond to Δ_q, stars to Δ_{1-q}.

The constant can be obtained by using the fact that $f(\alpha_0) = d$ and $f(\alpha_1) = \alpha_1$ (see section 5.1.4), so that finally

$$f(2d - \alpha) - f(\alpha) = d - \alpha. \tag{8.7}$$

Recalling that $\alpha_1 = D_1$ and $\alpha_0 = d - D'_0$, the symmetry (8.4) entails a relation

between the information dimension D_1 and the slope of D_q at the origin, namely

$$D_1 = d + D_0'. \tag{8.8}$$

Another consequence is obtained upon derivation of (8.7) with respect to α, yielding at $\alpha = d$ the value

$$f'(d) = \frac{1}{2}. \tag{8.9}$$

The perturbation-theoretic results (6.2)–(6.3) for strong multifractality show that the symmetry relation is verified at first order of perturbation series for all models where these equations apply. Namely, the anomalous dimensions $\Delta_q = (D_q - 1)(q - 1)$ are given by

$$\Delta_q = (1 - \eta)\frac{\Gamma\left(q - \frac{1}{2}\right)}{\sqrt{\pi}\,\Gamma(q - 1)} - q + 1 \tag{8.10}$$

for $q > 1/2$, and

$$\Delta_q = q + (1 - \eta)\frac{\Gamma(1/2 - q)}{\sqrt{\pi}\,\Gamma(-q)}. \tag{8.11}$$

for $q < 1/2$, which can directly be seen to obey the symmetry (8.1). Similarly, in the weak multifractality regime, D_q is a straight line given by (6.4), which immediately entails the symmetry. Note that the symmetry is not a generic feature of multifractal measures, as it is not verified for instance by models such that the simple multiplicative cascade, where τ_q is given by (5.38).

For the systems considered here, we checked whether the symmetry relation (8.1) is still valid outside the perturbative regime. This is the case for CM models (Fig. 8.1), for RS and PRBM ensembles (Fig. 8.2), but not for the intermediate map (Fig. 8.3). This symmetry relation seems to be verified as soon as there exists a possible perturbation theory approach that leads to formulas of the form of Eqs. (6.2)–(6.3) and (6.4), while it breaks down for the intermediate map (4.26), as illustrated in Fig. 8.3 [OG034]. Similar numerical data are obtained for the non-random map (4.24) (see Fig. 8.3 bottom).

8.2 Multifractality and spectrum: numerical connections

Suppose a matrix M is diagonalised as $M = UDU^\dagger$, with D a diagonal matrix, and U a unitary matrix whose columns are eigenvectors of U. Multifractality is a property that characterizes eigenvectors. Thus, multifractal dimensions are related to matrix U. They depend crucially on the basis in which U is expressed: in the basis of eigenvectors itself, U would just be the identity and have no multifractality property whatsoever. On the other hand, spectral properties only depend on matrix D, and are basis-independent. It is therefore somewhat surprising that connections have been found between multifractal dimensions and spectral properties of multifractal quantum maps.

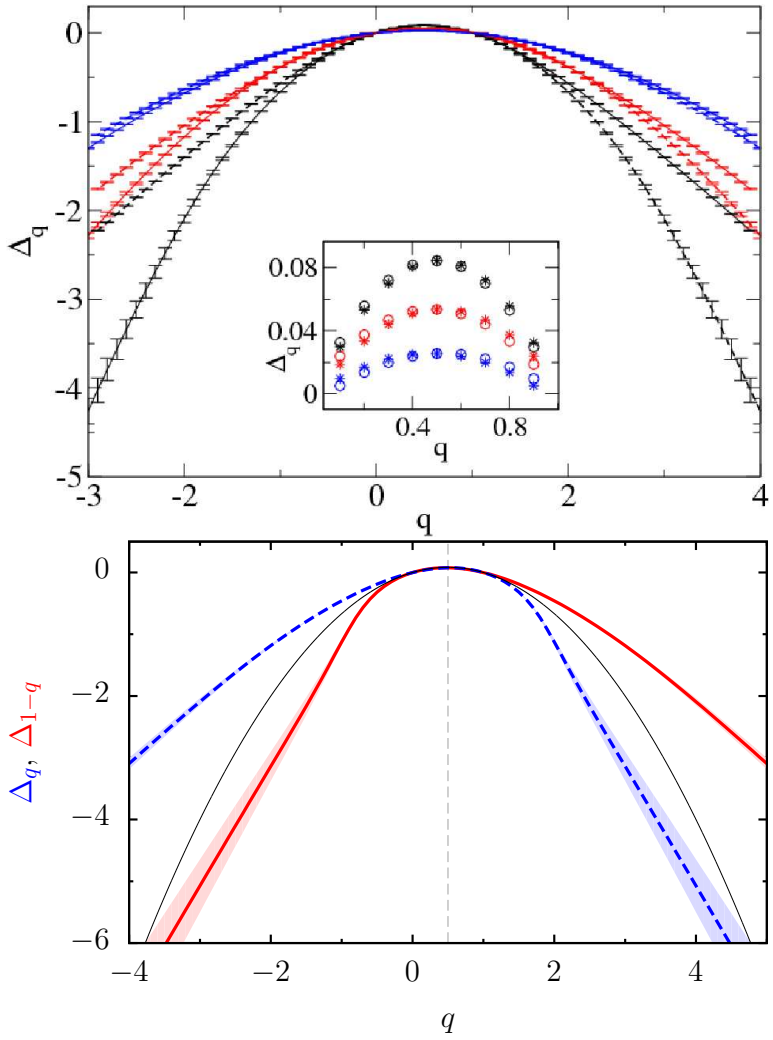

Figure 8.3: Top: Anomalous dimensions Δ_q (solid) and Δ_{1-q} (dashed) as a function of q for the intermediate ensemble (4.26), same data as in Fig. 7.2. Inset: same data zoomed in. Bottom: Anomalous exponents Δ_q (blue dashed curve) and Δ_{1-q} (red solid curve) for eigenvectors of the intermediate map (4.24) with $\gamma = 1/3$ and $N = 2^{14}$. The (light blue, light red) shaded region indicates standard error in the least squares fitting. The multifractal analysis was done with box sizes ranging from 16 to 1024. The black thin line shows the parabola $q(1-q)/b$ corresponding to the linear regime.

Relating the spectral form factor to the return probability $p(t)$ of a quantum wavepacket [214], and using the short-time dependence of the return probability $p(t) \sim t^{-D_2/d}$ [215], it was argued [96] that level compressibility and dimension D_2 should be related by the relation

$$2\chi + \frac{D_2}{d} = 1, \tag{8.12}$$

where d is the dimension of the underlying system. In [OG029] we conjectured the relation

$$\chi + \frac{D_1}{d} = 1, \tag{8.13}$$

which relates the level compressibility to the information dimension rather than the correlation dimension. In the case of one-dimensional systems Eq. (8.13) reduces to the simple relation

$$D_1 = 1 - \chi. \tag{8.14}$$

In the perturbative regimes of weak and strong multifractality, this equation allows to express not only the information dimension D_1 but all D_q as a function of the level compressibility, at least in a certain range of values of q. Indeed, in view of Eqs. (6.2) and (6.4) taken at $q = 1$, Eq. (8.14) implies the identity $\eta = \chi$, so that multifractal dimensions take the form

$$D_q = \begin{cases} \dfrac{\Gamma(q-1/2)}{\sqrt{\pi}\,\Gamma(q)}(1-\chi) & \text{for } 1-\chi \ll 1, \\ 1 - q\chi & \text{for } \chi \ll 1. \end{cases} \tag{8.15}$$

We will now consider various examples in 1, 2, or 3 dimensions. Level compressibility is calculated numerically following the procedure detailed in Section 3.1.

8.2.1 Intermediate map

For the intermediate map (4.26), the spectral compressibility can be inferred from our early result in [OG006]. It is given by Eq. (4.25) and reads $\chi = 1 - 1/b$ for a map parameter $\gamma = a/b$. The values of D_1 and D_2 extracted from the data of Fig. 7.2 are presented in Fig. 8.4. Clearly (8.14) holds for all values of b, while (8.12) breaks down in the strong multifractality regime of small b.

8.2.2 Banded matrices

For PRBM, perturbation series expansion allows to obtain the level correlation function as a correction of the RMT expression. For instance for $\beta = 2$ in the weak multifractality regime it reads [137]

$$R_2^{(c)}(s) = \delta(s) - \frac{\sin^2 \pi s}{\pi^2 s^2} \frac{\pi^2 s^2}{4b^2 \sinh^2\left(\frac{\pi s}{4b}\right)}. \tag{8.16}$$

This in turn gives the level compressibility

$$\chi = \frac{1}{2\pi\beta b}, \qquad b \gg 1. \tag{8.17}$$

For $b \ll 1$ one gets for $\beta = 2$ [137]

$$R_2^{(c)}(s) = \delta(s) - \exp\left(-\frac{s^2}{2\pi b^2}\right), \tag{8.18}$$

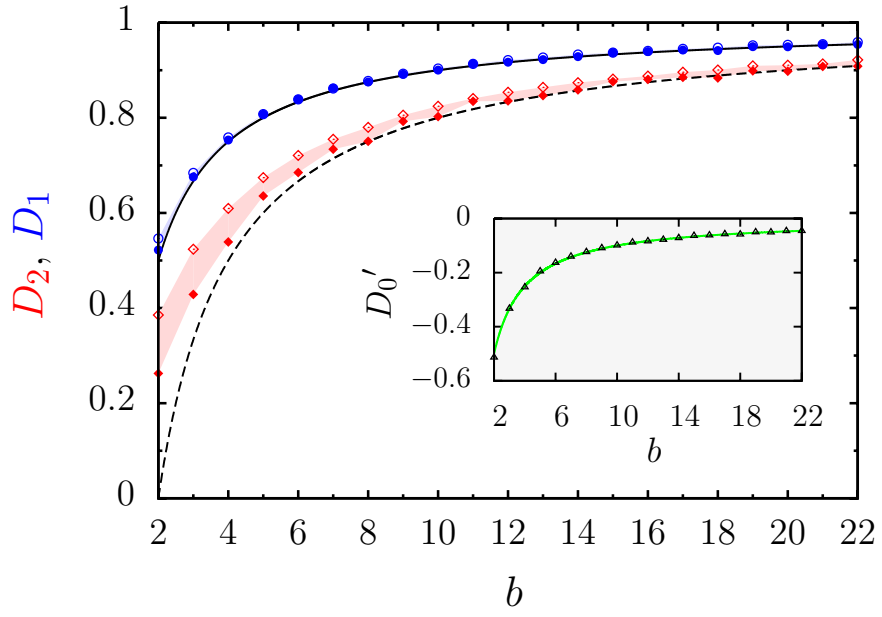

Figure 8.4: Information dimension D_1 (blue circles) and correlation dimension D_2 (red diamonds) as a function of the denominator of $\gamma = 1/b$. Full (empty) symbols are numerical values obtained by the method of moments. Solid and dashed lines are the theoretical curves $1-1/b$ and $1-2/b$ for D_1 and D_2 respectively. The values obtained by e.g. the box counting method lie in the shaded domain in between. Inset: slope of D_q at the origin $q = 0$ (triangles) and curve $-1/b$ (solid line), as predicted from (8.14) and the symmetry (8.8).

and $\chi = 1 - 2\sqrt{2}b$ for $\beta = 1$ (again corrected by a factor $1/\sqrt{2}$ compared to [137] to account for our change of definition), and $\chi = 1 - \pi\sqrt{2}b - 4(2/\sqrt{3} - 1)\pi^2 b^2$ for $\beta = 2$.

Perturbative expansion of the exponents D_2 was obtained up to second order in the band parameter $g \ll 1$ via the supersymmetric virial expansion technique [168, 169]. Again, (8.14) holds. Insets in Fig. 8.5 show that it also holds outside the perturbative regime.

For ultrametric matrices, perturbation series gives the first order of D_1 and χ in the strong multifractality limit. From (7.3) we obtain

$$D_1 = \frac{\pi}{\sqrt{2}\ln 2}\frac{J}{W}. \tag{8.19}$$

In [OG034] we obtained

$$\chi = 1 - \frac{\pi J}{\sqrt{2}\ln 2\, W} \tag{8.20}$$

for the level compressibility, which proves (8.14) in this regime. Figure 8.6 illustrates the validity of (8.14) for other values of J/W.

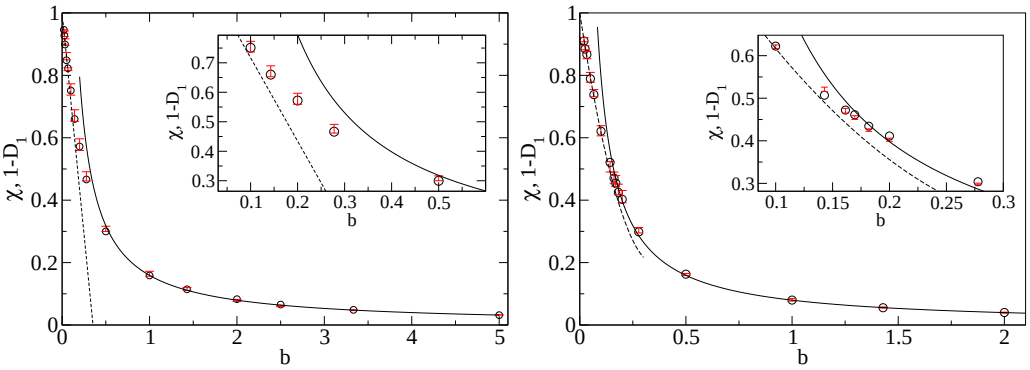

Figure 8.5: χ (black circles) and $1 - D_1$ (red error bars), for PRBM (4.12) with $\beta = 1$ (top) and $\beta = 2$ (bottom).

8.2.3 RS model

From exact expressions (4.78), (4.79), (4.81), it follows that for parameter a in the vicinity of integers $\kappa = 0, \ldots, 3$, one has

$$\chi \longrightarrow \begin{cases} 1 - 2a & |a| \ll 1 \\ \dfrac{(a-\kappa)^2}{\kappa^2} & |a - \kappa| \ll 1 \text{ and } |\kappa| \geq 1. \end{cases} \tag{8.21}$$

From the analytic perturbation theory Eqs. (6.2) and (6.4) one gets $D_1 = 1 - \chi$. Figure (8.7) illustrates this for RS ensemble. The inset clearly shows that the validity of this relation extends outside the perturbative regime.

8.2.4 Higher dimensional conjecture

A standard example of a transition in a two-dimensional critical model is the metal-insulator transition in the quantum Hall effect described by the Chalker-Coddington network model [216]. Various papers have investigated numerically this model. Information dimension D_1 was found to be $D_1 = 1.7405 \pm 0.0004$ in [22], yielding $1 - D_1/2 = 0.1298 \pm 0.0002$. On the other hand, the spectral compressibility for this model was found numerically to be equal to $\chi = 0.124 \pm 0.006$ in [217]. These results are compatible with our conjecture.

The conjecture was also shown to hold in the strong multifractality limit in a two-dimensional version of the PRBM model [218].

For a transition in a three-dimensional critical model, we considered the metal-insulator transition in the 3D Anderson model (4.10) [OG029]. It was found that $D_1 = 1.93 \pm 0.01$ in [26], while earlier computations by the same authors [25] had led to $D_0' = 4.027 \pm 0.016$, which would correspond via the symmetry (8.8) to $D_1 = 1.973 \pm 0.016$, and thus $1 - D_1/3$ about 0.34 to 0.36. On the other hand, the spectral compressibility for the anisotropic Anderson model at the metal-insulator transition was shown to take values ranging from $\chi = 0.28 \pm 0.06$ to $\chi = 0.32 \pm 0.03$ [219] . Again, we stress that numerically computing χ is a subtle issue. Nevertheless the values obtained in the literature are compatible with Eq. (8.14).

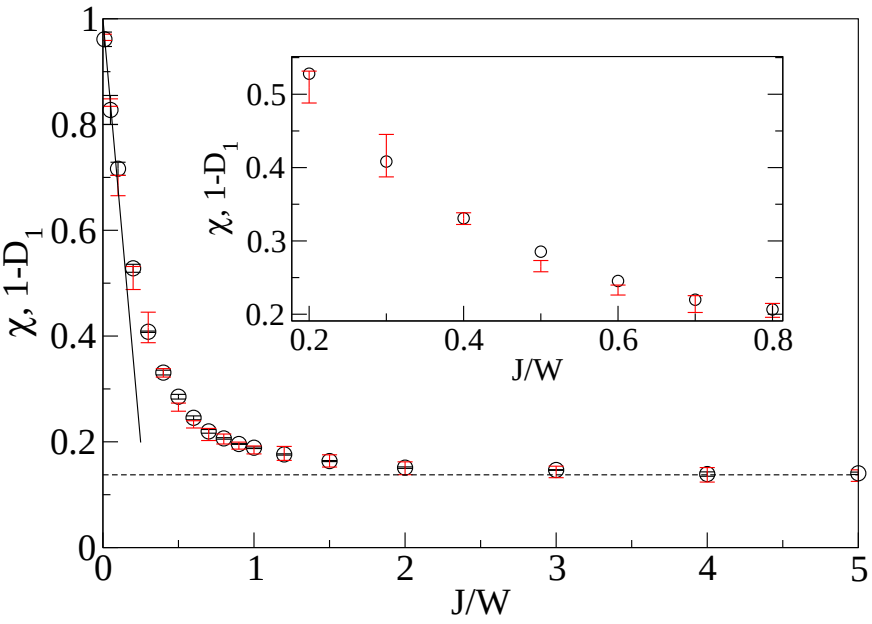

Figure 8.6: χ and $1 - D_1$ for ultrametric matrices. Solid line is the asymptotic theoretical value (8.20). Dashed horizontal line is the numerical value $1 - D_1 \simeq 0.137 \pm 0.008$ obtained for $W = 0$ ($J/W \to \infty$). Inset: same data magnified around $J/W = 0.5$.

8.2.5 Generalizations

Based on a heuristic observation on a scaling $D_q \simeq (1 + 1/(a_q b))^{-1}$ of the multifractal dimensions for the PRBM model, a generalisation of (8.14) was proposed in [13] as

$$D_q \simeq \frac{1-\chi}{1+(q-1)\chi}, \tag{8.22}$$

which translates into the fact that $\frac{qD_q}{1-D_q}$ is independent on q. For PRBM this relation was observed numerically for values of q approximately in the range $0.8 < q < 2.5$. It was checked numerically in [13] (and in [220] for its $q < 1/2$ version based on the symmetry (8.1)) that this relation holds reasonably well for a number of other critical systems, including the intermediate map (4.26) as well as the Ruijsenaars-Schneider and Calogero-Moser models defined above.

The relation (8.12) between D_2 and χ, proposed in [96] and valid in the weak multifractality limit, then appears as a first-order expansion of (8.22) in the limit $\chi \ll 1$.

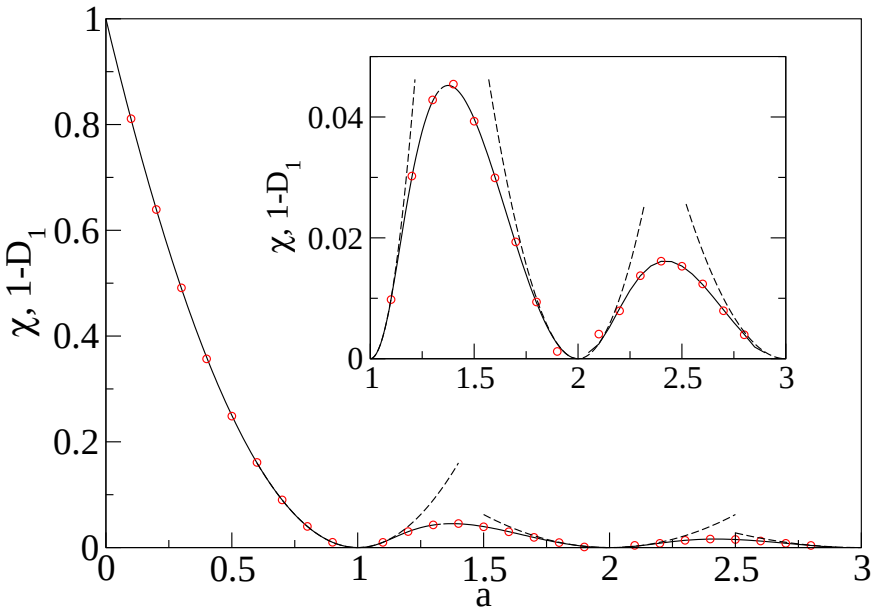

Figure 8.7: χ (solid line) and $1-D_1$ (red circles) for RSE. D_1 is obtained numerically by averaging over all eigenvectors, from 128 realizations for $N = 2^8$ to 8 for $N = 2^{12}$.

8.3 Tail of the moment distribution

A relationship between the exponent x_q governing the tail of the moment distribution (5.37) and multifractal exponents τ_q and $\tau_q^{\rm typ}$ was proposed in [137]. It reads

$$x_q \tau_q^{\rm typ} = \tau_{q x_q}. \tag{8.23}$$

This relationship was analytically proven for the PRBM model (4.11) for integer values of x_q [137], as well as in the strong multifractality limit for $q > 1/2$, using the explicit expressions for x_q and τ_q obtained from the renormalization-group approach.

Equation (8.23) has a few interesting consequences. First, since for $q \geq q_+$ one has $\tau_q^{\rm typ} = q\alpha_+$, (8.23) gives $q x_q \alpha_+ = \tau_{q x_q}$ for $q \geq q_+$. Thus $q x_q$ is given by the intersection of the curve $z \mapsto \tau_z$ and the straight line $z \mapsto z\alpha_+$. Since, as mentioned in Section 5.1.3, τ_q is a concave function, there is a unique intersection point, and so $q x_q$ is a constant quantity. By definition q_+ is such that $x_{q_+} = 1$, so that this constant is equal to q_+. Thus one has

$$x_q = \frac{q}{q_+}, \qquad q \geq q_+. \tag{8.24}$$

The tail exponent also takes a simple expression in the weak multifractality limit where D_q is of the form (6.4). Indeed, in this case, if both q and $q x_q$ belong to the interval $[q_-, q_+]$, the typical and quenched exponents coincide and are given by (6.4). From (8.23) one directly gets $x_q = 1/(q^2\eta)$. Again, applying this relation at $q = q_+$ gives $q_+^2 \eta = 1$ and thus

$$x_q = \left(\frac{q_+}{q}\right)^2, \qquad q \in [q_-, q_+]. \tag{8.25}$$

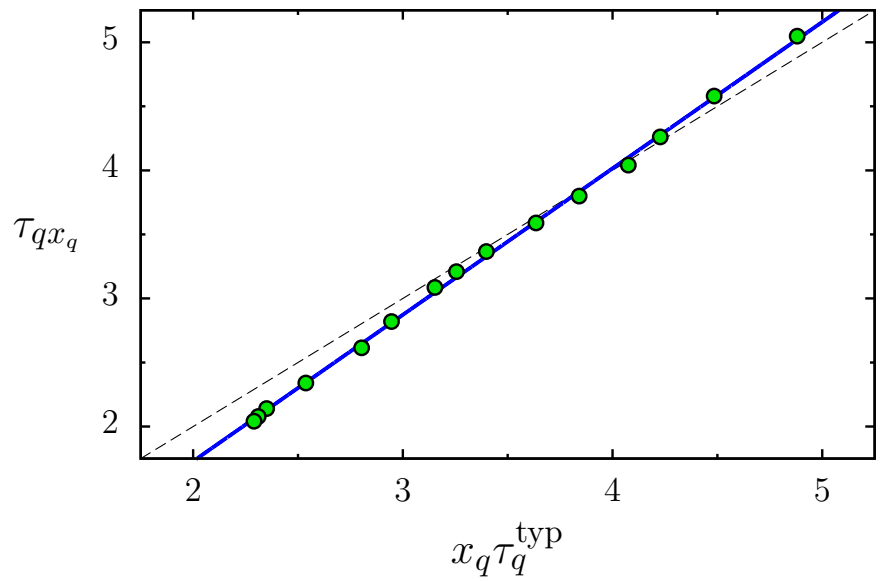

Figure 8.8: Relation between τ_{qx_q} and $x_q\tau_q^{\rm typ}$ for eigenvectors of the intermediate map (4.26) for $\gamma = 1/11$. The blue solid line shows a linear fit of the data ($y = 1.14x - 0.56$). Dashed line is the formula (8.23).

We investigated these relations in [OG027]. For the systems considered here, Eq. (8.23) works reasonably well in the weak multifractality regime, as illustrated in Fig. 8.8 for the intermediate map (4.26). It is not well verified in the limit of strong multifractality [OG027]. In the weak multifractality regime, the relation $q_+^2\eta = 1$ also gives a relation between the predicted separation point q_+ and the slope of D_q at zero or the level compressibility.

For the intermediate map with parameter $\gamma = a/b$, where the level compressibility is given by $1/b$ (see Eq. (4.25)), one would have $q_+ = \sqrt{b}$. For instance, from Fig. 7.3 for parameter $\gamma = 1/11$ we get that $x_q \sim 1$ for $q = 4.3$, while $q_+ = \sqrt{b} \simeq 3.32$. As mentioned earlier, the numerical determination of x_q comes with huge error bars.

8.4 Wave packet multifractality

While previous sections have mainly concentrated on eigenvectors, of primary importance for experiments is the behaviour of quantum wavepackets, as this is directly related to transport properties. As already mentioned in section 8.2, the return probability is governed by the multifractal dimension D_2. At time t it scales as $p(t) \sim t^{-D_2/d}$ [215, 221]. More generally, scaling relations for moments of the wavepackets were given in [222]. Experimental realizations of the quasi-periodic kicked rotor on cold atoms were based on the investigation of spreading properties of atomic wavepackets (see e.g. [34] or [36]).

Our results for multifractal dimensions of wave packet iterates for the kicked version (4.22) of the Anderson map, obtained in [OG027], are presented in Figs. 8.9

and 8.10.

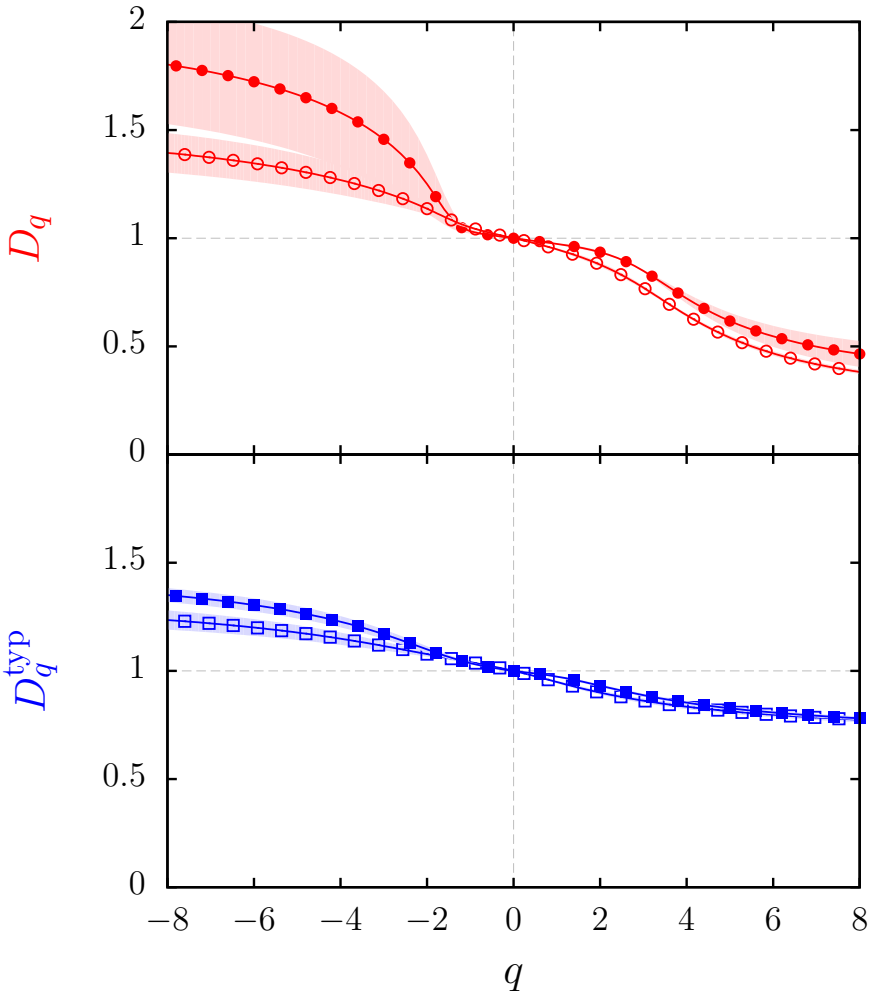

Figure 8.9: Multifractal exponents D_q and $D_q^{\rm typ}$ for iterates of the Anderson map with $k = 1.81$, $N = 2^{11}$. Empty/filled red circles correspond to the method of moments/wavelets. The (light blue, light red) shaded regions indicate standard error in the least squares fitting. The multifractal analysis was done over 1302 realizations of size $N = 2^{11}$ with box sizes ranging from 4 to 512 and scales ranging from $2-9$ to $2-4$.

In [OG035], we investigated multifractal properties of quantum wave packets for the Ruijsenaars-Schneider model (4.85). It was shown that for a state initially localized in the momentum representation at $P = P_0$, the average wave packet after time t was given for $P \neq P_0 - kt$ by

$$\langle |\Psi_P^{(t)}|^2 \rangle = \frac{\epsilon^2 \pi^2 t}{N^2} \frac{1}{\sin^2 \frac{\pi}{N}(P - P_0 + kt)}. \tag{8.26}$$

Multifractality of individual wave packets correspond to fluctuations under this envelope. Corresponding multifractal dimensions were shown to saturate for $t \to \infty$

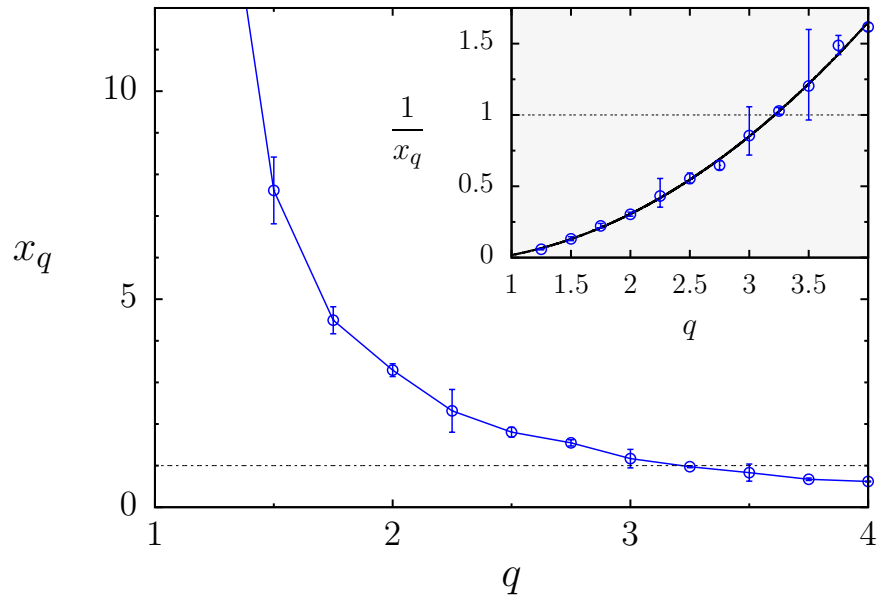

Figure 8.10: Tail exponents x_q for iterates of the Anderson map. Same parameters as in Fig. 8.9. The inset shows that $1/x_q$ is well-fitted by a parabola.

to a finite value smaller than that of eigenvectors.

Chapter 9

Quantum information

We now turn to a slightly different matter, which will nevertheless be considered in connection with the various topics mentioned so far. A first line of research which I have followed in the field of quantum information has been the search for efficient quantum algorithms simulating physical systems. This idea, originally suggested by Feynman in 1982, had been investigated at a theoretical level in various contexts, for instance many-body quantum systems [223] or classical chaotic systems [224]. This has led to proposals for the implementation of the evolution of simple quantum maps on a quantum computer. Efficient algorithms were proposed to simulate a number of the standard toy models of quantum chaos introduced in Chapter 4, such as the quantum baker map [122] or the kicked rotor [225]. Some results we obtained are reported in Section 9.1.

A natural question in this context is the evolution of entanglement under quantum maps. Indeed, one of the origins of the power of quantum computation rests in the high degree of entanglement of the quantum states which are manipulated. It turns out that the average entanglement of random pure states is nearly maximal [226, 227, 228]; our contributions on this point will be discussed in Section 9.2. It has been suggested that a way to efficiently generate highly entangled state would be to apply iterations of quantum maps. This naturally raises the question of the entangling properties of chaotic quantum maps. According to the conjectures of quantum chaos, one may expect the entanglement obtained by iteration of chaotic quantum maps to be comparable to the entanglement of column vectors of random matrices. By contrast, the entangling power of quantum maps with integrable underlying dynamics should be much weaker. Of primary interest for our work will be of course the question of the entangling power of intermediate maps. This question leads to expliciting connections between entanglement and localization, as we will show in Section 9.3.

9.1 Quantum algorithms

Given the lack of efficient quantum algorithms proposed in the literature, one of my lines of research has been to construct and propose some algorithms implementing the quantum simulation of systems of physical origin. In [OG009] we proposed an

algorithm simulating the evolution of a wavepacket on a smallworld network. Later on, we explored the efficiency of the quantum simulation of the semiclassical trace formulas, which relate semiclassical pseudo-eigenvalues of the evolution operator in a quantum system to periodic orbits of the corresponding classical map. Our results [OG016] show that a polynomial improvement can be achieved over classical algorithms. Other types of quantum algorithms we proposed were algorithms finding the equilibrium distribution for classical statistical mechanics systems [OG026].

Most known algorithms are based on the use of the quantum Fourier transform. When it is used in a quantum algorithm, the corresponding step is exponentially faster than the classical Fast Fourier Transform, due to the parallel nature of quantum operations. This is not the only transform that can be programmed efficiently. We showed that the wavelet transform described in Section 5.3.3 can similarly be implemented efficiently on a quantum computer. Inspired by our work on multifractality, we proposed a quantum algorithm that uses a quantum version of the wavelet transform in order to extract efficiently multifractal properties of a quantum wavefunction [OG019]. This opens the way to a new class of algorithms based on methods different from the usual ones.

9.2 Entanglement of random states

9.2.1 Definitions

One of the goals of quantum information theory is to analyse the various resources that quantum systems provide. In the past decade, many works have been dedicated to the study of entanglement in quantum systems and its characterization. In particular, the problem of defining a satisfactory entanglement measure is a difficult issue which is still open. Of particular interest in quantum information is the entanglement properties of random quantum states, as such states appear in many quantum algorithms and communication protocols, such as superdense coding or long-distance preparation of quantum states. For complex systems with chaotic properties, these states appear naturally as good models for eigenstates. Quantifying entanglement for such states is thus a crucial question.

A number of entanglement measures have been proposed in order to quantify entanglement, based either on quantum information theory or on thermodynamical considerations: entanglement of formation and distillable entanglement [229], relative entropy [230, 231, 232], n-tangle [233], concurrence [234] (see e.g. the review [235]). These measures, which may be complicated in the case of mixed states or when it comes to measuring multipartite entanglement, all take a very simple expression in the case of pure states and for bipartite entanglement, which measures entanglement in a bipartite system composed of two coupled Hilbert spaces (for instance, qubits and environment). In this simple case, it is measured by the Von Neumann entropy of the reduced density matrix obtained by tracing over one subsystem [236]. More specifically, if $\rho_A = \mathrm{tr}_B|\psi\rangle\langle\psi|$ is the density matrix obtained by tracing out subsystem B, then the entropy of entanglement of the state ψ with respect to the bipartition (A, B) is the von Neumann entropy of ρ_A, that is $S = -\mathrm{tr}(\rho_A \ln \rho_A)$.

Let Ψ be a pure state belonging to a Hilbert space $\mathcal{H}_A \otimes \mathcal{H}_B$, where $\mathcal{H}_A$ and $\mathcal{H}_B$ are spanned respectively by $\{|a_i\rangle\}_{1\leq i\leq N}$ and $\{|b_i\rangle\}_{1\leq i\leq M}$. We assume that $N \leq M$. Let x_i be the Schmidt coefficients for Ψ, that is, the state Ψ has a Schmidt decomposition (see e.g. [237])

$$|\Psi\rangle = \sum_{i=1}^{N} \sqrt{x_i}|a_i\rangle \otimes |b_i\rangle. \tag{9.1}$$

In this basis the reduced density matrix ρ_A is an $N \times N$ diagonal matrix with entries x_i. The entropy of entanglement, or Von Neumann entropy, is the Shannon entropy of the x_i,

$$S = -\sum_{i=1}^{N} x_i \ln x_i. \tag{9.2}$$

For states that can be factorized between the two Hilbert spaces (unentangled states), it takes the value 0. For maximally entangled states where all $x_i = 1/N$ it takes the maximal value $\ln N$. For bipartite pure states, the entanglement entropy can be proved to be a unique entanglement measure [238, 239]. More conveniently for analytic purposes, one often uses a linearized version of it. Let

$$R = \sum_{i=1}^{N} x_i^2 \tag{9.3}$$

be the purity of a state Ψ. The linear entropy τ is the first-order term in the expansion of the von Neumann entropy around its maximum. It is expressed in terms of the purity by the simple relation

$$\tau = \frac{N}{N-1}\left(1 - R\right), \tag{9.4}$$

where the scaling factor is such that τ varies in $[0, 1]$. A generalization of the Von Neumann entropy is given by the Renyi entropy

$$R_q = \frac{1}{1-q} \ln \left(\sum_{i=1}^{N} x_i^q \right). \tag{9.5}$$

For $q \to 1$ one recovers the Von Neumann entropy.

In the case of multipartite pure states, one can generalize this measure by considering the average purity between one qubit and all others. This is the so-called Meyer-Wallach entanglement [240]. Namely, for a pure state Ψ, the one-qubit reduced density matrix ρ_A is a 2×2 matrix whose eigenvalues x_1 and x_2 are the Schmidt coefficients of the state. They are roots of the characteristic polynomial $X^2 - X + \det \rho_A$, so that the linear entropy (9.4) is given by

$$\tau = 2(1 - \mathrm{tr}\rho_A^2) = 4 \det \rho_A. \tag{9.6}$$

In the case of 2 qubits this quantity is called the *tangle* and corresponds to the square of the generalized concurrence [241]. Since $\mathrm{tr}\rho_A = 1$, one has $\tau \in [0, 1]$. The

entanglement entropy (9.2) of one qubit with the $n-1$ others can then be written

$$S = h\left(\frac{1+\sqrt{1-\tau}}{2}\right), \qquad \text{with} \quad h(x) = -x\ln x - (1-x)\ln(1-x). \tag{9.7}$$

The Meyer-Wallach entanglement can then be defined as the mean value of τ averaged over all $(1, n-1)$ bipartitions. It can be alternatively written as

$$\langle\tau\rangle = \frac{4}{n}\sum_{r=0}^{n-1} G(u^r, v^r), \tag{9.8}$$

where $G(u,v) = \langle u|u\rangle\langle v|v\rangle - |\langle u|v\rangle|^2$ is the Gram determinant of u and v, and u^r (resp. v^r) is the vector of length $N/2$ whose components are the Ψ_i such that i has no (resp. has a) term 2^r in its binary decomposition. Vectors u^r and v^r are therefore a partition of vector Ψ in two subvectors according to the value of the r-th bit of the index. A more general (but less tractable) quantity can be defined for other bipartitions $(\nu, n-\nu)$, where ν is any number between 1 and $n-1$.

9.2.2 Entanglement of random states

In order to be able to assess entangling properties of quantum maps, one should first be able to make predictions, as a reference, in the simplest framework of Random Matrix Theory. Starting from a localized state (which is usually the case in the computational basis for a quantum algorithm), one iteration of a map modeled by a random matrix leads to a column vector of that matrix. Random pure states thus allow to access typical properties of quantum states. Such states can be seen as column vectors of random unitary matrices drawn from an ensemble with unitarily invariant Haar measure [72]. Equivalently they can be realized as vectors with coefficients given by independent random complex Gaussian variables, rescaled to have a norm equal to 1 (see e.g. [242]). Numerically they can be obtained by Hurwitz parametrization of random states [243].

One of the earliest analytical results on the entanglement properties of random pure states is the average von Neumann entropy (9.2) at finite M and N, which reads [228, 244]

$$\langle S\rangle = \sum_{k=N+1}^{MN} \frac{1}{k} - \frac{M-1}{2N}. \tag{9.9}$$

For multipartite entanglement, an expression for the mean Meyer-Wallach entanglement for non-localized CUE vectors of length N was given in [226]. It reads

$$\langle\tau\rangle = \frac{N-2}{N+1}. \tag{9.10}$$

Maximally multipartite entangled states were investigated in [245]. Other analytical results include expressions for the second and third moments of the purity [246, 123], the average value for each Schmidt coefficient of a random pure state [247], or the distribution of G-concurrence [248]. For mixed states, statistical properties of entanglement measures for random density matrices were obtained in [249]–[250].

In the large M and N limit with M/N fixed, the probability distribution of Renyi entropy was calculated using a Coulomb gas method [57]. For any fixed $q > 1$ the distribution was obtained by saddle-point approximation of the integral over all eigenvalue distributions with fixed entropy. It was shown that this distribution can be divided into three separate regimes, according to the shape of the density of eigenvalues which dominates at large N. In particular, although the mean value (9.9) of the entropy is asymptotically close to $\ln N$, the probability to actually achieve the maximal value rapidly decreases with N. Other large–N results were obtained, such as properties of the Laplace transform of the purity distribution, allowing to calculate asymptotic expressions for cumulants [58]. Nevertheless, there was no known expression for finite-size matrices, apart from the trivial cases.

For random pure states obtained as column vector of random matrices distributed according to the unitarily invariant Haar measure (CUE matrices), the Schmidt coefficients are characterized by the following joint distribution [227, 123, 242]:

$$P(x_1, \ldots, x_N) = \mathcal{A} \prod_{1 \leq i < j \leq N} (x_i - x_j)^2 \prod_{1 \leq i \leq N} x_i^{M-N} \, \delta\left(1 - \sum_{i=1}^{N} x_i\right) \tag{9.11}$$

for $x_i \in [0, 1]$; δ is the Dirac delta function, and $\mathcal{A}$ is the normalisation factor

$$\mathcal{A} = \frac{(NM-1)!}{\prod_{0 \leq j \leq N-1} (M-j-1)!(N-j)!}. \tag{9.12}$$

In the case $N = 2$, the analytic expression for the probability distribution $P(R)\, dR$ can easily be obtained analytically directly from (9.3)–(9.11), and reads

$$P(R) = \frac{(2M-1)!}{2^{M-1}(M-1)!(M-2)!} (1-R)^{M-2} \sqrt{2R-1} \tag{9.13}$$

for $1/2 \leq R \leq 1$, 0 otherwise (A is the normalization factor). Calculations are much more involved for $N > 2$. For $M = N = 3$, we found in [OG013] that

$$P(R) = 70\sqrt{3} \left| \begin{array}{ll} 2\pi \left(R - \frac{1}{3}\right)^3, & \frac{1}{3} \leq R \leq \frac{1}{2} \\ 6\left(R - \frac{1}{3}\right)^3 \left(\frac{\pi}{3} - \arccos \frac{1}{\sqrt{6R-2}}\right) & \\ \quad + (R-1)(R - \frac{5}{9})\sqrt{6R-3}, & \frac{1}{2} \leq R \leq 1. \end{array} \right. \tag{9.14}$$

We also gave analytic expressions for $3 \times M$ and $4 \times M$ systems in [OG013].

For $N \geq 4$, we calculated in [OG011] the nth moments of the purity, obtaining the closed expression

$$\begin{aligned} \langle R^n \rangle = & \frac{(NM-1)!}{(NM+2n-1)!} \sum_{n_1+n_2+\cdots+n_N=n} \frac{n!}{n_1! n_2! \ldots n_N!} \\ & \times \prod_{i=1}^{N} \frac{(M+2n_i-i)!}{(M-i)!i!} \prod_{1 \leq i < j \leq N} (2n_i - i - 2n_j + j). \end{aligned} \tag{9.15}$$

From Equation (9.15) one can get the expressions for the cumulants of the distribution $P(R)$. Since the probability distribution $P(R)$ is defined over a bounded interval

(R is bounded), the knowledge of all moments determines uniquely the probability distribution [161]. In particular, the asymptotic expansion of the distribution $P(R)$ can be expressed (see [251] and references therein) by Edgeworth expansion as a function of the normal distribution $Z(x) = \exp(-x^2/2)/\sqrt{2\pi}$ and the cumulants of $P(R)$.

The expressions (9.15) can be extended to the calculation of moments of the Meyer-Wallach entanglement, as we showed in [OG011].

9.3 Entangling power of quantum maps and relationship with localization

One of the byproducts of the investigation of quantum algorithms which could simulate the quantum evolution of complex systems (see Section 9.1) was the study of the entangling properties of chaotic quantum maps. Such studies include for instance entanglement generation in coupled standard maps [252], in Baker's map [253] or in kicked tops [254], or entanglement growth under random unitary evolution [255]. Bounds in entanglement production were explained by RMT in [256].

Meyer-Wallach entanglement was used e.g. to quantify entanglement generation for pseudo-random operators [257] or intermediate or chaotic quantum maps [253, 258]. In [OG010], we investigated entanglement generation for intermediate quantum maps, showing that it differs from usual chaotic systems.

There is in fact a direct connection between entanglement and localization properties. From the definition of the Renyi entropy R_q (9.5) and the definition of multifractal dimensions D_q, Eqs. (5.13)–(5.15), it clearly appears that for large N the Renyi entropy exactly coincides with the multifractal dimension of the quantum states (9.1). Similarly, the Von Neumann entropy (9.2) exactly corresponds to the information dimension of (9.1), given by (5.16), while the purity (9.3) is precisely the inverse participation ratio of (9.1). This enables to connect entanglement (as measured by the purity) to localization properties of quantum states. It was shown that entanglement measures reflect the localization-delocalization transition of electronic states in the tight-binding model on a smallworld networks [259], in the PRBM model [260], in the 3D Anderson model and in the integer quantum Hall transition [261]. While these latter studies consider entanglement between lattice sites, in [OG012] and [OG018] we investigated the links between multifractal dimensions of quantum states and entanglement between qubits in a quantum simulation of such systems.

There are various situations (presence of a symmetry, study of the subpart of a quantum algorithm) in which one is interested only in the spreading of a quantum state inside a subpart of the Hilbert space. This is typically the case in the regime of Anderson localization. In [OG012] we studied the mean Meyer-Wallach entanglement of random but localized states and obtained an explicit analytic relation between localization and entanglement measures. Namely, we considered states $|\Psi\rangle$ of length $N = 2^n$ with $M \leq N$ nonzero components. Its Inverse Participation Ratio

(IPR) is defined as

$$\xi = \sum_i |\Psi_i|^2 / \sum_i |\Psi_i|^4. \tag{9.16}$$

For each partition of $|\Psi\rangle$ into two vectors $|u\rangle$ and $|v\rangle$ of length $N/2$, we introduced the correlators

$$C_{xx} = \frac{1}{2}\left(\langle |u_i|^2 |u_j|^2\rangle + \langle |v_i|^2 |v_j|^2\rangle\right) \tag{9.17}$$

$$C_{xy} = \langle |u_i|^2 |v_j|^2\rangle, \tag{9.18}$$

where the average is taken over all n partitions of $|\Psi\rangle$ into two vectors $|u\rangle$ and $|v\rangle$ of length $N/2$, and over all $i, j \in \{1, ..., N/2\}$ with $i \neq j$ (for C_{xx}) and all $i, j \in \{1, ..., N/2\}$ (for C_{xy}). Thus C_{xx} quantifies the internal correlations inside u and v, and C_{xy} the cross correlations between u and v. Normalization of $|\Psi\rangle$ imposes that

$$\langle 1/\xi\rangle + N(N/2-1)\langle C_{xx}\rangle + (N^2/2)\langle C_{xy}\rangle = 1, \tag{9.19}$$

Using (9.8) we get $\langle\tau\rangle = N(N-2)\langle C_{xy}\rangle$. Under the condition of uncorrelated vector components, we have $C_{xx} = C_{xy}$, which, by the normalization condition (9.19), entails

$$\langle\tau\rangle = \frac{N-2}{N-1}\left(1 - \left\langle\frac{1}{\xi}\right\rangle\right). \tag{9.20}$$

A similar result with different assumptions, relating $\langle\tau\rangle$ to the IPR, was found the same year in [262].

As an example, for a CUE vector in a N-dimensional Hilbert space, localized on M basis vectors, the IPR is $\xi = (M+1)/2$, and (9.20) gives

$$\langle\tau\rangle = \frac{M-1}{M+1}\frac{N-2}{N-1}. \tag{9.21}$$

In the more general case of other bipartitions $(\nu, n-\nu)$, the generalization of Eq. (9.20) reads

$$\langle S\rangle \approx \nu \ln 2 - \frac{2^\nu - 1}{2}\left(1 - \frac{N-2^\nu}{N-1}\left\langle\frac{1}{\xi}\right\rangle\right). \tag{9.22}$$

As mentioned, τ is the first-order term of the expansion of the von Neumann entropy around its maximum. For a $(1, n-1)$ bipartition, the maximum is achieved at $\tau = 1$. From (9.7), the series expansion in powers of $(1-\tau)$ of S reads

$$S = \ln 2 - \sum_{k=1}^{\infty} \frac{(1-\tau)^k}{2k(2k-1)}. \tag{9.23}$$

It is possible to calculate by similar methods all higher-order terms in this expansion as a function of the mean moments Z_q of the wavefunction, given by (5.13), and their powers [OG018]. For example, we get

$$\begin{aligned}\langle\tau^2\rangle &= N(N-2)(N^2-6N+16)c_{1111} \\ &\quad +4N(N-2)(N-4)c_{211} + 4N(N-2)c_{22}\end{aligned} \tag{9.24}$$

with

$$\begin{aligned} c_{22} &= \frac{\langle Z_2^2\rangle - \langle Z_4\rangle}{N(N-1)},\ c_{211} = \frac{\langle Z_2\rangle - \langle Z_2^2\rangle - 2\langle Z_3\rangle + 2\langle Z_4\rangle}{N(N-1)(N-2)}, \\ c_{1111} &= \frac{1 - 6\langle Z_2\rangle + 8\langle Z_3\rangle + 3\langle Z_2^2\rangle - 6\langle Z_4\rangle}{N(N-1)(N-2)(N-3)}, \end{aligned} \tag{9.25}$$

which relates the second order of the entropy of entanglement to moments up to order 4 of the vector. In particular, this indicates that at each order the behavior of the entanglement is governed by the set of multifractal exponents. In the case of a CUE random vector of size N, formulas get simpler; in particular, it is possible to resum the whole series (9.23), which yields

$$\langle S\rangle = \sum_{k=N/2+1}^{N-1} \frac{1}{k}. \tag{9.26}$$

This coincides, as it should, with the expression (9.9) in the case of Hilbert spaces of size respectively $N/2$ and 2. Higher-order terms can be obtained also for the $(\nu, n-\nu)$ bipartitions by expanding the entropy $S = -\mathrm{tr}(\rho_A \log_2 \rho_A)$ around the maximally mixed state $\rho_0 = \mathbf{1}/2^\nu$, as

$$S = \nu \ln 2 + \sum_{n=1}^{\infty} \frac{(-2^\nu)^n}{n(n+1)} \mathrm{tr}((\rho_A - \rho_0)^{n+1}), \tag{9.27}$$

and the traces can be evaluated as sums over correlators of higher moments [OG018].

These formulas correspond to random vectors whose components are distributed over a randomly chosen subset of basis vectors. More physically relevant is the situation where vectors are localized preferentially on a particular subspace of Hilbert space, for instance on M computational basis states which are adjacent (that is, which follow each other in lexicographic order). Such a subspace is spanned by vectors of the form $|c\rangle$,...,$|c+M-1\rangle$, $0 \le c \le 2^n - 1$. In this case we showed in [OG012] that for $M \le N/2$

$$\begin{aligned} \langle\tau\rangle &= \left[\left(\frac{M-2}{M-1} r_0 + \frac{2(2^{r_0}-1)}{M(M-1)} + \frac{4}{3}\frac{(M+1)(2^n - 2^{r_0})}{2^{n+r_0}}\right.\right. \\ &- \left.\left. \frac{1}{M(M-1)} \sum_{r=0}^{r_0-1} \chi_r(m_r)\right)\left(1 - \langle\frac{1}{\xi}\rangle\right)\right]\frac{1}{n}, \end{aligned} \tag{9.28}$$

where $\chi_r(x) = \chi_r(2^{r+1} - x) = x^2 - \frac{2}{3}x(x^2-1)/2^r$ for $0 \le x \le 2^r$. For $M = 2^{r_0}$, $r_0 < n$, this reduces to

$$\langle\tau\rangle = \left[\left(\frac{(r_0 + \frac{4}{3})M^2 - 2(r_0-1)M - \frac{10}{3}}{M(M-1)} - \frac{4(M+1)}{3N}\right)\left(1 - \langle\frac{1}{\xi}\rangle\right)\right]\frac{1}{n}. \tag{9.29}$$

Numerically, this expression is in fact a very good approximation to Eq. (9.28) for all M if we set $r_0 = \log_2 M$.

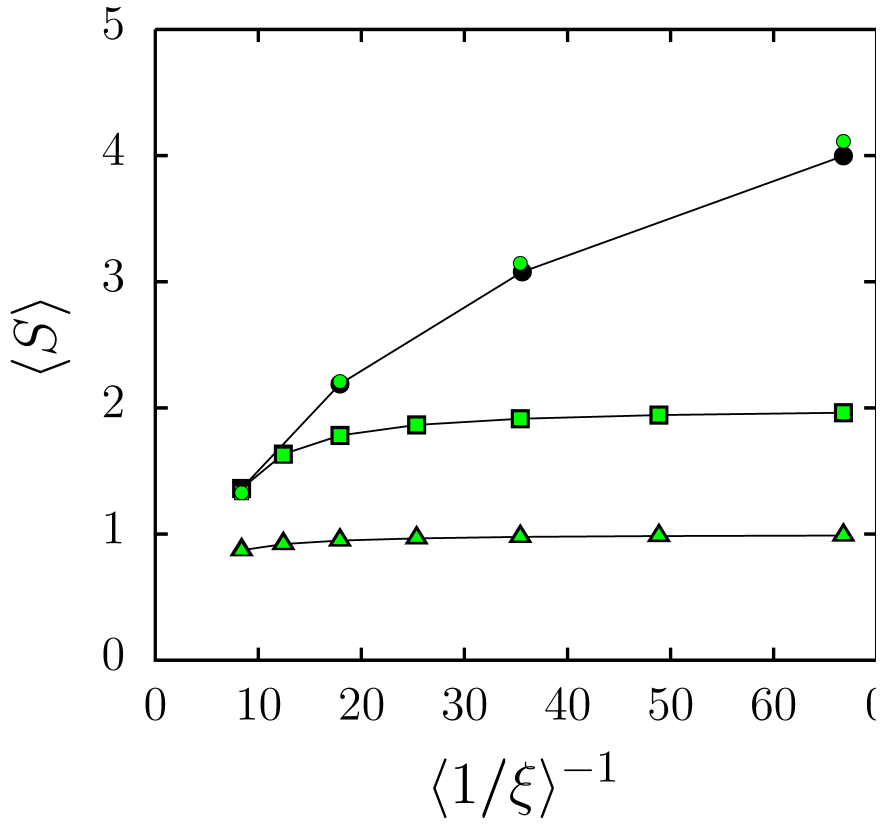

Figure 9.1: Mean entropy of entanglement S for different bipartitions $(\nu, n-\nu)$ as a function of the mean IPR for eigenvectors of (4.26) with $\gamma = 1/3$; the average is taken over 10^6 eigenvectors. Black symbols are the theoretical predictions for the mean value of S obtained from Eq. (9.22) and green symbols are the computed mean values of the von Neumann entropy.

These theoretical formulas were checked on various types of physical systems. Figure (9.1) displays the mean entanglement entropy for eigenvectors of the intermediate map (4.26) with randomly shuffled components, compared with the first order expression (9.22).

As an illustration of the second situation where eigenvector entries are adjacent, we considered the one-dimensional Anderson map (4.10) with $V = 1$ and ϵ_i Gaussian random variables with variance w^2. It has been shown that it can be efficiently simulated on a n-qubit quantum computer [263]. Vectors $|\Psi\rangle$ describe the particle wavefunction in the position representation. Because of localization in one dimension, these wavefunctions have an envelope of the form $\exp(-x/l)$, where l is the localization length. We checked that N-dimensional CUE vectors multiplied by such an exponential envelope have a mean Meyer-Wallach entanglement $\langle Q \rangle$ which is in excellent agreement with (9.28) with $\xi = l$ and $M = 2\xi$ (this corresponds to stars in the inset of Fig. 9.2). The main panel in Fig. (9.2) displays the mean Meyer-Wallach entanglement $\langle Q \rangle$ as a function of the number n of qubits for various strengths of

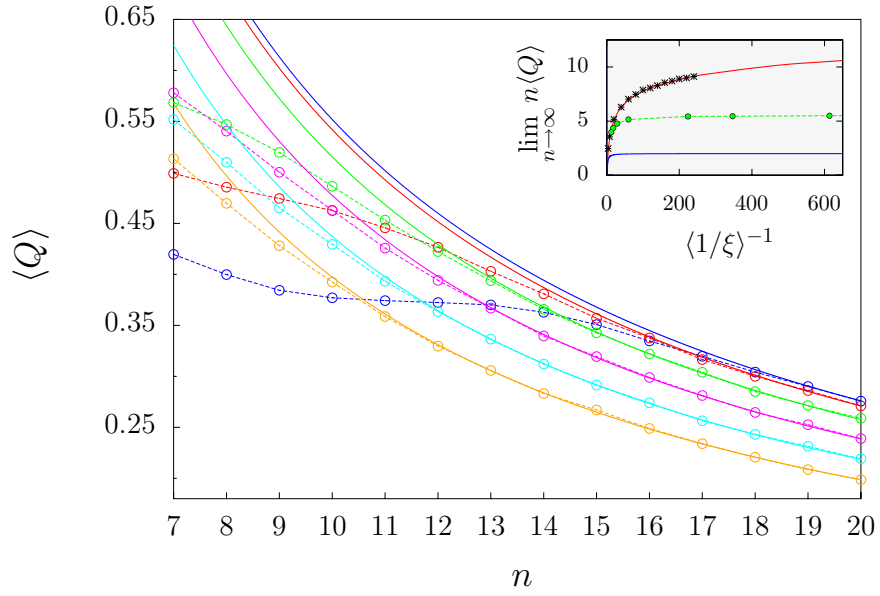

Figure 9.2: (Color online) Mean Meyer-Wallach entanglement vs the number of qubits for 1D Anderson model with disorder from top to bottom $w = 0.2$ (blue), 0.5 (red), 1.0 (green), 1.5 (magenta), 2.0 (cyan), and 2.5 (orange). Average is over 10 central eigenstates for 1000 disorder realizations. Solid lines are the C/n fits of the tails. Inset: Value of $C = \lim_{n\to\infty} n\langle Q\rangle$ as a function of IPR ξ (green dots) for the values of w above and $w = 0.4$, together with analytical result from Eq. (9.28) (red line, top) and from Eq. (9.30) (blue line, bottom) both for $M = 2\xi$. Stars are the C values resulting from a C/n fit of the numerical data for CUE vectors of size N with exponential envelope $\exp(-x/l)$.

the disorder w. While the decrease in $1/n$ is perfectly reproduced, the dependence in ξ does not correspond to the one expected from (9.28). This discrepancy can be accounted for by the oscillating nature of localized eigenvectors for weak disorder. For oscillating vectors of the form $\Psi_j = \cos \pi j/2$, $c + 1 \leq j \leq c + M$, and zero elsewhere, the mean Meyer-Wallach entanglement is given (after averaging over c) by

$$\langle \tau \rangle = \left(\frac{26}{9} - \frac{4}{M} - \frac{8(3r_0 + 1)}{9M^2} - \frac{4(M^2 - 4)}{3M2^n} \right) \frac{1}{n}. \tag{9.30}$$

for $M = 2^{r_0}$, $r_0 < n$. Asymptotically $n\langle\tau\rangle$ converges to a constant independent of $\xi = M/2$. Thus, a formula like Eq. (9.30) captures well the saturation behavior of the numerical $\langle\tau\rangle$, although the saturation constant is different. Other examples were investigated in [OG012], such as smallworld networks, where the delocalization transition translates into an entanglement transition, or spin chains. Multipartite entanglement of random pure states localized to a subspace were also independently obtained in [64].

These results allow to directly connect entanglement properties of random vectors to their localization properties. In the absence of correlations between eigenvector

components, our formulas reproduce accurately the entanglement present in several physical systems. In the presence of correlations, while the description of entanglement is still qualitatively correct, some discrepancies appear. It is known that systems with a low amount of entanglement can be simulated classically efficiently. These results thus give an insight on the difficulty to simulate classically physical systems.

Chapter 10

Perspectives

My future research activity should be oriented towards three main topics. While the two last ones (spectral properties of complex networks and multifractality) quite naturally fit in the activity of the Statistical physics team of LPTMS, the first one (tensors and spin systems) opens a new direction, which is more directly related with mathematical results that appeared recently in the literature. I briefly list below a few open directions on these topics.

1. Quantum properties of spin systems

Recent developments in the domain of quantum information had led to a renewed interest in fundamental issues pertaining to properties of quantum states. As various implementations of systems with small number of qubits are now available to experimentalists (supraconducting devices, atoms, ions...), the theory of quantum information is interested in the optimal way in which these quantum states can be manipulated by exploiting their specific properties.

In this domain, characterizing, detecting and measuring quantum entanglement is the source of many open problems. A direction I intend to follow is to investigate questions related with entanglement and classicality of quantum state. In quantum optics, "classical states" are states whose Glauber-Sudarshan P-function is positive: these are states whose density matrix is a convex sum of projectors on coherent states. Generalizing this notion of classical states familiar in quantum optics, we defined classical spin states as classical mixtures of projectors on coherent spin states [OG017].

1.1. Tensors

One goal is to describe 'almost classical states'. The notion of classicality (or of quantumness), beyond its mathematical definition, remains unclear. A starting direction would be to establish precise classicality criteria, by developing tools in order to better understand the structure of the set of quantum states that can be considered almost classical. I will focus in particular on the recently developed spectral theory of tensors. In the simplest case of a symmetric space associated with two qubits, i.e. a spin 1, there exists a necessary and sufficient condition for classicality.

This condition can be expressed as positivity of a certain matrix (see [OG017]). This matrix can be seen as a tensor of order two (with two indices). For larger spins, it turns out that similar expressions can be obtained using higher-order tensors. As it happens, the theory of tensors has flourished in the mathematical literature in very recent years. New directions are unfolding and many applications have appeared, at the interface between mathematics, computer science and theoretical physics, such as random tensors (in the spirit of random matrix theory), models of tensor field theories, spectral theory of non-negative tensors, and so on.

Getting familiar with all this literature should allow to open up a new line of research bridging tensor theory and geometry of spin systems.

1.2. Most quantum states

Another goal is to investigate the other end of the problem, that is, extreme quantum states. These are states which are "maximally quantum", i.e. as far from classical states as possible. These "Queens of Quantum" [OG023] may be expected to be a useful resource in quantum information. But so far these states have been obtained only by numerical optimization, and discovered only in the lowest-dimensional cases. Besides, little is known about their physical properties.

An interesting aspect would be to try and identify (hopefully analytically) extreme quantum states for larger dimensional spin states, in particular for multipartite systems. This would then lead to the investigation of their physical properties, and their possible applications; in particular one should check how these states keep their quantumness under decoherence, external noise, or particle loss. As these states have a near-maximal degree of entanglement, these are ideal testbeds for such approaches.

1.3. New characterizations of entanglement

The study of physical properties of extreme quantum states also requires the development of the study of multipartite entanglement.

SLOCC transformations (stochastic local operations with classical communication) are the generic operations for manipulation of distant qubits. These operations only allow to access a certain ensemble of quantum states from a given initial state. The set of states accessible from a given one forms an entanglement class, and various classes can be identified. Entanglement classification is a question for which only partial answers exist, in the case of few-qubit pure states. Nevertheless, the general question of classifying, detecting and quantifying entanglement for mixed states remains open.

The tensor approach to the problem could allow to make some progress in the classification of SLOCC classes for multipartite entanglement, for instance by constructing polynomial invariants. This classification goes together with the construction of entanglement witnesses, which give an experimental way of detecting entanglement in physical systems. The question can of course be generalized to higher-dimensional qudits.

2. Complex networks

Information retrieval within the World wide web is based on the PageRank algorithm, proposed in 1998, which forms the basis of the Google web browser. The root of this algorithm is to contruct a vector (the pageRank vector) which allows to rank webpages according to their relative importance. The results that we have obtained on the subject showed that there exists a delocalized phase for the PageRank vector when some parameters of the model are changed; besides, a delocalization transition takes place in the complex plane of eigenvalues of the Google matrix when the PageRank is localized.

2.1. Communities and the game of Go

In publications [OG031] and [OG041] we have considered complex networks associated with the game of go. The questions raised there are in fact very general: how can one connect spectral properties of the Google matrix of the graph with properties of the underlying graph? In [OG041] we have proposed that eigenvectors of the Google matrix could serve as community detectors in the graph of go. This opens questions such as what are the role and the properties of relaxation modes, and how do eigenvectors besides PageRank localize or delocalize on the graph.

The question of community detection is a vast and complex one. We have started a collaboration with a US team on the detection of communities in directed networks such as our model for the game of go. These results could then be applied to the game itself. While chess computers defeated professional players more than 15 years ago, computers still struggle in the game of go, although spectacular progress has been made in the past ten years thanks to the introduction of ideas coming from physics, in particular Monte-Carlo approaches. The network approach could help in that direction.

2.2. Complex networks: spectral aspects

I also intend to dedicate some time to a question that lies at the interface between the domain of complex networks and that of quantum multifractality. One of the questions on the Google matrix is how to understand the distribution of its eigenvalues in the complex plane (the matrix being non-Hermitian). The cloud of eigenvalues possesses a characteristic radius whose value could be obtained from properties of the underlying graph. In [OG039] we have obtained expressions for the spectral density of matrices associated with a graph. These expressions were derived in the simplest case of a tree graph with constant connectivity. It would be interesting to try and extend these results to web-like graphs. These questions also occur in closely related problems, such as in smallworld networks, which are regular graphs with long-range links.

Besides, some of these models, when seen as disordered systems, display multifractal properties of their wavefunctions. An interesting aspect would be to make connections with multifractal quantum maps.

3. Wavefunction multifractality

Systems intermediate between integrable and chaotic systems, or critical systems, possess properties which are original and still not entirely understood. A general theory describing these systems is still lacking, despite the experimental consequences of these peculiar properties. We also mentioned that these systems are relevant to quantum information, because of their specific entanglement properties, and also as they are examples where efficient algorithms for quantum information processing can be conceived. Several researche directions are to be considered.

3.1. Multifractal quantum maps

Various families of complex systems have been shown to display Anderson-like transitions. Simple models where intermediate properties were observed include quantizations of certain classical maps, Lax matrices of certain integrable N-body systems, 1D mapping of the Anderson model. However, spectral characteristics, such as nearest-neighbour spacing distributions (and their generalizations) or the spectral form factor, have been obtained analytically only for a few of them. A detailed analytical investigation of these systems should allow us to better characterize their spectral properties: joint probability distribution function of eigenvalues, nearest or next-to-nearest neighbour spacing distribution, level compressibility. Techniques from random matrix theory, such as the Coulomb gas method, have been proven useful for the calculation of asymptotic spectral distributions. These methods could be adapted to the matrix ensembles considered here in order to get such asymptotic formulas. In parallel, properties of multifractal dimensions such as the symmetry of anomalous exponents, or the connection between the singularity spectrum and the distribution of extremal values of eigenvectors, should be investigated.

As mentioned above, numerical results are very diffcult to obtain due to the asymptotic nature of multifractal dimensions, which requires to diagonalize a large amount of very large matrices in order to get reliable results. This is why analytical tools should be developed to investigate the different aspects of critical systems, that is, spectral properties, multifractality of the eigenfunctions, and other properties such as the wave-packet behaviours. From a theoretical point of view, we mentioned an analogy between the quantum intermediate kicked map and certain ensembles of Lax matrices of classical N-body integrable systems. The deep origin of this connection has not yet been elucidated, and this should be understood. The rich mathematical structure of our models should be further exploited in order to get analytic results on multifractal dimensions for such random matrix ensembles.

3.2. Properties of multifractals

The fascinating relation (8.14) linking the information dimension of eigenfunctions with the level compressibility characterizing the spectrum has been accurately verified both analytically (in asymptotic regimes) and numerically for various models. On the other hand, as we mentioned, it seems to break down for some other models. A similar status affects the symmetry relation of the multifractal spectrum, which is

valid for some models but not all of them. The relation between spectral and multifractal properties should be explored in detail, as well as the extent of validity of the generalizations proposed in the literature. In order to investigate such relations between multifractality and spectral properties, quantum chaos provides us with a convenient tool. Semiclassical trace formulae enable to express spectral densities of quantum systems as a sum over periodic orbits of the underlying classical system. Diffractive corrections can be taken into account. In our paradigmatic intermediate quantum map, the underlying classical map is especially simple. Such an approach could be usefully applied in our context. This should yield tractable expressions and interesting analytical results. The extent of these relations to iterates of the quantum maps rather than its eigenvectors is also a natural question, as iterates of wavepackets are the objects that appear in actual experiments.

3.3. Delocalization transition

Very recent papers form 2013 and 2014 investigate delocalization transition on the Cayley tree. For this system, it was observed that two transition points exist, one corresponding to a delocalization transition of eigenvectors, the second one to a transition in statistical properties of the spectrum of eigenvaues. The numerical data do not yet allow to confirm or infirm this preliminary observation, and the status of the transition is yet unclear.

Preliminary works have allowed us to observe a similar kind of double transition on other systems. This direction should be pursued. More refined analysis of these transitions should allow to clarify this question, which raises much debate at the present time.

3.4. Quantum information and multifractality

As mentioned, the field of quantum information has developed very actively in the world in the past few years. One of the applications consists in the development of quantum algorithm performing computational tasks faster than their classical counterparts. In view of the experimental progress in the realization of small quantum processors, it is important to have a clear picture of the applicability of quantum procedures to these devices. I would like to study the conception and implementation of quantum algorithms simulating multifractal systems. Most importantly, one should devise efficient quantum methods to extract information, in particular how it is possible to get relevant information from multifractal wavefunctions once they have been simulated: quantum wavelet transform, sensitivity to experimental noise, etc.

Besides, experimental progress opens the way towards the detection of multifractality in physical systems such as cold atoms subjected to particular potentials. One must be able to estimate what is the robustness of multifractality under perturbations of the system, and to identify which quantities may conserve some indication of multifractality.

3.5. Extreme value statistics

The problem of multifractal fluctuations in disordered systems may also be considered from the point of view of extreme value statistics. One question is to describe the probability that a certain function (typically a time-dependent signal) increases beyond some given threshold. For disordered systems, the properties of the maximum is related with multifractality properties. Various analytical and numerical results have described the probability density function of the number of entries of a function larger than some fixed value for logarithmically correlated systems. For multifractals, the typical value of the maximum of a wavefunction follows a power-law scale which depends on asymptotic properties of the singularity spectrum.

It would be interesting to better understand properties of extreme values for multifractal quantum wavefunctions: distribution of the maximum, tails of the distribution, connection between our systems and logarithmically correlated processes. One should try and understand to which universality classes these quantum maps belong in terms of extreme value statistics, given the underlying classical dynamics.

****

Bibliography

[1] http://www.nobelprize.org/nobel_prizes/physics/laureates/

[2] P. W. Anderson, Phys. Rev. **109**, 1492 (1958).

[3] E. Abrahams, P.W. Anderson, D.C. Licciardello and T.V. Ramakrishnan, Phys. Rev. Lett. **42**, 673 (1979).

[4] F. Wegner, Z. Phys. B **36**, 209 (1980)

[5] C. Castellani and L. Peliti, J. Phys. A: Math. Gen. **19**, L429 (1986).

[6] H. Aoki, J. Phys. C **16**, L205 (1983).

[7] M. Schreiber and H. Grussbach, Phys. Rev. Lett. **67**, 607 (1991).

[8] M. Janssen, Int. J. Mod. Phys. **8**, 943 (1994).

[9] J. T. Chalker and G. J. Daniell, Phys. Rev. Lett. **61**, 593 (1988).

[10] B. Huckestein, Rev. Mod. Phys. **67**, 357 (1995).

[11] E. Bogomolny and C. Schmit, Phys. Rev. Lett. **92**, 244102 (2004).

[12] A. D. Mirlin, Y. V. Fyodorov, F.-M. Dittes, J. Quezada, and T. H. Seligman, Phys. Rev. E **54**, 3221 (1996).

[13] J. A. Méndez-Bermúdez, A. Alcázar-López, and I. Varga, Europhys. Lett. **98**, 37006 (2012).

[14] Y. V. Fyodorov, A. Ossipov, and A. Rodriguez, J. Stat. Mech. L12001 (2009).

[15] N. Meenakshisundaram and A. Lakshminarayan, Phys. Rev. E **71**, 065303(R) (2005).

[16] P. Repetowicz, U. Grimm, and M. Schreiber, Phys. Rev. B **58**, 13482 (1998).

[17] C.-P. Zhu and S.-J. Xiong, Phys. Rev. B **63**, 193405 (2001).

[18] J. N. Bandyopadhyay, J. Wang and J. Gong, Phys. Rev. E **81**, 066212 (2010).

[19] A. M. García-García and J. Wang, Phys. Rev. Lett. **94**, 244102 (2005).

[20] M. V. Feigel'man, L. B. Ioffe, V. E. Kravtsov, and E. A. Yuzbashyan, Phys. Rev. Lett. **98**, 027001 (2007).

[21] F. Evers, A. D. Mirlin, Rev. Mod. Phys. **80**, 1355 (2008).

[22] F. Evers, A. Mildenberger, and A. D. Mirlin, Phys. Rev. Lett. **101**, 116803 (2008).

[23] E. B. Bogomolny, R. Dubertrand and C. Schmit, Nonlinearity **22**, 2101 (2009).

[24] M. S. Foster, S. Ryu, and A. W. W. Ludwig, Phys. Rev. B **80**, 075101 (2009).

[25] A. Rodriguez, L. J. Vasquez, and R. A. Römer, Phys. Rev. Lett. **102**, 106406 (2009).

[26] A. Rodriguez, L. J. Vasquez, K. Slevin and R. A. Römer, Phys. Rev. Lett. **105**, 046403 (2010).

[27] I. S. Burmistrov, S. Bera, F. Evers, I. V. Gornyi and A. D. Mirlin, Ann. Phys. **326**, 1457 (2011).

[28] C. Monthus and T. Garel, J. Stat. Mech. P09015 (2010).

[29] I. Gruzberg, A. Ludwig, A. D. Mirlin, and M. R. Zirnbauer, Phys. Rev. Lett. **107**, 086403 (2011).

[30] I. A. Gruzberg, A. D. Mirlin, M. R. Zirnbauer, Phys. Rev. B **87**, 125144 (2013).

[31] J. Billy, V. Josse, Z. Zuo, A. Bernard, B. Hambrecht, P. Lugan, D. Clément, L. Sanchez-Palencia, P. Bouyer and A. Aspect, Nature **453**, 891 (2008).

[32] G. Roati, C. D'Errico, L. Fallani, M. Fattori, C. Fort, M. Zaccanti, G. Modugno, and M. Inguscio, Nature **453**, 895 (2008).

[33] M. Robert-de-Saint-Vincent, J.-P. Brantut, B. Allard, T. Plisson, L. Pezzé, L. Sanchez-Palencia, A. Aspect, T. Bourdel and P. Bouyer, Phys. Rev. Lett. **104**, 220602 (2010).

[34] J. Chabé, G. Lemarié B. Grémaud, D. Delande, P. Szriftgiser, and J. Garreau, Phys. Rev. Lett. **101**, 255702 (2008).

[35] G. Lemarié, J. Chabé, P. Szriftgiser, J. Garreau, B. Grémaud, and D. Delande, Phys. Rev. A **80**, 043626 (2009).

[36] G.Lemarié, H. Lignier, D. Delande, P. Szriftgiser and J. Garreau, Phys. Rev. Lett. **105**, 090601 (2010).

[37] F. Jendrzejewski, A. Bernard, K. Müller, P. Cheinet, V. Josse, M. Piraud, L. Pezzé, L. Sanchez-Palencia, A. Aspect, and P. Bouyer, Nature Physics **8**, 398 (2012).

[38] W. R. McGehee, S. S. Kondov, W. Xu, J. J. Zirbel, and B. DeMarco, Phys. Rev. Lett. **111**, 145303 (2013).

[39] S. Faez, A. Strybulevych, J. Page, A. Lagendijk, and B. A. van Tiggelen, Phys. Rev. Lett. **103**, 155703 (2009).

[40] M. Segev, Y. Silberberg, and D. N. Christodoulides, Nature Photonics **7**, 197 (2013).

[41] B. Mandelbrot, *Les objets fractals : forme, hasard et dimension*, Paris, Flammarion (1975).

[42] K. Falconer, *Fractal Geometry – Mathematical Foundations and Applications*, Second Edition, John Wiley & Sons Eds. (2003).

[43] D. M. Basko, I. L. Aleiner, and B. L. Altshuler, Annals of Physics **321**, 1126 (2006).

[44] I. L. Aleiner, B. L. Altshuler, and G. V. Shlyapnikov, Nature Physics **6**, 900 (2010).

[45] O. Bohigas, M.-J. Giannoni, and C. Schmit, Phys. Rev. Lett. **52**, 1 (1984).

[46] M. V. Berry and M. Tabor, Proc. Roy. Soc. Lond. **356**, 375 (1977).

[47] B. I. Shklovskii, B. Shapiro, B. R. Sears, P. Lambrianides, and H. B. Shore, Phys. Rev. B **47**, 11487 (1993).

[48] E. Bogomolny, U. Gerland, and C. Schmit, Phys. Rev. E **59**, R1315 (1999).

[49] E. P. Wigner, Ann. Math. **53**, 36 (1951).

[50] F. J. Dyson, J. Math. Phys. **3**, 140 (1962).

[51] C. E. Porter, *Statistical Theories of Spectra: Fluctuations* (Academic Press, New York, 1965).

[52] B. Shapiro, Int. J. Mod. Phys. B **10**, 3539 (1996).

[53] J. H. Hannay and M. V. Berry, Physica **1D**, 267 (1980).

[54] D. P. DiVincenzo, Fortschritte der Physik **48**, 771 (2000).

[55] P. Shor, SIAM Journal on Computing **26**, no 5, 1484 (1997).

[56] B. Georgeot and D. L. Shepelyansky, Phys. Rev. E **62**, 3504 (2000); **62**, 6366 (2000).

[57] C. Nadal, S. N. Majumdar, and M. Vergassola, Phys. Rev. Lett. **104**, 110501 (2010); *ibid*, J. Stat. Phys. **142**, 403 (2011).

[58] P. Facchi, U. Marzolino, G. Parisi, S. Pascazio and A. Scardicchio, Phys. Rev. Lett. **101**, 050502 (2008).

[59] A. De Pasquale, P.Facchi, G. Parisi, S. Pascazio, and A. Scardicchio, Phys. Rev. A **81**, 052324 (2010).

[60] L. Amico, R. Fazio, A. Osterloh and V. Vedral, Rev. Mod. Phys. **80**, 517 (2008).

[61] A. Lakshminarayan and V. Subrahmanyam, Phys. Rev. A **67**, 052304 (2003).

[62] L. F. Santos, G. Rigolin, and C. O. Escobar, Phys. Rev. A **69**, 042304 (2004).

[63] C. Mejía-Monasterio, G. Benenti, G. G. Carlo, and G. Casati, Phys. Rev. A **71**, 062324 (2005).

[64] W. G. Brown, L. F. Santos, D. J. Starling, and L. Viola, Phys. Rev. E **77**, 021106 (2008).

[65] O. Bohigas and M. J. Giannoni, in *Mathematical and Computational Methods in Nuclear Physics*, edited by J. S. Dehesa, J. M. G. Gomez, and A. Polls (Springer Verlag, Spain, 1984), proceedings of the 6th Granada Workshop (Lecture Notes in Physics Vol. 209 p.1).

[66] V. Oganesyan and D. A. Huse, Phys. Rev. B **75**, 155111 (2007).

[67] C. Kollath, G. Roux, G. Biroli, and A. M. Läuchli, J. Stat. Mech. **P08011** (2010).

[68] M. Rigol and L. F. Santos, Phys. Rev. A **82**, 011604(R) (2010); L. F. Santos and M. Rigol, Phys. Rev. E **82**, 031130 (2010); Phys. Rev. E **81**, 036206 (2010).

[69] M. Collura, H. Aufderheide, G. Roux, and D. Karevski, Phys. Rev. A **86**, 013615 (2012).

[70] V. Oganesyan, A. Pal, and D. A. Huse, Phys. Rev. B **80**, 115104 (2009); A. Pal and D. A. Huse, Phys. Rev. B **82**, 174411 (2010); E. Cuevas, M. Feigel'man, L. Ioffe, and M. Mézard, Nature Comm. **3**, 1128 (2012); G. Biroli, A. C. Ribeiro-Teixeira, and M. Tarzia, *Preprint* [arXiv:1211.7334] (2012); S. Iyer, V. Oganesyan, G. Refael, and D. A. Huse, Phys. Rev. B **87**, 134202 (2013).

[71] A. De Luca and A. Scardicchio, Europhys. Lett. **101** 3, 37003 (2013).

[72] M. L. Mehta, *Random Matrix Theory* (Springer, New York, 1990).

[73] E. Bogomolny, U. Gerland, and C. Schmit, Eur. Phys. J. B **19**, 121 (2001).

[74] T. Gorin and J. Wiersig, Phys. Rev. E **68**, 065205(R) (2003).

[75] J. Marklof, in *Proceedings of the 3rd European Congress of Mathematics* (Birkhuser, Basel, 2001), (Barcelona, 2000) - Progress in Mathematics Vol. 202, pp.421-427.

[76] A. Pandey, O. Bohigas, and M.-J. Giannoni, J. Phys. A: Math. Gen. **22**, 4083 (1989).

[77] P. M. Bleher, J. Statist. Phys. **61**, 869 (1990).

[78] P. M. Bleher, J. Statist. Phys. **63**, 261 (1991).

[79] C. D. Greenman, J. Phys. A **29**, 4065 (1996).

[80] J. J. Duistermaat and V. W. Guillemin, Invent. Math. **29**, 39 (1975).

[81] A. Weinstein, Duke Math. J. **44**, 883 (1977).

[82] Y. Colin de Verdière, Comment. Math. Helvetici **54**, 508 (1979).

[83] H. Wu, M. Vallières, D. H. Feng, and D. W. L. Sprung, Phys. Rev. A **42**, 1027 (1990).

[84] A. Altland and M. R. Zirnbauer, Phys. Rev. B **55**, 1142 (1997).

[85] D. Wintgen, Phys. Rev. Lett. **58**, 1589 (1987).

[86] R. U. Haq, A. Pandey, and O. Bohigas, Phys. Rev. Lett. **48**, 1086 (1982).

[87] L. Velilla, B. Lepetit, A. Aguado, J. A. Beswick, and M. Paniagua, J. Chem. Phys. **129**, 084307 (2008).

[88] M. V. Berry and M. Robnik, J. Phys. A: Math. Gen. **19**, 649 (1986).

[89] E. Bogomolny, F. Leyvraz, and C. Schmit, Comm. Math. Phys. **176**, 577 (1996).

[90] F. J. Dyson and M. L. Mehta, J. Math. Phys. **4** nr 5, 701 (1963).

[91] E. P. Wigner, SIAM Review **9**, 1 (1967).

[92] B. Dietz and F. Haake, Z. Phys. B – Condensed Matter **80**, 153 (1990).

[93] A. Y. Abul-Magd and M. H. Simbel, Phys. Rev. E **60**, 5371 (1999).

[94] C. A. Tracy and H. Widom, *Introduction to random matrices*, in Geometric and quantum aspects of integrable systems (1993) 103.

[95] F. Bornemann, Math. Comput. **79**, 871 (2010).

[96] J. T. Chalker, V. E. Kravtsov, and I. V. Lerner, JETP Lett. **64**, 386 (1996).

[97] H. Hernández-Saldaña, J. Flores, and T. H. Seligman, Phys. Rev. E **60**, 449 (1999).

[98] T. H. Seligman, J. J. M. Verbaarschot, and M. R. Zirnbauer, Phys. Rev. Lett. **53**, 215 (1984).

[99] M. V. Berry and M. Robnik, J. Phys. A: Math. Gen. **17**, 2413 (1984).

[100] E. Bogomolny, Sov. Phys. JETP Lett. **41**, 65 (1986).

[101] M. Moshe, H. Neuberger, and B. Shapiro, Phys. Rev. Lett. **73**, 1497 (1994).

[102] U. Gerland, Phys. Rev. Lett. **83**, 1139 (1999).

[103] T. Jonckheere, B. Grémaud, and D. Delande, Phys. Rev. Lett. **81**, 2442 (1998).

[104] B. L. Altshuler and L. S. Levitov, Phys. Rep. **288**, 487 (1997).

[105] T. A. Brody, Lett. Nuov. Cim. **7**, 482 (1973).

[106] N. Rosenzweig and C. E. Porter, Phys. Rev. **120**, 1698 (1960).

[107] A. M. García-García and J. J. M. Verbaarschot, Phys. Rev. E **67**, 046104 (2003).

[108] K. A. Muttalib, Y. Chen, M. E. H. Ismail, and V. N. Nicopoulos, Phys. Rev. Lett. **71**, 471 (1993).

[109] C. M. Canali, Phys. Rev. B **53**, 3713 (1996).

[110] E. Bogomolny, O. Bohigas, and M. P. Pato, Physical Review E **55**, 6707 (1997).

[111] S. Nishigaki, Phys. Rev. E **59**, 2853 (1999).

[112] J. Choi and K. A. Muttalib, J. Phys. A: Math. Theor. **42**, 152001 (2009).

[113] P. Cizeau and J. P. Bouchaud, Physical Review E 50, 1810 (1994).

[114] V. E. Kravtsov and K. A. Muttalib, Phys. Rev. Lett. **79**, 1913 (1997).

[115] M. L. Ndawana and V. E. Kravtsov, J. Phys. A: Math. Gen. **36**, 3639 (2003).

[116] O. M. Yevtushenko and V. E. Kravtsov, Phys. Rev. E **69**, 026104 (2004).

[117] M. V. Berry and P. J. Richens, Physica D **2**, 495 (1981).

[118] A. B. Zemlyakov and A. N. Katok, Math. Notes **18**, 760 (1976).

[119] J. P. Keating, Nonlinearity **4**, 309 (1991).

[120] N.L. Balasz and A. Voros, Ann. Phys. (N.Y.) **190**, 1 (1989).

[121] M. Saraceno, Ann. Phys.(N.Y.) **199**, 37 (1990).

[122] R. Schack, Phys. Rev. A **57**, 1634 (1998).

[123] A. J. Scott and C. M. Caves, J. Phys. A: Math. Gen. **36**, 9553 (2003).

[124] G. Casati, B. V. Chirikov, J. Ford, and F. M. Izrailev, Lect. Notes Phys. (Springer) **93**, 334 (1979).

[125] M. V. Berry, N. L. Balasz, M. A. Tabor and A. Voro, Ann. Phys. **122**, 26 (1979).

[126] F. M. Izrailev, Phys. Rev. Lett. **56**, 541 (1986).

[127] A. Bouzouina and S. De Bièvre, Comm. Math. Phys. **178**, 83 (1996).

[128] B. Bulka, M. Schreiber, and B. Kramer, Z. Phys. B **66**, 21 (1987).

[129] G. Semeghini, M. Landini, P. Castilho, S. Roy, G. Spagnolli, A. Trenkwalder, M. Fattori, M. Inguscio, and G. Modugno, Nature Physics **11**, 554 (2015).

[130] D. Delande and G. Orso, arXiv:1403.3821

[131] V. E. Kravtsov, I. V. Lerner, B. L. Altshuler, and A. G. Aronov, Phys. Rev. Lett. **72**, 888 (1994).

[132] D. Braun, G. Montambaux, and M. Pascaud, Phys. Rev. Lett. **81**, 1062 (1998).

[133] L. S. Levitov, Europhys. Lett. **9**, 83 (1989).

[134] L. S. Levitov, Phys. Rev. Lett. **64**, 547 (1990).

[135] T. H. Seligman, J. J. M. Verbaarschot, and M. R. Zirnbauer, J. Phys. A: Math. Gen. **18**, 2751 (1985).

[136] F. Evers and A. D. Mirlin, Phys. Rev. Lett. **84**, 3690 (2000).

[137] A. D. Mirlin and F. Evers, Phys. Rev. B **62** 7920 (2000).

[138] S. Fishman, D. R. Grempel, and R. E. Prange, Phys. Rev. Lett. **49**, 509 (1982).

[139] D. R. Grempel, R. E. Prange, and S. Fishman, Phys. Rev. A **29**, 1639 (1984).

[140] B. V. Chirikov, Phys. Rep. **52**, 263 (1979).

[141] A.J. Lichtenberg and M.A. Lieberman, *Regular and Stochastic Motion* (Springer, New York, 1983).

[142] D. L. Shepelyansky, Phys. Rev. Lett. **56**, 677 (1986).

[143] B. Levi and B. Georgeot, Phys. Rev. E **70**, 056218 (2004).

[144] K.M.Frahm and D.L.Shepelyansky, Phys. Rev. E **80**, 016210 (2009).

[145] J. Wang and A. M. García-García, Phys. Rev. E **79**, 036206 (2009).

[146] T. Prosen and M. Žnidarič, Phys. Rev. Lett. **87**, 114101 (2001).

[147] G.Casati, I.Guarneri, D.L.Shepelyansky, Phys. Rev. Lett. 62, **345** (1989).

[148] G. Lemarié, B. Grémaud, and D. Delande, Europhys. Lett. **87**, 37007 (2009).

[149] J. Marklof and Z. Rudnick, GAFA, Geom. Funct. Anal. **10**, 1554 (2000).

[150] F. Haake, *Quantum Signatures of Chaos* (Berlin: Springer) (2001).

[151] G. Casati and T. Prosen, Phys. Rev. Lett. **85**, 4261 (2000).

[152] E. Bogomolny and C. Schmit, Phys. Rev. Lett. **93**, 254102 (2004).

[153] A. M. García-García and J. Wang, Phys. Rev. E **73**, 036210 (2006).

[154] V. I. Arnol'd, *Mathematical Methods of Classical Dynamics* (Springer, Berlin) (1978).

[155] P. Lax, *Integrals of nonlinear equations of evolution and solitary waves*, Comm. Pure Applied Math. **21**, 467 (1968).

[156] O. Babelon and C.-M. Viallet, *Hamiltonian structures and Lax equations*, Phys. Lett. B **237**, 411 (1990).

[157] O. Babelon, D. Bernard, and M. Talon, *Introduction to Classical Integrable Systems* Cambridge Monographs on Mathematical Physics (Cambridge University Press) (2003).

[158] M.A. Olshanetsky and A.M. Perelomov, Phys. Rep. **71**, 313 (1981).

[159] F. Calogero, Lett. Nuovo Cimento **20**, 251 (1977).

[160] S. Ruijsenaars, Publ. RIMS, Kyoto Univ. **31**, 247 (1995).

[161] F. Hausdorff, Math. Zeitschr. **9**, 74-109 and 280-299 (1921).

[162] M. E. Cates and J. M. Deutsch, Phys. Rev. A **35**, 4907 (1987).

[163] B. Duplantier and A. W. W. Ludwig, Phys. Rev. Lett. **66**, 247 (1991).

[164] J. T. Chalker, Physica A **167**, 253 (1990).

[165] Y. V. Fyodorov and A. D. Mirlin, Phys. Rev. B **55**, R16001 (1997).

[166] T. Brandes, B. Huckestein, and L. Schweitzer, Ann. Phys. **508**, 633 (1996).

[167] E. Cuevas and V. E. Kravtsov, Phys. Rev. B **76**, 235119 (2007).

[168] V. E. Kravtsov, A. Ossipov, O. M. Yevtushenko, and E. Cuevas, Phys. Rev. B **82**, 161102(R) (2010).

[169] V. E. Kravtsov, A. Ossipov and O. M. Yevtushenko, J. Phys. A: Math.Theor. **44**, 305003 (2011).

[170] A. R. Subramaniam, I. A. Gruzberg, A. W. W. Ludwig, F. Evers, A. Mildenberger, and A. D. Mirlin, Phys. Rev. Lett. **96**, 126802 (2006).

[171] A. Mildenberger, A. R. Subramaniam, R. Narayanan, F. Evers, I. A. Gruzberg, and A. D. Mirlin, Phys. Rev. B **75**, 094204 (2007).

[172] U. Frisch and G. Parisi, in *Turbulence and predictability in geophysical fluid dynamics and climate dynamics* (M. Ghil, R. Benzi and G. Parisi Eds.) North-Holland, Amsterdam (1985) 84-88

[173] T. C. Halsey, M. H. Jensen, L. P. Kadanoff, I. Procaccia, and B. I. Shraiman, Phys. Rev. A **33** (1986) 1141

[174] C. Monthus and T. Garel, J. Stat. Mech. 2010, P06014 (2010).

[175] Y. V. Fyodorov, J. Stat. Mech. P07022 (2009).

[176] Y. V. Fyodorov and A. D. Mirlin, Phys. Rev. B **51**, 13403 (1995).

[177] V. I. Falko and K. B. Efetov, Phys. Rev. B 52, 17413 (1995).

[178] V. N. Prigodin and B. L. Altshuler, Phys. Rev. Lett. **80**, 1944 (1998).

[179] I. Varga, Phys. Rev. B **66**, 094201 (2002).

[180] E. Cuevas, M. Ortuño, V. Gasparian, and A. Pérez-Garrido, Phys. Rev. Lett. **88**, 016401 (2001).

[181] A. M. Yaglom, Soviet Physics-Doklady Vol. II, 2629 (1966).

[182] B. B. Mandelbrot, J. Fluid Mech. **62**, 331 (1974).

[183] J.-P. Kahane, *Sur le modèle de turbulence de Benoît Mandelbrot*, C.R. Acad. Sci. Paris **278**, 567 (1974).

[184] J.-P. Kahane and J. Peyrière, *Sur certaines martingales de Benoît Mandelbrot*, Adv. Math. **22**, 131 (1976).

[185] J.-P. Kahane, *Sur le chaos multiplicatif*, Ann. Sci. Math. Québec **9** no.2, 105 (1985).

[186] T. C. Halsey, M. H. Jensen, L. P. Kadanoff, I. Procaccia, and B. I. Shraiman, Phys. Rev. A **33**, 1141 (1986).

[187] A. Arneodo, G. Grasseau and M. Holschneider, Phys. Rev. Lett. **61**, 2281 (1988).

[188] W. G. Hanan, J. Gough, and D. M. Heffernan, Phys. Rev. E **63**, 011109 (2000).

[189] B. Derrida, Phys. Rev. B **25** nr 5, 213 (1981).

[190] L. J. Vasquez, A. Rodriguez, and R. A. Römer, Phys. Rev. B **78**, 195106 (2008); A. Rodriguez, L. J. Vasquez, and R. A. Römer, Phys. Rev. B **78**, 195107 (2008).

[191] E. Cuevas, Phys. Rev. B **68**, 184206 (2004).

[192] A. Chhabra and R. V. Jensen, Phys. Rev. Lett. **62**, 1327 (1989).

[193] F. Milde, R. A. Römer, and M. Schreiber, Phys. Rev. B **55**, 9463 (1997).

[194] *Wavelets: Theory and Applications*, G. Erlebacher, M. Y. Hussaini and L. M. Jameson, Eds (Oxford University Press, New York, 1996).

[195] I. Daubechies, Comm. Pure Appl. Math. **41**, 909 (1988).

[196] J. W. Kantelhardt, H. E. Roman and M. Greiner, Physica A **220**, 219 (1995).

[197] W. Uhm and S. Kim, J. Kor. Phys. Soc. **32**, 1 (1997).

[198] H. Hu, A. Strybulevych, J. H. Page, S. E. Skipetrov and B. A. van Tiggelen, Nature physics **4**, 945 (2008).

[199] A. Richardella, P. Roushan, S. Mack, B. Zhou, D. A. Huse, D. D. Awschalom, and A. Yazdani, Science **327**, 665 (2010).

[200] C. D. Errico, E. Lucioni, L. Tanzi, L. Gori, G. Roux, I. P. McCulloch, T. Giamarchi, M. Inguscio, and G. Modugno, arXiv:1405.1210

[201] Y. V. Fyodorov and A. D. Mirlin, Phys. Rev. Lett. **67**, 2405 (1991).

[202] O. Yevtushenko and V. E. Kravtsov, J. Phys. A: Math. Gen. **36**, 8265 (2003).

[203] V. E. Kravtsov, O. M. Yevtushenko, and E. Cuevas, J. Phys. A: Math. Gen. **39**, 2021 (2006).

[204] A. Ossipov, J. Phys. A: Math. Theor. **45**, 335002 (2012).

[205] O. Yevtushenko and A. Ossipov, J. Phys. A: Math. Theor. **40**, 4691 (2007).

[206] M. S. Hussein and M. P. Pato, Physica A **285**, 383 (2000).

[207] C. M. Soukoulis and E. N. Economou, Phys. Rev. Lett. **52**, 565 (1984).

[208] J. L. Pichard and G. Sarma, J. Phys. C **18**, 3457 (1985).

[209] F. Wegner, Nuclear Physics B **316**, 663 (1989).

[210] E. Cuevas, Phys. Stat. Sol. B **241**, 2109 (2004).

[211] A. D. Mirlin, Y. V. Fyodorov, A. Mildenberger, and F. Evers, Phys. Rev. Lett. **97**, 046803 (2006).

[212] A. D. Mirlin and Y. V. Fyodorov, Phys. Rev. Lett. **72**, 526 (1994).

[213] C. Monthus, B. Berche, and C. Chatelain, J. Stat. Mech. **2009**, P12002 (2009).

[214] J. T. Chalker, I. V. Lerner, and R. A. Smith, Phys. Rev. Lett. **77**, 554 (1996).

[215] B. Huckestein and L. Schweitzer, Phys. Rev. Lett. **72**, 713 (1994).

[216] J. T. Chalker and P. D. Coddington, J. Phys. C: Solid State Phys. **21**, 2665 (1988).

[217] R. Klesse and M. Metzler, Phys. Rev. Lett. **79**, 721 (1997).

[218] A. Ossipov, I. Rushkin, and E. Cuevas, Phys. Rev. E **85**, 021127 (2012).

[219] M. L. Ndawana, R. A. Römer, and M. Schreiber, Eur. Phys. J. B **27**, 399 (2002).

[220] J. A. Méndez-Bermúdez, A. Alcázar-López, and I. Varga, arXiv:1303.5665 [cond-Mat] (2013).

[221] B. Huckestein and R. Klesse, Phys. Rev. B **59**, 9714 (1999).

[222] R. Ketzmerick, K. Kruse, D. Kraut and T. Geisel, Phys. Rev. Lett. **79**, 1959 (1997).

[223] S. Lloyd, Science **273**, 1073 (1996).

[224] B. Georgeot and D. Shepelyansky, Phys. Rev. Lett. **86**, 5393 (2001).

[225] B. Georgeot and D. Shepelyansky, Phys. Rev. Lett. **86**, 2890 (2001); B. Lévi, B. Georgeot and D. Shepelyansky, Phys. Rev. E **67**, 046220 (2003).

[226] E. Lubkin, J. Math. Phys. (N.Y.) **19**, 1028 (1978).

[227] S. Lloyd and H. Pagels, Ann. Phys., NY **188**, 186 (1988).

[228] D. N. Page, Phys. Rev. Lett. **71**, 1291 (1993).

[229] C. H. Bennett, D. P. DiVincenzo, J. A. Smolin, and W. K. Wootters, Phys. Rev. A **54**, 3824 (1996).

[230] V. Vedral, M. B. Plenio, M. A. Rippin, and P. L. Knight, Phys. Rev. Lett. **78**, 2275 (1997).

[231] V. Vedral, M. B. Plenio, K. Jacobs, and P. L. Knight, Phys. Rev. A **56**, 4452 (1997).

[232] V. Vedral and M. B. Plenio, Phys. Rev. A **57** 1619 (1998).

[233] A. Wong and N. Christensen, Phys. Rev. A **63** 044301 (2001).

[234] S. Hill and W. K. Wootters, Phys. Rev. Lett. **78**, 5022 (1997).

[235] M. B. Plenio and S. Virmani, Quant. Inf. Comput. **7**, 1 (2007).

[236] C. H. Bennett, H. Bernstein, S. Popescu, and B. Schumacher, Phys. Rev. A **53**, 2046 (1996).

[237] M. A. Nielsen and I. L. Chuang, *Quantum computation and quantum information*, Cambridge university press (2000).

[238] S. Popescu and D. Rohrlich, Phys. Rev. A **56**, R3319 (1997).

[239] M. J. Donald, M. Horodecki and O. Rudolph , J. Math. Phys. **43**, 4252 (2002).

[240] A. D. Meyer and N. R. Wallach, J. Math. Phys. **43**, 4273 (2002).

[241] P. Rungta and C. M. Caves, Phys. Rev. A **67**, 012307 (2003).

[242] K. Zyczkowski and H. -J. Sommers , J. Phys. A: Math. Gen. **34**, 7111-7125 (2001).

[243] A. Hurwitz, Nachr. Ges. Wiss. Goettinger Math. Phys. Kl. **71**, (1897).

[244] S. K. Foong and S. Kanno, Phys. Rev. Lett. **72**, 114 (1994).

[245] P. Facchi, G. Florio, G. Parisi and S. Pascazio, Phys. Rev. A **77**, 060304 (R) (2008).

[246] S. Sen, Phys. Rev. Lett. **77**, 1 (1996).

[247] M. Znidaric, J. Phys. A: Math. Theor. **40**, F105 (2007).

[248] V. Cappellini, H. -J. Sommers and K. Zyczkowski, Phys. Rev. A **74**, 062322 (2006).

[249] H. -J. Sommers and K. Zyczkowski, J. Phys. A: Math. Gen. **37**, 8457-8466 (2004).

[250] P. Facchi, G. Florio and S. Pascazio, Phys. Rev. A **74**, 042331 (2006).

[251] S. Blinnikov and R. Moessner, Astron. Astrophys. Suppl. Ser. **130**, 193 (1998).

[252] A. Lakshminarayan, Phys. Rev. E **64**, 036207 (2001).

[253] A. J. Scott, Phys. Rev. A **69**, 052330 (2004).

[254] R. Demkowicz-Dobrzanski and M. Kus, Phys. Rev. E **70**, 066216 (2004).

[255] R. F. Abreu and R. O. Vallejos, Phys. Rev. A **75**, 062335 (2007).

[256] J. N. Bandyopadhyay and A. Lakshminarayan, Phys. Rev. Lett. **89**, 060402 (2002).

[257] Y. S. Weinstein and C. S. Hellberg, Phys. Rev. Lett. **95**, 030501 (2005); Y. S. Weinstein and C. S. Hellberg, Phys. Rev. A **71**, 014303 (2005); Y. S. Weinstein and C. S. Hellberg, Phys. Rev. A **69**, 062301 (2004); Y. S. Weinstein and C. S. Hellberg, Phys. Rev. A **72**, 022331 (2005).

[258] P. Zanardi, C. Zalka, and L. Faoro, Phys. Rev. A **62**, 030301 (2000).

[259] L. Gong and P. Tong, Phys. Rev. E **74**, 056103 (2006).

[260] I. Varga and J. A. Méndez-Bermúdez, Phys. Stat. Sol. (c) **5**, 867 (2008).

[261] X. Jia, A. R. Subramaniam, I. A. Gruzberg, and S. Chakravarty, Phys. Rev. B **77**, 014208 (2008).

[262] L. Viola and W. G. Brown, J. Phys. A **40**, 8109 (2007).

[263] A. A. Pomeransky and D. L. Shepelyansky, Phys. Rev. A **69**, 014302 (2004).